



Generic Micropatterned Pull-Down Assays for
Quantifying Interaction Dynamics and Stoichiometry
of Protein-Protein Interactions

Dissertation

Presented to the Department of Biology/Chemistry, Osnabrück University,
in partial fulfillment of the requirements for the degree of

‘Doctor rerum naturalium’

Tim Wedeking

Osnabrück

September 2023

Summary

Many cellular functions are governed by an extensive network of protein-protein interactions (PPI) that exhibit regulatory mechanisms through core features such as affinity, avidity and competition. While fulfillment of essential functions such as cell growth, programmed cell death and immune response require a precisely tuned level of activity, dysregulation of such a tightly controlled network leads to serious consequences such as cancerous cell growth, pathogen susceptibility, or autoimmune diseases. Fundamental biological research at the protein level is therefore of vital interest, enabling breakthroughs in medicine while promoting the development of ever more advanced methods to help characterize the many unresolved PPIs.

One of the key factors of cellular signaling is the family of cytokines that regulate hematopoiesis and immunological homeostasis. Serving as the model system of this work, the type I interferon (IFN) signaling pathway plays a prominent role in the response against viral and intracellular bacterial infections. Type I IFN signaling employs a heterodimeric class II cytokine receptor (IFNAR1, IFNAR2), as well as cytosolic associated Janus family tyrosine kinases (JAK) and signal transducers and activators of transcription (STAT) as effector proteins. In general, the JAK-STAT pathway is the hallmark of the class I and II cytokine receptor families. Unique to type I IFN, however, are the negative feedback regulators USP18 and ISG15, which serve to regulate the long-term cellular response by desensitizing IFN signaling. While many insights have been gained in recent years at the receptor and JAK level, better mechanistic understanding of the interplay of cytosolic effector proteins and negative feedback regulators is required. This critically depends on quantifying dynamics and stoichiometry of their molecular interactions. On the one hand, bioanalytical characterization was traditionally tackled by biochemical methods and pull-down assays, but such *in vitro* techniques investigate PPIs far from their biological context and quantitative approaches are very demanding in terms of protein production and purification. *In vivo* techniques, on the other hand, are still challenging as it is not possible to change or control the protein concentrations in living cells. Moreover, many of these methods require target-specific optimization and leave much to be desired in terms of their reliability and simplicity of their overall strategy.

Overcoming these fundamental challenges, this thesis aimed to develop micropatterned nanobody-based pull-down assays to quantify the interaction dynamics and

stoichiometry of cytosolic PPIs. These methods were used to characterize the PPIs of the type I IFN signaling pathway, but we also aspired to develop generically applicable strategies that can be used for a broad range of target proteins. Spatially-resolved nanobody immobilization was achieved by employing a robust poly-L-lysine grafted poly(ethylene glycol) (PLL-PEG) surface architecture, which can be readily generated via microcontact printing and provide surface passivation, biocompatibility and a functional micropatterning in a single step. The pull-down assays employ an anti-GFP nanobody directed against the widely used green fluorescent protein (GFP), providing a generalized targeting strategy instead of targeting a specific protein of interest. To this end, we have developed two methods: The first is nanobody live cell micropatterning, which enables spatiotemporal reorganization of cytosolic GFP-fused proteins inside cells to quantitatively investigate their interaction partners and dynamics. The second is *in situ* single cell pull-down (SiCPull), which directly captures GFP-fused proteins and interacting proteins from whole-cell lysates on the micropatterned chip, enabling background-free quantitative interaction dynamics analysis, and even stoichiometric analysis of individual protein complexes on the single molecule level (SM-SiCPull).

Using the nanobody live cell micropatterning, we could demonstrate that ISG15 acts as a double-edged sword. On the one side, ISG15 canonically rescues USP18 from proteolytic degradation, but on the other side interferes with USP18 binding to STAT2, thus partially obstructing USP18's recruitment to IFNAR2 via STAT2. Furthermore, investigation on the protein domains revealed steric hindrance, as truncation of the N-terminal ISG15 domain abolished the competition. Moreover, SiCPull demonstrated a robust analysis of interaction dynamics of unstimulated STATs, ranging from stable interactions with a lifetime of half an hour, to transient interactions of only mere seconds. Using SM-SiCPull, we could analyze the stoichiometry of individual protein complexes, revealing that both unstimulated and IFN-induced phosphorylated STAT1 featured complex stoichiometries ranging from monomers and dimers to even tetramers.

The here presented methods have the potential for broad application in protein interaction analysis, as they are very robust and well compatible with modern cell biology, requiring only relatively simple equipment for microcontact printing, while employing nanobodies for a generalized pull-down strategy.

Table of contents

1	Introduction	1
1.1	The Protein Puzzle	1
1.2	Cytokine signaling pathways	3
1.3	Type I interferon signaling pathway.....	5
1.3.1	Janus kinase structure and influence on receptor dimerization.....	9
1.3.2	STAT structure and dimerization dependent activation.....	14
1.3.3	USP18 and ISG15 regulate type I IFN receptor dimerization.....	18
1.4	Methodologies for investigating protein-protein interactions.....	22
2	Objective	25
2.1	Strategies	26
2.1.1	GFP protein tags as generic pull-down targets	26
2.1.2	Antibody-related protein binders	26
2.1.3	Micropatterned surface architectures.....	28
2.1.4	Generic nanobody live cell micropatterning assay.....	30
2.1.5	<i>In situ</i> single cell pull-down (SiCPull) assay.....	32
2.1.6	Bimolecular fluorescence complementation in pull-down assays.....	34
3	Materials and Methods.....	36
3.1	Molecular Biology.....	36
3.1.1	Mammalian cell culture and transfection.....	36
3.1.2	Plasmid generation	36
3.1.3	Protein purification.....	37
3.2	Synthesis of PLL-PEG derivatives	37
3.2.1	HaloTag ligand-functionalized poly-L-lysine-graft-(polyethylene glycol) copolymer (PLL-g-PEG-HTL).....	37
3.2.2	RGD-functionalized poly-L-lysine-graft-(polyethylene glycol) copolymer (PLL-g-PEG-RGD)	38
3.3	Stamp manufacturing and microcontact printing	39
3.4	Fluorescence microscopy and data analysis.....	40
3.4.1	Total internal reflection fluorescence microscopy (TIRFM)	40
3.4.2	Bait specific fluorescence contrast analysis.....	41
3.4.3	Fluorescence recovery after photobleaching (FRAP)	43

3.4.4	Single Cell Pull-down (SiCPull) to characterize interaction dynamics	44
3.4.5	Single molecule single cell pull-down (SM-SiCPull)	45
3.4.6	Single molecule localization and data analysis	46
4	Results.....	47
4.1	Micropatterned surface architectures.....	47
4.1.1	Generic nanobody live cell micropatterning.....	47
4.1.2	Immobilization of mEGFP in an anti-GFP NB micropattern.....	48
4.2	Nanobody live cell micropatterning.....	49
4.2.1	Characterizing the interaction of USP18 and ISG15.....	49
4.2.2	Structural investigation of individual USP18 and ISG15 domains	52
4.2.3	Resolving USP18-ISG15 interaction dynamics via FRAP	55
4.2.4	Nanobody live cell micropatterning to examine cytosolic competition	56
4.2.5	Directly immobilizing STAT2 as bait for live cell micropatterning.....	60
4.2.6	Excluding direct interactions between STAT2 and ISG15	61
4.2.7	Investigating competition at the interferon receptor.....	62
4.2.8	N-terminus of USP18 is required for STAT2 binding.....	64
4.2.9	Split two-hybrid nanobody live cell micropatterning	65
4.2.10	STAT2 prevents fluorescence complementation by USP18-ISG15	67
4.3	<i>In situ</i> single cell pull-down (SiCPull).....	69
4.3.1	<i>In vitro</i> capturing of mEGFP into anti-GFP NB micropatterns	69
4.3.2	Specific single cell pull-down	70
4.3.3	Investigating STAT protein interaction dynamics via SiCPull.....	71
4.3.4	Single molecule micropatterning for investigating stoichiometry.....	73
4.3.5	Single molecule analysis workflow	75
4.3.6	Stoichiometry of STATs following type I IFN stimulation.....	78
4.3.7	Selective analysis of complemented receptor-kinase protein complexes... 80	
5	Discussion and Conclusions	82
5.1	Investigating type I IFN interactions via generic nanobody live cell micropatterning.....	82
5.1.1	Competition between STAT2 and negative feedback regulators USP18 and ISG15	84
5.1.2	Nanobody live cell micropatterning as a robust pull-down method	86
5.1.3	Two-hybrid nanobody pull-down assays to investigate distinct complexes	88

5.2	SiCPull for background-free investigation of interaction dynamics.....	89
5.2.1	Single molecule SiCPull to investigate cytosolic STAT and JAK stoichiometry 91	
5.2.2	Incorporating the two-hybrid approach into SM-SiCPull	94
5.2.3	Good analysis practice and workflow of SM-SiCPull.....	95
6	Appendix.....	98
6.1	References.....	98
6.2	List of Figures	107
6.3	Abbreviations.....	109
7	Publications	111
8	Curriculum vitae.....	112
9	Declaration.....	113

1 Introduction

1.1 The Protein Puzzle

We are currently living in one of the most exciting times in terms of medical and biological research, which is defined by an abundance of new insights and data. Recent progressions are fueled by increasingly modern, high-throughput methodologies, such as next-generation sequencing for genomics [1-3] and mass spectrometry-based analysis for proteomics [4-6]. Just in 2021, DeepMind's AlphaFold revolutionized structural biology by utilizing deep-learning for protein structure predictions [7, 8]. Importantly, such feats required a tremendous deal of effort only a few decades ago. Similar to a genome, which represents the genetic make-up of an organism, a proteome is the entirety of all proteins of a living being, a tissue, a cell, or even a cell compartment, which are, or can be, expressed by the genome under precisely defined conditions and at a specific point in time. Generally speaking, the genome serves as the blueprint of life, whereas the proteome is quite literally its transcription, and serves to perform and regulate the functions of life.

Already in 2001, the Human Genome Project was announced complete, having identified ~20.000 genes [9], which encode for roughly the same number of proteins. However, not only did the human reference genome only focus on the euchromatic region, leaving the remaining 8% of the heterochromatic region undetermined [10], it was also recognized via RNA-sequencing that alternative splicing, alternative transcription initiation and alternative transcription termination occurred far more often than anticipated, affecting up to 95% of human genes [11, 12]. Depending on the source material, it is currently estimated that the human body contains between 80.000 – 400.000 different proteins, or even more than >1.000.000 proteins when accounting for posttranslational modifications. However, these proteins are produced in different cell types and points in time, and with roughly 250 different cell types in the human body, these proteins are thus organized in at least 250 different proteomes. Lastly, proteomes are also depending on an organism's age, diet and health, as well as medications or other environmental influences. Simply finding or identifying each piece of the protein puzzle is therefore only the first step, as all interacting proteins within a proteome still need to be pieced together. This is because the plethora of cellular functions is governed by vast networks of protein-protein interactions (PPIs), which exhibit regulatory mechanisms through core features such as

affinity and avidity, or by acting as co-factors and competitors. Even excluding other influencing factors such as protein expression level and protein turnover, these mechanisms allow highly important and relatively redundant systems such as signaling pathways to generate a plethora of distinct cellular responses. Therefore, cellular functions such as cell growth, programmed cell death and immune response not only require a precisely tuned activity level. Dysregulation of such a tightly controlled network often culminates in catastrophic repercussions such as pathogen susceptibility, autoimmune diseases, or cancerous cell growth.

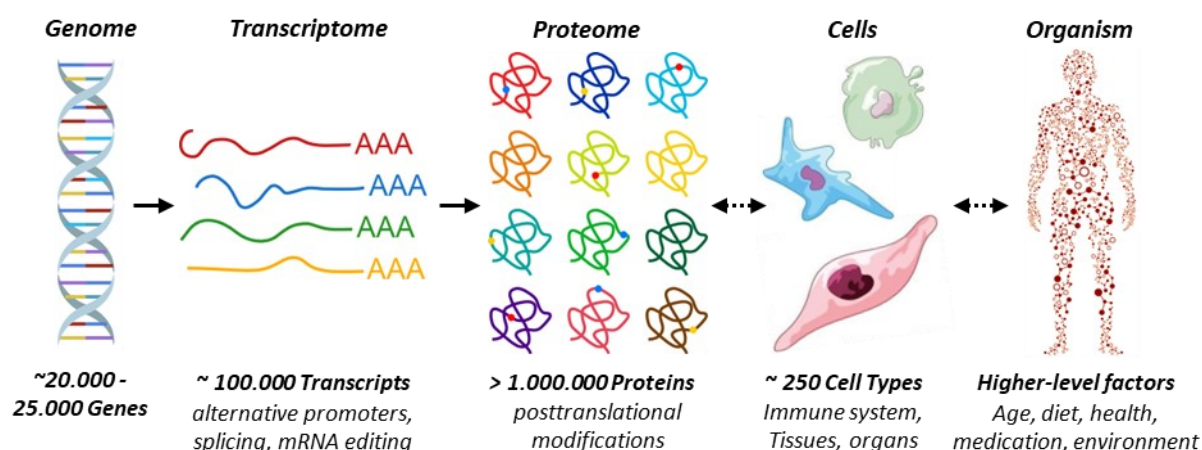


Figure 1: Genomic and proteomic complexity. The human genome is estimated to consist of ~20.000 – 25.000 genes, which yield about 100.000 transcripts, translating into >1.000.000 proteins including posttranslational modifications (PTM, coloured dots). Transcription and expression depend on the specific cell of >250 cell types and are influenced by higher-level factors of the organism.

For these reasons, PPIs not only need to be validated but also require thorough in-depth characterizations of their interaction dynamics, stoichiometry and interacting partners, especially within their biological context. Such fundamental biological research on the protein level is literally of vital importance, as it is enabling the development of highly specific drugs, even for targeting mutations related diseases that were thought undruggable up until a few years ago. Such a recent example is the mutant KRAS^{G12C} inhibitor Sotorasib, which in mid-2021 and in January 2022 became the first ever to be approved KRAS inhibitor in the US and Europe, respectively. This inhibitor was designed to specifically and irreversibly bind mutant KRAS^{G12C}, which is occurring in 13% of non-small-cell lung cancers (NSCLC) [13, 14], enabling treatment of “undruggable” cancer types, with even more inhibitors directed against KRAS and other mutant kinases already appearing on the horizon [15-17]. This recent example illustrates how the progress made in biology further inspires the development of advanced methodologies, with which it will be possible to characterize unresolved PPIs and to tackle the molecular mechanisms involved in cellular functions, thus step-by-step piecing together the protein puzzle.

1.2 Cytokine signaling pathways

Cytokines are a key factor of cellular signaling, regulating hematopoiesis and immunological homeostasis while employing only a select few key components for downstream signaling in many different pathways [18]. Mechanistically, the signaling cascade is activated by cytokine-induced homo- and heteromerization of their cognate receptors [19, 20]. Class I and class II cytokine receptors lack intrinsic enzymatic activity, and activate downstream signaling via associated Janus family tyrosine kinases (JAK). These in turn phosphorylate receptor tyrosine residues and transcription factors of the signal transducers and activators of transcription (STAT) family, thus inducing their dimerization and subsequent translocation into the nucleus [21] (**Figure 2**). Importantly, JAKs are responsible for most if not all of the cellular responses to peptide hormones and cytokines and are thus paramount for homeostasis and immunity [22]. However, the JAK-STAT signaling pathway is a relatively redundant system, for being employed by over 40 different members of class I/II cytokine receptor families, while only relying on 4 JAK family members (JAK1, JAK2, JAK3, TYK2) and 7 STAT family members (STAT1, STAT2, STAT3, STAT4, STAT5a, STAT5b, STAT6) for downstream signaling [23]. Making things even more complex, individual cytokines also exhibit pleiotropy, by inducing a wide range of biological responses in different cell types, leading to a strong crosstalk and overlap of their signaling pathways. It is therefore quite impressive that the select few key components of JAK-STAT signaling are able to achieve a high degree of signaling plasticity, while maintaining their functional selectivity [24-26]. This apparent bottleneck nevertheless achieves differential signaling for the plethora of different cytokine families, by inducing highly specific gene expression patterns and cellular responses, which all require precise regulation of the JAK-STAT signaling [27].

To this end, different strategies are employed which regulate cytokine signaling on many levels. Among the more straightforward regulations are cellular receptor surface concentrations and cytokine affinity, which both directly correlate to signaling strength and thus are the first step to regulate the responsiveness of different cell types. In line with this notion, it was recently demonstrated that binding of STATs to receptor phosphotyrosine motifs accounts for altered cytokine responses and that in turn receptor and STATs concentrations greatly influence cytokine responses, leading to functional pleiotropy of cytokine signaling [28]. Additionally, intracellular mechanisms serve to efficiently attenuate cytokine signals and are thus regulating both the signal amplitude

and duration, which is a crucial aspect in maintaining cellular functions while preventing sustained firing of the cytokine signals [29]. Acting as an off-switch, three main families of negative feedback regulators have been identified, including protein-tyrosine-phosphatases (PTP) which counteract tyrosine phosphorylation and thus activation, protein inhibitors of activated STAT (PIAS) which interact with STATs to suppress their DNA-binding activity, as well as suppressors of cytokine signaling (SOCS) which as a general rule are induced by and inhibit many cytokine-signaling systems in a classic negative-feedback loop [29] (**Figure 2**). However, some cytokine signaling pathways feature a unique negative feedback regulation, as demonstrated by the type I interferon (IFN) signaling pathway, which serves as the model system of this work.

To summarize, class I and II cytokines exhibit pleiotropy and signaling plasticity, although the JAK-STAT signaling pathway consists of only 4 JAK (JAK1, JAK2, JAK3, TYK2) and 7 STAT (STAT1, STAT2, STAT3, STAT4, STAT5a, STAT5b, STAT6) family proteins, which in turn requires additional regulatory mechanisms, such as negative feedback regulators. Cytokine signaling pathways thus illustrate the importance of in-depth characterization of PPIs to unravel the intricate interactions and mechanistic regulations.

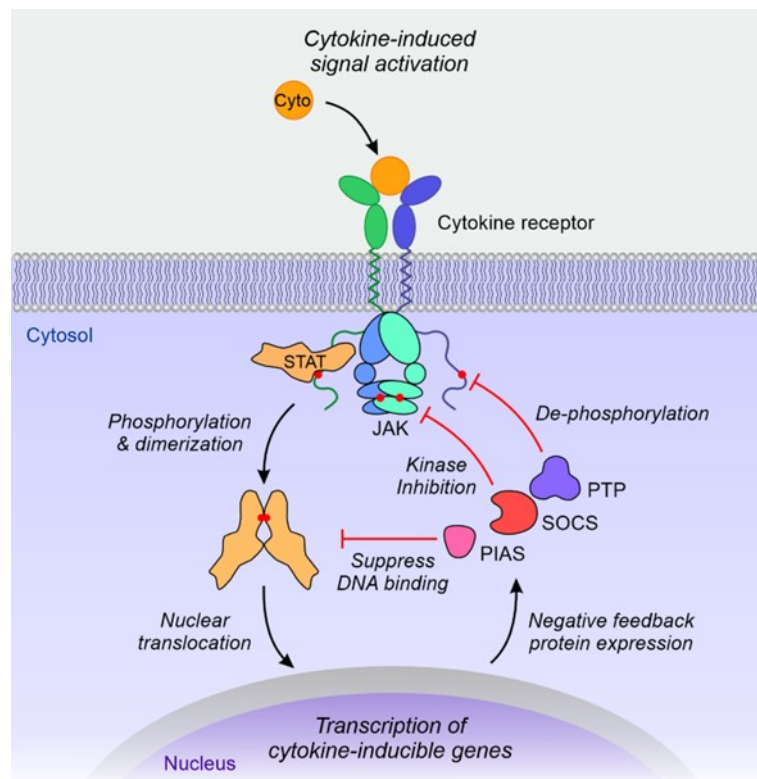


Figure 2: Cytokine-induced JAK-STAT signaling pathways. Ligand-induced receptor dimerization enables associated JAKs to phosphorylate (red dots) receptor tyrosine residues and STATs. Activated STATs translocate into the nucleus, leading to the transcription of cytokine-inducible genes, including negative feedback regulators PIAS, SOCS, PTP, which generally down-regulate the JAK-STAT signaling pathway. Figure based on [18].

1.3 Type I interferon signaling pathway

Among the class II cytokine receptors, the prominent type I interferon (IFN) receptor serves as the model system of this work, representing a highly relevant model system of JAK-STAT signaling and its regulation. IFNs play a crucial role in the immune response of vertebrates against viral and intracellular bacterial infections [27, 30] and serve as a prime example for differential cytokine signaling via their α/β differentiation [31, 32].

Being identified as an antiviral factor in 1957, these cytokines have been named for their interference with viral growth [33], by being secreted from infected cells and thus leading to their elimination and the protection of surrounding cells. Mechanistically, IFNs mediate antiviral and antiproliferative cellular responses by up-regulation of interferon-stimulated genes (ISG) [34] and trigger an immune response by regulating differentiation and function of immune cells such as natural killer cells (NK) and cytotoxic T cells (CTLs)[30]. The family of human type I IFNs comprises 16 members including IFN β , IFN ϵ , IFN κ , IFN ω and 12 subtypes of IFN α , which all bind to a shared cell surface receptor consisting of two heterodimeric subunits IFNAR1 and IFNAR2 [35]. Regarding the redundancy of cytokine signaling in general, binding of different IFN subtypes yield differential signaling, albeit solely relying on the JAK-STAT signaling to achieve unique gene expression patterns as a signaling response [27].

Simply put, the signaling itself is initiated via binding of IFN to the higher affinity subunit IFNAR2, followed by recruitment of the lower affinity subunit IFNAR1, thus leading to the formation of a ternary complex, setting in motion a cascade of activation via phosphorylation events [36-38] (**Figure 3**). Specifically, the receptor associated Janus kinases JAK1 (IFNAR2) and TYK2 (IFNAR1) are brought into close proximity of each other, leading to their activation by enabling reciprocal trans-phosphorylation [19, 21] (**chapter 1.3.1**). These activated Janus kinases in turn phosphorylate specific tyrosine residues on the receptor chains, which serve as binding sites for the src-homology 2 (SH2) domains of STATs. In case of type I IFN signaling, STAT1, STAT2 and STAT3 are then activated by phosphorylation of a conserved tyrosine residue, facilitating their homo- and heterodimerisation through reciprocal SH2-domain/pTyr interactions [39]. These activated or phosphorylated STAT (pSTAT) homo- and heterodimers are then actively transported into the nucleus via binding to importin- α 5 [40], where they activate transcription of specific sets of genes (**Figure 3**) [21, 41].

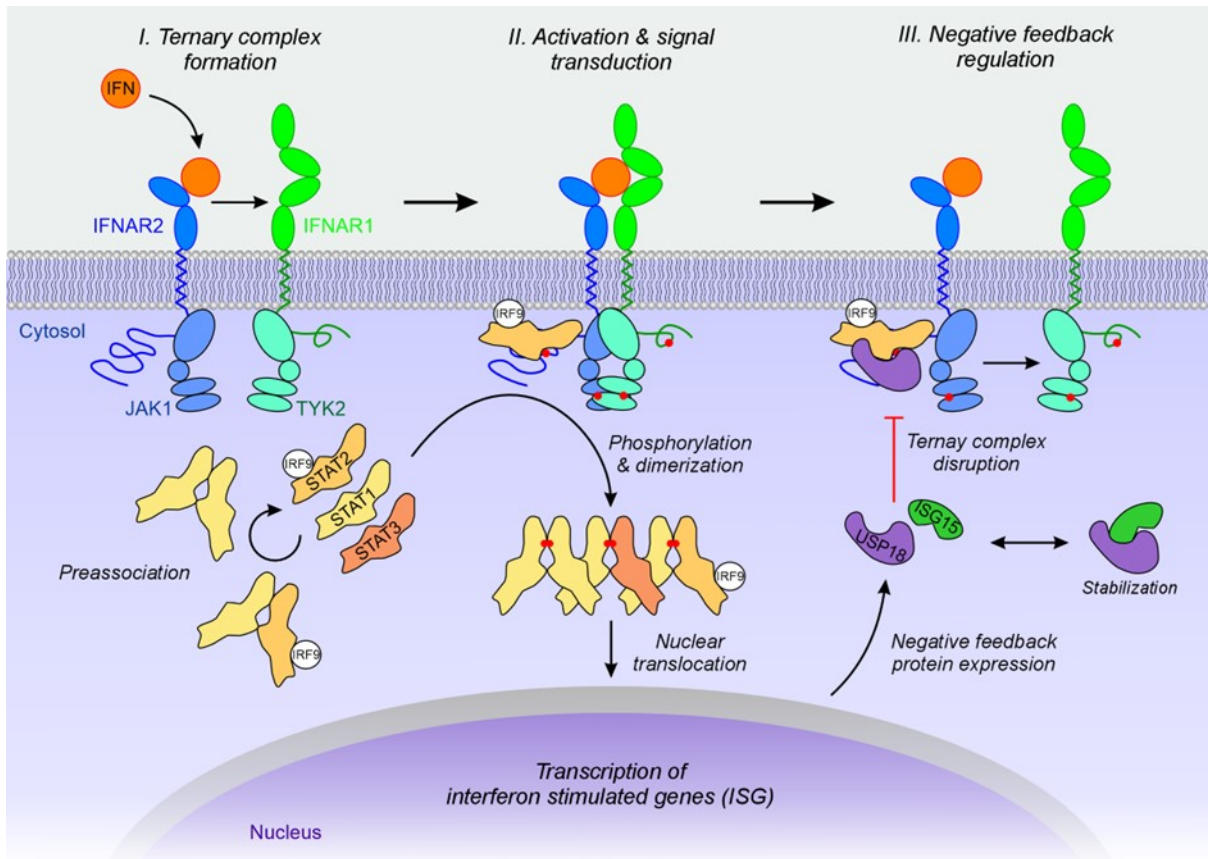


Figure 3: Type I IFN signaling pathway. Schematic representation of type I IFN signaling. (I) Binding of IFN to the high affinity subunit IFNAR2 leads to subsequent binding of the low affinity subunit IFNAR1, resulting in ligand-induced ternary complex formation. (II) Receptor associated JAK1 and TYK2 are brought into close proximity and undergo reciprocal trans-phosphorylation, followed by specific tyrosine phosphorylation on the receptor chains, acting as binding sites for STAT SH2 domains. Phosphorylation is indicated as red dots. Cytosolic STAT proteins, which also preassociate in absence of IFN stimulation, are then recruited to and phosphorylated by the kinases. This leads to their canonical homo- and heterodimerization as activated transcription factors, e.g. ISGF3 (STAT1+STAT2+IRF9), followed by their dimerization and phosphorylation-dependent translocation into the nucleus. Transcription of ISGs leads to up-regulation of USP18 and ISG15 as negative feedback proteins. ISG15 indirectly affects negative regulation by stabilizing cytosolic USP18 by preventing its proteolytic degradation. USP18 itself is recruited to IFNAR2 via STAT2 and disrupts the ternary complex stability, serving as an off-switch for signaling.

Heterodimerization of pSTAT1 and pSTAT2 interacting with IFN regulatory factor 9 (IRF9, formerly p48) acts as the heterotrimeric interferon-stimulated gene factor 3 (ISGF3), whereas common pSTAT1 activation and its homo- and heterodimerization acts as a more general response to various cytokines and even growth factors [42, 43]. Upon nuclear translocation, ISGF3 binds to IFN-I-stimulated response elements (ISRE), leading to the activation of transcription of over 300 interferon-stimulated genes (ISGs), with the abundance and phosphorylation kinetics of ISGF3 components regulating the nature and duration of the type I IFN responses [44]. In absence of STAT1, preformed complexes of pSTAT2-IRF9 control basal expression of ISGs [45], and can also lead to prolonged ISGF3-like transcriptional responses and antiviral activity, potentially substituting for the role

of ISGF3 [44] and underlining the importance of STAT2 in type I IFN signaling. It is however noteworthy that even non-phosphorylated STATs constitutively shuttle between the cytosol and nucleus, where they activate transcription of sets of genes different from phosphorylated STATs and that STATs are largely present as dimers, or as high molecular mass “statosome” complexes [46] (**chapter 1.3.2**). Phosphorylation and active translocation into the nucleus via importin- α 5, as well as the subsequent activation of transcription of ISGs are thus specific responses for type I IFN signaling and another manifestation of cytokine signaling plasticity.

With its highly critical role in coordinating early immune responses, type I IFN signalling is regulated at diverse layers. Notably, binding affinities of the different IFN subtypes are fine-tuned to regulate signal transduction and thus the differential biological activity [38, 47], and especially antiproliferative responses have been shown to be dependent on ternary complex stability [48]. With the ternary complex formation following a two-step assembly, caused by binding of IFN to the higher affinity subunit IFNAR2, followed by the recruitment of the lower affinity subunit IFNAR1 [36-38], the lower affinity interaction critically regulates ternary complex stability. It has been demonstrated that increase of binding affinities towards the low-affinity subunit IFNAR1 increases ternary complex stability, as shown by comparing IFN α 2 with IFN β and IFN α 2-YNS [49], an IFN α 2 mutant that is like IFN β featuring a \sim 50-fold increased binding affinity towards IFNAR1 [50], thus increasing ternary complex stability significantly. In turn, this also leads to differential receptor internalization rates, STAT phosphorylation profiles and downstream gene expression patterns, illustrating the α/β differential regarding antiproliferative activities caused by different ligands [50].

In line with this notion, differential signaling can be regulated quite simply through the cell surface receptor concentration of a specific cell type, as seen for the interferon α/β differential [31, 32]. On the one hand, antiviral activity is responsive even at low receptor expression levels and low ligand concentrations. On the other hand, antiproliferative activity requires not only high receptor expression and ligand concentrations, but also the higher binding affinity of IFN β for long-term stimulation [32, 39]. Antiviral activity can thus be categorized as an early response requiring a relatively low stimulation and is induced after a few hours of IFN stimulation, whereas antiproliferative activity serves as a late response, requiring up to several days of continuous IFN stimulation [32].

In part, this is due to the fact that signal propagation not only induces the expression of immunological response proteins, but also of regulatory feedback proteins aiming to mitigate IFN signaling activity [19, 51, 52]. As previously mentioned, typical negative feedback regulators are for example harnessing phosphatase activity to dephosphorylate TYK2 (protein-tyrosine phosphatase 1B, PTP1B), inhibit kinase activity of TYK2 and JAK1 (suppressor of cytokine signaling, SOCS1, SOCS3), or prevent DNA binding of activated STATs (protein inhibitors of activated STAT, PIAS1). Whereas these negative regulators are generally affecting JAK-STAT signaling, the ubiquitin-specific protease 18 (USP18) exclusively inhibits type I IFN signaling by disrupting the ligand-induced ternary complex formation in a non-competitive manner (**Figure 3**) [19, 52, 53]. Alongside USP18, the di-ubiquitin-like protein ISG15 (interferon-stimulated gene 15) is also upregulated in response to IFN stimulation, and is either conjugated to target protein lysine residues in a process named ISGylation [54-56], or exists as a free intracellular or extracellular molecule. In its free intracellular state, ISG15 was shown to stabilize USP18 by preventing its proteolytic degradation, thus directly influencing the long-term negative feedback regulation [57]. To this end, both negative feedback proteins USP18 and ISG15 are unique regulators for type I IFN signaling, in turn leading to a significant desensitization of IFN α 2 (see **chapter 1.3.3**).

In conclusion, the intracellular signal propagation of the type I IFN signaling pathway is heavily reliant on a complex interplay of cytosolic protein-protein interactions, including the JAK-STAT proteins, which are commonly employed by cytokine signaling pathways, as well as the negative feedback regulators USP18 and ISG15, which are unique for type I IFN. Unraveling these interactions requires a thorough characterization, including interaction kinetics and complex stoichiometry, which are largely part of this work. To this end, all of these investigations should be carried out within biological context, thus *in vivo* or *in situ*, while in presence of co-factors and competitors and if feasible also at the single molecule level for stoichiometric investigation of protein complexes. First, however, such quantification requires a basic understanding of the structure and domains of these proteins, which dictate not only their cellular function, but also their protein-protein interactions.

1.3.1 Janus kinase structure and influence on receptor dimerization

Constitutively associated tyrosine kinases are required to provide tyrosine kinase activity for the IFNAR subunits of type I IFN signaling [58]. Following the IFNAR ternary complex formation, the Janus kinases JAK1 (IFNAR2) and TYK2 (IFNAR1) activate the signal transduction through a cascade of reciprocal trans-phosphorylation of the JAKs [19, 21], followed by phosphorylation of specific tyrosine residues on the IFNAR chains, and on the STAT proteins as well [39]. Interestingly however, the four Janus kinases JAK1, JAK2, JAK3 and TYK2 are also employed by other cytokine and even growth factor receptors [59], all leading to different cellular responses and thus illustrating that JAKs are able to achieve signal plasticity. Moreover, they even exert a regulatory influence on receptor dimerization, as will be shown later in this chapter.

Regarding their structure, Janus kinases are 120-140 kDa large proteins which all share a similar domain structure. They feature an N-Terminal FERM (four-point-one, ezrin, radixin and moesin) domain and src-kinase SH2 domain (SH2) involved in receptor binding (**Figure 4a, b**), as well as the C-terminal pseudokinase (PK) and tyrosine kinase (TK) domains, which both modulate the kinase activity (**Figure 4c**)[60].

FERM domains are regularly employed in proteins in order to bind to the membrane-proximal region of single transmembrane domain proteins. Consisting of the three subdomains F1, F2 and F3, the clover-shaped FERM domain features an ubiquitin-like fold in the N-terminal subdomain F1, a shared fold of an acyl-CoA binding protein in F2, as well as a structurally similar pleckstrin homology (PH) domain in F3 [61], which also allows non-covalent interaction with phospholipids [62].

Usually, SH2 domains bind specific motifs which contain phosphorylated tyrosine residues and are thus involved in protein-protein interactions. It was however shown via mutagenic analysis and structural alignment that the SH2 domains found in JAK1 and TYK2 do not fulfill a classical SH2 function. Instead, they play a structural role for receptor interaction and even up-regulation of receptor surface expression [63]. Moreover, JAKs have been demonstrated to play a non-enzymatic role in stable surface expression of receptors, masking endocytic motifs on IFNAR and even preventing their proteolytic downregulation [22, 64-66]. In line with these findings, a co-localization analysis clearly demonstrated that associated JAKs stabilize the ternary IFNAR complex and that receptor dimerization dynamics also act as a regulatory valve for type I IFN signaling [19].

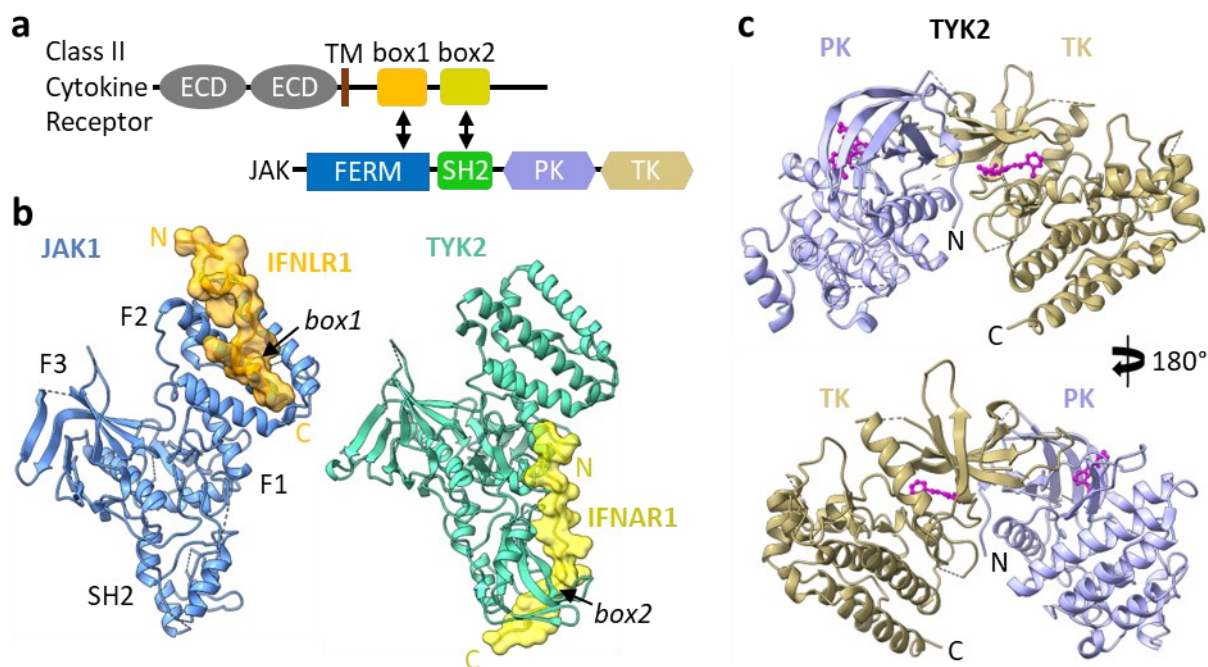


Figure 4: FERM and SH2 domains interact with receptor box motifs. (a) Linear domain structure of class II cytokine receptors and JAKs. Receptors feature extracellular domains (ECD), transmembrane domain (TM), and box1 and box2 motifs, and JAK features FERM and SH2 domains, and pseudokinase (PK) and tyrosine kinase (TK) domains. (b) Comparison of JAK1 (blue) bound to IFNLR1 box1 motif (orange) and TYK2 (teal) bound to IFNAR1 box2 motif (yellow). Binding of box1 is mediated by the FERM F2 subdomain and binding of box2 is primarily mediated by the SH2 domain. (c) Structure of the pseudokinase (light-blue) and kinase (light-brown) complex. The kinase inhibitor molecule compound 7012 is shown in the active site as ball-stick models (purple). Structure is rotated 180°, to aid consideration of the interaction interface. Figure ‘a-b’ based on [67], PDB: 5IXD (JAK1) and 4PO6 (TYK2). Figure ‘c’ based on [68], PDB: 4OLI.

Interactions with JAKs are mediated through kinase binding domains, which are located in the membrane-proximal region of cytokine receptors and contain two conserved motifs: a proline-rich sequence often preceded by hydrophobic residues called box1, followed 10-40 amino acids downstream by a cluster of hydrophobic residues often preceded by charged residues called box2 (**Figure 4a, b**) [69]. Both box1 and box2 have been demonstrated to mediate the vital link between extracellular ligand-mediated receptor dimerization and JAK activation [60], with the box1 motif being more significant for signal activation while seemingly playing a minor role in kinase association, and the box2 motif majorly contributing to kinase binding [70, 71]. Moreover, crystal structures of IFN- α receptor 1 (IFNAR1) bound to human TYK2 FERM-SH2 domains described the molecular basis of box2 recognition [72], and crystal structures of IFN- λ receptor 1 (IFNLR1) bound to the human JAK1 FERM- SH2 domains revealed an interaction site in the JAK1 FERM that accommodates the box1 motif (**Figure 4c**), which acts as the primary driver for JAK1 interaction, while the box2 motif further stabilizes the JAK1-IFNLR1 complex [67].

Most importantly, the presence of multiple receptor binding sites on JAKs, in combination with a high target receptor sequence diversity, demonstrate that signaling outputs are resulting from these differences in structure and affinity between JAKs and bound receptors [67]. Regarding their catalytical activity, JAKs feature both a pseudokinase domain (PK) and a classical tyrosine kinase domain (TK), with the former acting as an autoinhibitory domain, holding the kinase domain in an inactive state until cytokine binding initiates receptor dimerization and stimulates transition into an active state [68]. An autoinhibitory crystal structure of TYK2 has demonstrated that the PK and TK domains are interacting near the kinase active site (**Figure 4c**) and it was found that most reported mutations in cancer-associated JAK alleles cluster in or near this interface [68]. Among these is the oncogenic JAK2 V617F (VF) mutation, which causes hyperactivity through constitutive activity of the tyrosine kinase [73, 74].

Following up on this, Janus Kinase influence on activation of homodimeric class I cytokine receptors and dysregulation caused by oncogenic mutations were previously demonstrated by our workgroup [20], utilizing live-cell single-molecule colocalization and co-tracking of individual receptor subunits of either the Thrombopoietin receptor (TpoR), the Erythropoietin receptor (EpoR), or the growth hormone receptor (GHR). It was established in 2020 that the prototypic homodimeric class I cytokine receptors EpoR, TpoR, and GHR are only dimerized by their ligand (**Figure 5**) [20], contradicting the previous view of pre-dimerized receptors that are activated by a ligand-induced conformational change [75].

Ligand-induced dimerization was clearly demonstrated as the activation mechanism of these receptors, but also the regulatory role of JAK2 for ligand-induced receptor dimerization under physiological expression levels, as the presence of JAK2 elevated the relative co-locomotion of TpoR, EpoR and GHR, while also excluding downstream signal activation by addition of ruxolitinib, a JAK2 inhibitor [20]. Moreover, receptor dimerization was attributed to the intermolecular PK-PK interaction of JAK2, by quantifying the TpoR dimerization in presence of different JAK2 truncations [20]. Whereas the TK domain truncation (JAK2 Δ TK) was able to maintain dimerization, the TK and PK domain truncation (JAK2 Δ PK-TK) abrogated dimerization [20]. Also, it was shown that the oncogenic JAK2 V617F mutation is sufficient enough to drive ligand-independent receptor dimerization [20].

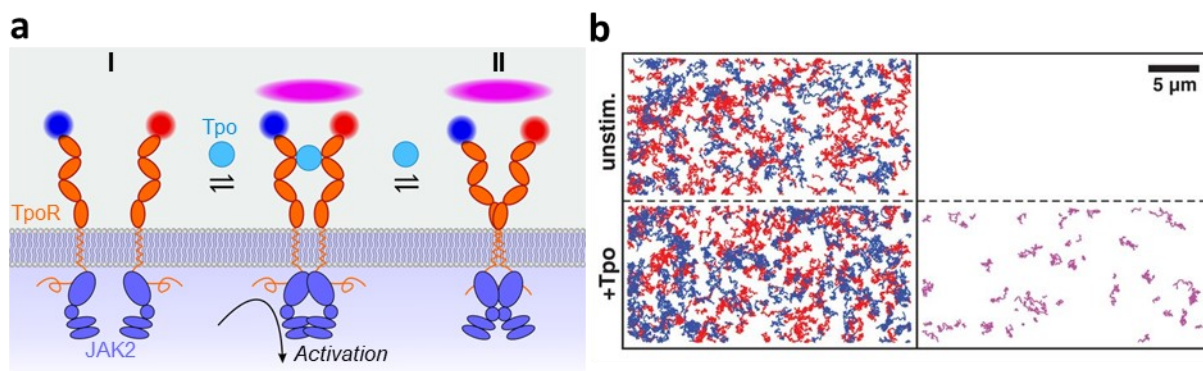


Figure 5: Homodimeric cytokine receptor activation. (a) Ligand-induced cytokine receptor dimerization (I) versus ligand-induced conformational change (II). (b) TpoR tracking (left) and co-tracking analysis (right). Individual fluorescence-labeled (blue, red) TpoR subunits, and co-trajectories (magenta), before (top) and after (bottom) addition of Tpo. For wildtype TpoR, addition of ligand clearly induces receptor dimerization (I), whereas no ligand-independent dimerization is observable under single molecule conditions for wildtype TpoR (II). Figure adapted from [20].

Importantly, it was concluded that the assembly of the signaling complexes is controlled by additive interactions, with energetic contributions deriving from ligand-induced dimerization, JAK2 PK-PK domain interactions, as well as transmembrane and juxtamembrane interactions [20].

Moreover, a recent cryo-EM structure from 2022 showed an active JAK1-IFN λ R1 complex, giving further insights into JAK dimerization. To this end, mouse JAK1 (for high expression in insect cells) was utilized, together with a cytokine receptor intracellular domain (ICD) containing the Box1/Box2 domains from interferon λ receptor 1 (IFN λ R1), as well as the JAK1-V657F mutation (analogous to human JAK2-V617F) to stabilize the activated state of the complex (**Figure 6**) [76]. When comparing the V657F cryo-EM structure with a model of WT V657, it was found that the smaller valine side chain results in an unfilled pocket within the PK-PK dimer interface, whereas V657F enhanced structural and hydrophobic complementarity of the dimer interface (**Figure 6b**), thus enhancing the tendency of the PK domains to naturally dimerize [76]. These findings were in line with the previous JAK2-TpoR study [20], which has shown that WT JAK2 requires the PK domain to enhance ligand-induced dimerization. Strikingly, the JAK1-IFN λ R1 cryo-EM structure was also aligned with the previously reported structure of the autoinhibited TYK2 PK-TK domain fragment (**Figure 4c**) [68], showing a “closed” autoinhibitory JAK monomer in which the TK is folded back on the FERM-SH2 domain, obscuring the activation loop and kinase active site (**Figure 6a**) [76]. This yielded a two-step model of JAK activation, featuring the “closed” conformation, which is sterically incompatible with JAK dimerization (**Figure 6a, left**), and an “open” conformation (**Figure 6a, middle**).

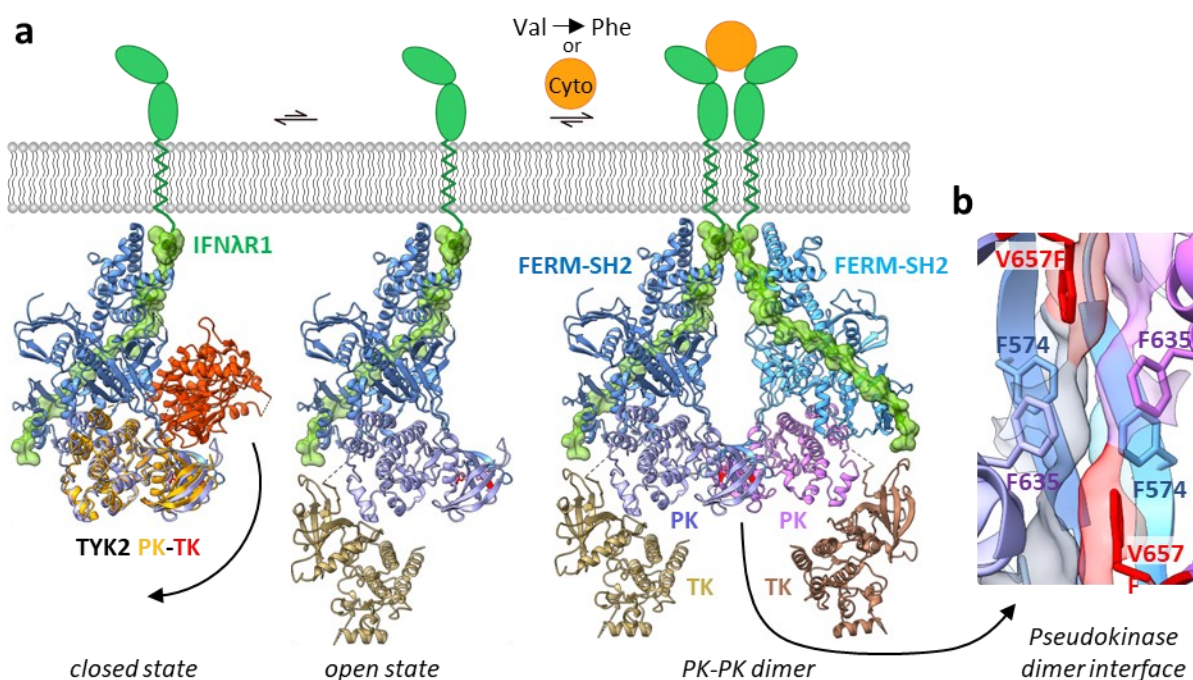


Figure 6: Two-step model of JAK activation. (a) Crystal structure of the PK-TK domains (orange, red) from TYK2 (PDB: 4OLI) [68] overlaid on the cryo-EM structure of dimeric JAK1-IFN λ R1. FERM-SH2: blue, PK: blue-magenta, TK: brown, IFN λ R1: green. Dynamic equilibrium between the autoinhibitory “closed” state (left) and a partially active “open” state (middle), with exposed PK domain and SH2-PK linker to allow for JAK dimerization. Cytokine-induced receptor dimerization or Val to Phe mutation facilitates formation of the PK-PK dimer (right), sterically preventing autoinhibition and enabling the kinase domains phosphotransferase activity. (b) Cross-section view of the PK-PK interface from the bottom view, with the V657F cryo-EM structure. Oncogenic V657F (red) enhances shape complementarity of the PK dimerization interface. Figure based on [76], PDB: 7T6F.

Activation via cytokine-induced receptor dimerization or the VF (Val to Phe) mutation then shifts the equilibrium away from the closed autoinhibitory state to the open state, facilitating JAK transphosphorylation (**Figure 6a, right**) [76]. According to this model, it was predicted that oncogenic mutations either destabilize the autoinhibited state, or stabilize the dimeric active state, which is in line with a paired analysis of JAK2 phosphorylation and TpoR dimerization at physiological expression levels, [20]. Mapping of the two identified groups of mutations onto the active JAK1-IFN λ R1 structure showed distinct clustering: Mutants which enhance JAK2 phosphorylation without affecting receptor dimerization cluster at the FERM-SH2-PK-TK interface, suggesting that destabilizing this interdomain interaction releases JAK from autoinhibition, whereas those mutations which enhance both JAK2 phosphorylation and receptor dimerization cluster at the PK-PK interface, enhancing structural and hydrophobic complementarity [76].

To summarize, cytokine receptor dimerization, JAK activation, and cytokine signaling as a whole, are strongly controlled by the inter- and intramolecular interactions of functional and regulatory JAK domains, which can be severely dysregulated by oncogenic mutations such as the well-known Valine to Phenylalanine mutation. By correlating structural and functional data, which were acquired closer to physiological conditions, many insights have been gained in recent years that even refuted the dogma of pre-dimerized cytokine receptors, and instead established ligand-induced dimerization as a model. These findings especially underline the importance of performing experiments under biological context, and close to physiological expression levels.

1.3.2 STAT structure and dimerization dependent activation

The STAT family is the hallmark of cytokine signaling and thus a prominent example for induced oligomerization of cytosolic effector proteins. STATs are canonically tyrosine-phosphorylated upon cytokine stimulation and regulate binding via their SH2 domains, forming homo- and heterodimeric transcription factors which act as a general response to various cytokines [77, 78]. These, along with the unique heterotrimeric interferon-stimulated gene factor 3 (ISGF3) consisting of STAT1, STAT2 and IRF9 [42, 43], translocate into the nucleus where they bind DNA in order to activate transcription and regulate gene expression [51].

Regarding their structure, biochemical, genetic and structural studies have identified seven STAT domains which are highly conserved in all mammals, including an N-terminal domain (ND), a coiled-coil domain (CC), a DNA-binding domain (DBD), a linker domain (LD), an SH2-domain (SH2), tyrosine activation domain (Y) and a transactivation domain (TAD) (**Figure 7**) [59]. Moreover, proteolytic cleavage identified three structurally independent moieties comprising of either the N-terminal domain, the C-terminal TAD domain, as well as a hydrophobic core fragment containing the CC, DBD, LD, SH2 and Y domains [79].

The N-terminal domain (ND, residues ~1-125) has been shown to direct homodimerization of inactive unphosphorylated STATs, as well as tetra- or oligomerization of pSTATs, enhancing cooperative DNA binding [59, 80-82]. The ND has also been postulated to be required for reorientation of STAT1 dimers, enabling dephosphorylation of STAT1 [83], as well as regulating nuclear import, as demonstrated by deletion of the ND and subsequent lack of nuclear translocation [84].

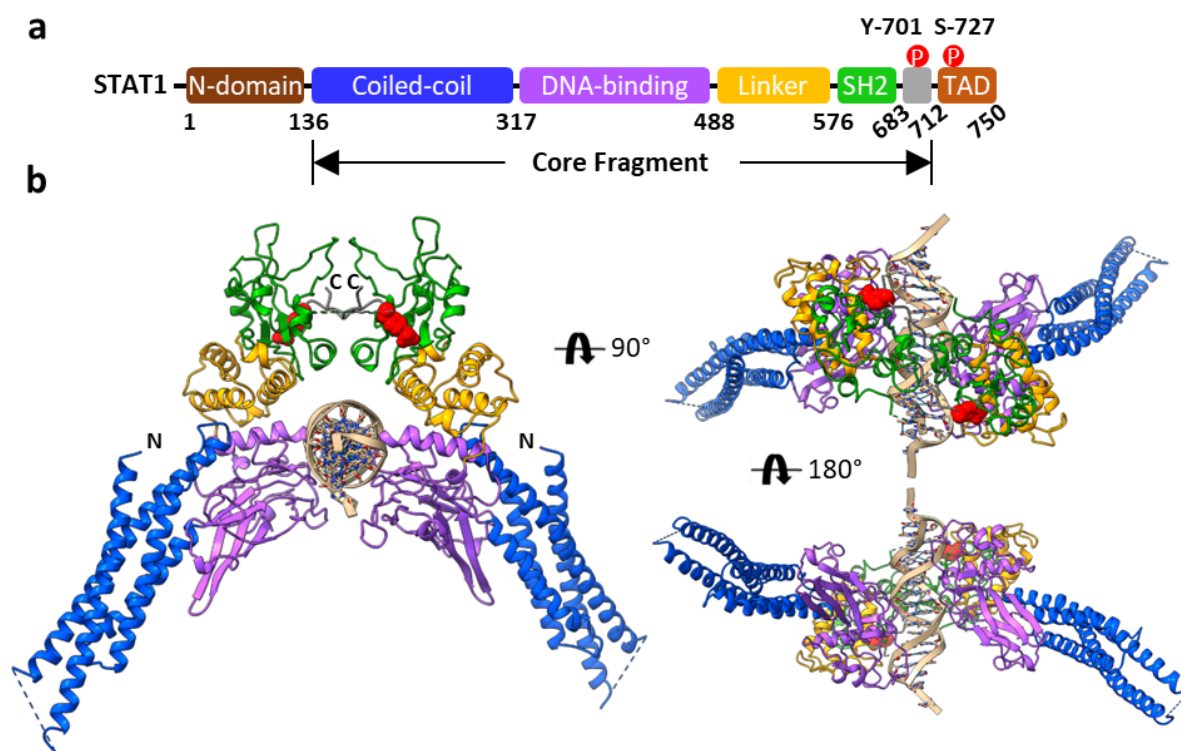


Figure 7: STAT1 domains and crystal structure in complex with DNA. (a) Scaled linear representation of STAT1 domains with corresponding amino acid residues. Phosphorylation sites Tyr-701 and Ser-727 are indicated as a red “P”, crystallized core fragment indicated by arrows. Scheme adapted from [80]. (b) Structural domains include the coiled-coil domain (blue), DNA-binding domain (purple), linker domain (orange), SH2 domain (green), as well as not-shown unstructured N-terminal domain and a transactivation domain (TAD). pTyr-701 is shown in a sphere representation (red). N and C termini of the STAT-1 core are labeled. The DNA backbone is shown in light-brown. Figure based on [85].

As the first domain within the core fragment, the adjacent coiled-coil domain (CC, residues ~135–315) represents a protein interacting domain, consisting of a four- α -helix bundle which provides a large hydrophilic surface and enables binding of regulators such as IRF9 to STAT2 (formerly p48) [86], as well as constitutive binding of STAT2 to IFNAR2 [87]. The CC is also involved in nuclear import and export of various STATs [88]. The DNA-binding domain (DBD, residues ~320–480) features a β -barrel immunoglobulin fold for DNA-binding with nanomolar avidity. The DBD also specifically regulates nuclear import and export of tyrosine phosphorylated STATs, by containing a nonclassical, conditional nuclear localization signal (NLS) which is only active in dimeric STATs, and a nuclear export signal (NES) [40, 89-91]. The conserved linker domain (LD, residues ~480–580) connects the DBD and the SH2-domain, and is mostly critical in stabilizing an appropriate conformation between these two domains [59, 92]. However, the most highly conserved domain within the STAT family is the SH2-domain (SH2, residues ~575-680), fulfilling the important roles of stimulation dependent receptor binding, as well as phosphorylation dependent homo- and heterodimerization, thus enabling DNA binding and activation of transcription [59, 88, 93].

The tyrosine activation domain (Y, residue ~700, STAT1 Y-701; STAT2 Y-690) is positioned adjacent to the SH2-domain and is precluding (intramolecular) self-association [59]. Lastly, the C-terminal transactivation domain (TAD, ~38-200 residues) varies greatly among the STAT family members, presenting an opportunity to associate with distinct transcriptional regulators such as CBP/p300 in IFN γ mediated STAT1 signaling [59, 92, 94], as well as STAT2 dependent ISGF3 signaling [95].

Regarding the activation of the 7 family members, STAT1, STAT2, STAT3, STAT5a and STAT5b are generally employed in response to type I IFNs, whereas STAT4 and STAT6 can only be activated in certain cell types [51]. Furthermore, it has also been indicated that variations of the basal and induced expression levels, as well as relative STAT concentrations, are shaping both cytokine function and immune responses [96]. Following their ligand-induced activation, pSTATs are dramatically shifted towards nuclear translocation, whereas inactive STATs are predominately localized within the cytosol [59]. This steady state is regulated by multiple NLS and NES signal motifs, which are recognized by importin- α 5 and CRM1 (chromosome region maintenance 1, or exportin1), respectively [40, 97].

In case of STAT1 and STAT2, recognition via importin- α 5 requires both tyrosine phosphorylation and dimer formation in the parallel orientation (**Figure 8**) [40, 89-91], illustrating the importance of STAT dimerization, proper structural orientation and phosphorylation as prerequisites for signal transduction. Mutations within these NLS and NES signal motifs cause inhibition of either import or export, as is the case with the STAT1 L407A mutation in the NLS, which is rendering phosphorylated STAT1 unrecognizable by importin- α 5, thus preventing its accumulation in the nucleus [40] and is for this reason employed later in this work, in order to control cytosolic STAT localization (**chapter 4.3.6**).

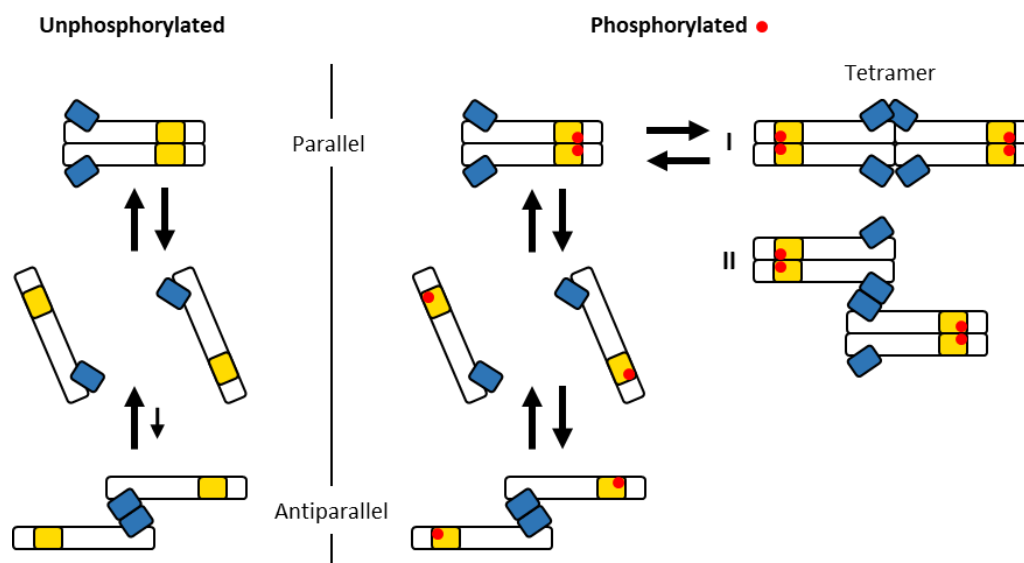


Figure 8: Model for STAT1 Oligomerization. Unphosphorylated (left) and tyrosine phosphorylated STAT1 (right). STAT1 homodimers exist in an antiparallel and parallel conformation. Upon phosphorylation, parallel dimers of STAT1 are able to form two possible tetramer conformations (I) and (II). N-terminal domains are shown in blue, SH2 domains are shown in yellow and phosphorylation of Tyr701 is shown as a red dot. Figure modified from [82].

Specifically, pSTAT1-pSTAT1 homodimerization is a well-described process for which even tetramerization has been reported [46, 80, 82]. Curiously, unstimulated STATs are also able to oligomerize, since STAT1-STAT1 homodimers [80, 82], as well as STAT1-STAT2 and STAT1-STAT3 heterodimers [98], and even the so-called “statosomes” have been reported to form in absence of phosphorylation [46]. These have been proposed to have important regulatory functions, considering that non-phosphorylated STATs are transcriptionally active towards sets of target genes distinct from those of phosphorylated STATs [46, 99]. Moreover, a variety of interactions between STATs and other effector proteins have been proposed for both phosphorylated and nonphosphorylated homo- and heterodimers, [23], which still remain to be tackled regarding affinity, kinetics and stoichiometry. Such a task not only requires an unbiased bioanalytical characterization, but also a methodology suitable for single-molecule analysis, which is crucial for any stoichiometric investigations of STATs.

1.3.3 USP18 and ISG15 regulate type I IFN receptor dimerization

Acting as a unique negative feedback regulator of type I IFN signaling, USP18 (ubiquitin specific protease 18, formerly UBP43) does not require its isopeptidase activity against di-ubiquitin-like ISG15 (interferon-stimulated gene 15) conjugates, but rather functions as a non-enzymatic inhibitor capable of destabilizing the ternary IFNAR complex at the plasma membrane [52, 53]. Canonically, expression of both USP18 and ISG15 is upregulated upon type I IFN stimulation, which in case of ISG15 is leading to a process called ISGylation, where ISG15 is conjugated via specific E1-, E2- and E3-protein ligases to a plethora of target proteins, akin to ubiquitination [54-56]. In turn, isopeptidase activity of USP18 is required for a process called deISGylation, cleaving ISG15 from conjugated proteins [100].

Peculiarly however, neither ISGylation [101] nor isopeptidase activity of USP18 [102] are required for regulation of type I IFN signaling. Instead, the negative feedback mechanism of type I IFN signaling relies on recruitment of USP18 to IFNAR2 via STAT2, which serves as a docking site and interacts with USP18 via the STAT2 coiled-coil (CC) and DNA binding (DB) domains [103]. Recruitment of USP18 then leads to a disruption of signaling, by shifting the equilibrium from the ternary toward the binary IFNAR complex at the plasma membrane.

Similar to the assays used for TpoR and JAK dimerization (**chapter 1.3.1**) [20], the role of USP18 in receptor dimerization was investigated by quantitative ligand-binding assays, and by single molecule co-tracking of IFNAR1 and IFNAR2 prior and upon stimulation via IFN subtypes and mutants (**Figure 9**) [19]. Not only did this reveal a mode of ligand-induced receptor dimerization, but also allowed probing of the negative feedback mechanism. Cells were observed after several hours of priming with IFN, i.e. stimulating the expression of interferon-stimulated genes, and then performing the dimerization analysis. It was found that ligand-induced IFNAR dimerization was quite similar for different IFN subtypes in naïve cells [19]. However, cells primed with IFN and cells transiently expressing USP18 showed that IFN α 2 was much less potent compared to IFN β or IFN α 2-YNS (**Figure 9b**), both featuring a ~50-fold increased affinity towards the low-affinity subunit IFNAR1 [50]. This desensitization towards the lower affinity subtype IFN α 2 demonstrates the α/β differential signaling, which in turn is caused by the negative feedback regulation of USP18 [19].

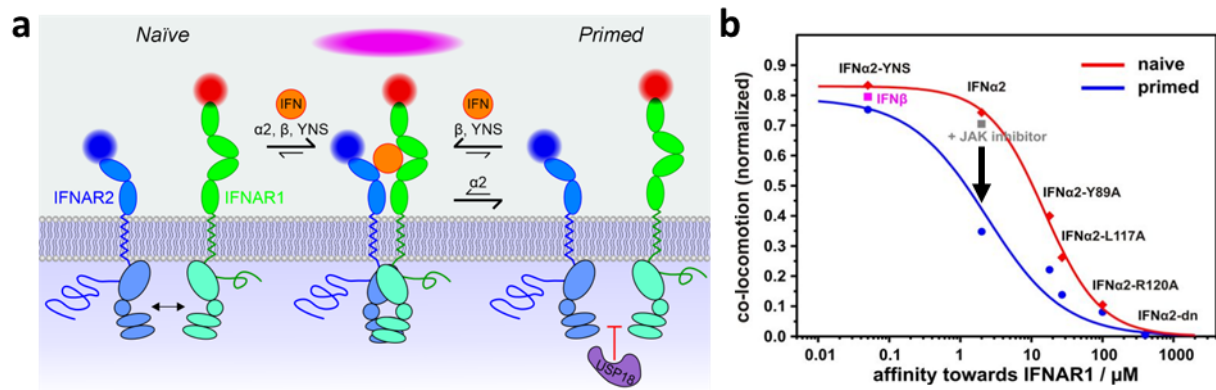


Figure 9: IFN-induced IFNAR dimerization and negative feedback regulation by USP18. (a) Schematic representing IFN induction in a naïve state (left), in a primed state in presence of negative feedback regulation by USP18 (right). Ternary complex formation (middle) results in an observable co-locomotion of receptors. In naïve cells, IFN α 2, IFN β and IFN α 2-YNS are capable to induce receptor dimerization. In primed cells, IFN β and IFN α 2-YNS are more capable to induce receptor dimerization than IFN α 2, favoring their \sim 50-fold increased affinity towards the lower-affinity subunit IFNAR1. (b) Co-locomotion analysis of surface receptors IFNAR1 and IFNAR2 determined IFNAR dimerization. The affinity-dimerization relationship is depicted for naïve and primed cells by a plot of the law of mass action. Figure (b) adapted from [19].

Most importantly, presence of ISG15 is critically required for long-term negative feedback regulation of USP18, as free cytosolic ISG15 is stabilizing USP18 by preventing SKP2-dependent ubiquitination. Due to decreased levels of USP18, amplification of IFN- α / β responses and autoinflammation is observed in cells lacking ISG15, making ISG15 another key negative regulator of type I IFN signaling, by directly influencing its long-term regulation [57].

Although IFN- α / β signaling and ISG induction are controlled by multiple negative regulators, protein-tyrosine-phosphatases (PTP), suppressors of cytokine signaling (SOCS) and protein inhibitors of activated STAT (PIAS) have been shown to be insufficient, whereas ISG15 is necessary to completely shut down IFN signaling and interferon-stimulated gene (ISG) expression [104]. When determining mRNA levels of ISGs in ISG15-deficient cells, it was found that high expression levels of transcripts (IFIT1, MX1) persisted up to 5 days after IFN priming, but returned to baseline after \sim 24 hours in control cells [104, 105]. Therefore, patients lacking ISG15 feature low USP18 levels, while showing higher steady-state levels of ISG transcripts in whole blood than controls [57, 106].

Peculiarly, it was observed that in humans, ISG15-deficiency and increased ISG expression leads a broad protection against viruses, but not in ISG15-deficient mice [104]. To further examine this species-specific interaction, we contributed by performing live-cell micropatterned pull-down experiments like those presented in this thesis,

quantifying the stability of the ISG15-USP18 complex in living cells. We found that the murine ISG15-USP18 complex was significantly less stable than the human counterpart. However, it was concluded that murine ISG15 does not act to sustain the level of murine USP18 and that the IFN response is regulated even in absence of murine ISG15, whereas humans crucially require ISG15 for USP18 stability and negative feedback regulation of the IFN response [104].

Considering the long-term functional effects of type I IFN, it was found that USP18- or ISG15-deficient patients all have high levels of ISGs in their peripheral blood mononuclear cells (PBMCs), which is common for all type I interferonopathies [107], yet only half of the ISG15-deficient patients show circulating type I IFN in their plasma [57]. As previously mentioned, ISG mRNA levels were significantly higher in USP18- or ISG15-deficient cells, persisting up to 5 days after IFN priming and IFN removal, whereas control cells returned to basal levels after ~24 hours [104]. Rather than a lack of down-regulation during the initial IFN exposure, RT-qPCR revealed active transcription of ISGs 60 hours after IFN removal in USP18- and ISG15-deficient cells, but not in control cells. Likewise, 36 hours after IFN removal, phosphorylated STATs (pSTATs) were detected and JAK activity was demonstrated. Even miniscule remainders of IFN in the supernatant were blocked by an anti-IFN antibody, but ISG transcription still persisted [105]. These findings indicated either a “cytokineless” signaling, or a cytokine presence within these cells, even several days after IFN removal. We contributed to this investigation by carrying out volumetric fluorescence imaging after treatment with fluorescently labeled IFN α 2 [105]. While IFNAR is known to undergo endocytosis [108], this was the first demonstration that IFN is retained endosomally after signaling cessation, in what we called “IFN silos”, explaining the paradox of the long-term cytokine signaling even after becoming undetectable [105].

Considering that free intracellular ISG15 was shown to stabilize USP18 levels [57], these findings demonstrate the delicate balance that is being exerted by USP18 and ISG15, as negative feedback without either of these proteins is not able to properly suppress long-term interferon signaling. Moreover, this illustrates the drastic effect of a dysregulated system of interacting proteins, stressing the importance of investigating and characterizing these PPIs of the type I IFN signaling pathway.

Regarding the structural basis of the USP18 and ISG15 interaction, all ISG15 residues involved in binding are localized within the C-terminal ubiquitin-like domain UL2 (**Figure 10**) [109]. In contrast, USP18 features two important regions involved in binding.

These are named the ISG15 binding box 1 (IBB1), comprised of A138, L142, S192 and H251 which are distributed across the thumb and palm domains, and the ISG15 binding box 2 (IBB2), comprised of Q259 and W262. The IBB2 is localized inside a region of amino acids 255-267 called blocking loop 1, which forms a small β -sheet upon binding of ISG15. Similarly, blocking loop 2 has been described in several members of the USP family and undergoes minor conformational changes upon ISG15 binding. The switching loop exhibits major conformational differences, folding from no secondary structure into a short α -helix and is known to influence the catalytic activity of USP18. Like ubiquitin, ISG15 features a C-terminal LRLRGG motif that binds the active site cleft of USP18 and is therefore crucial for deISGylation [109].

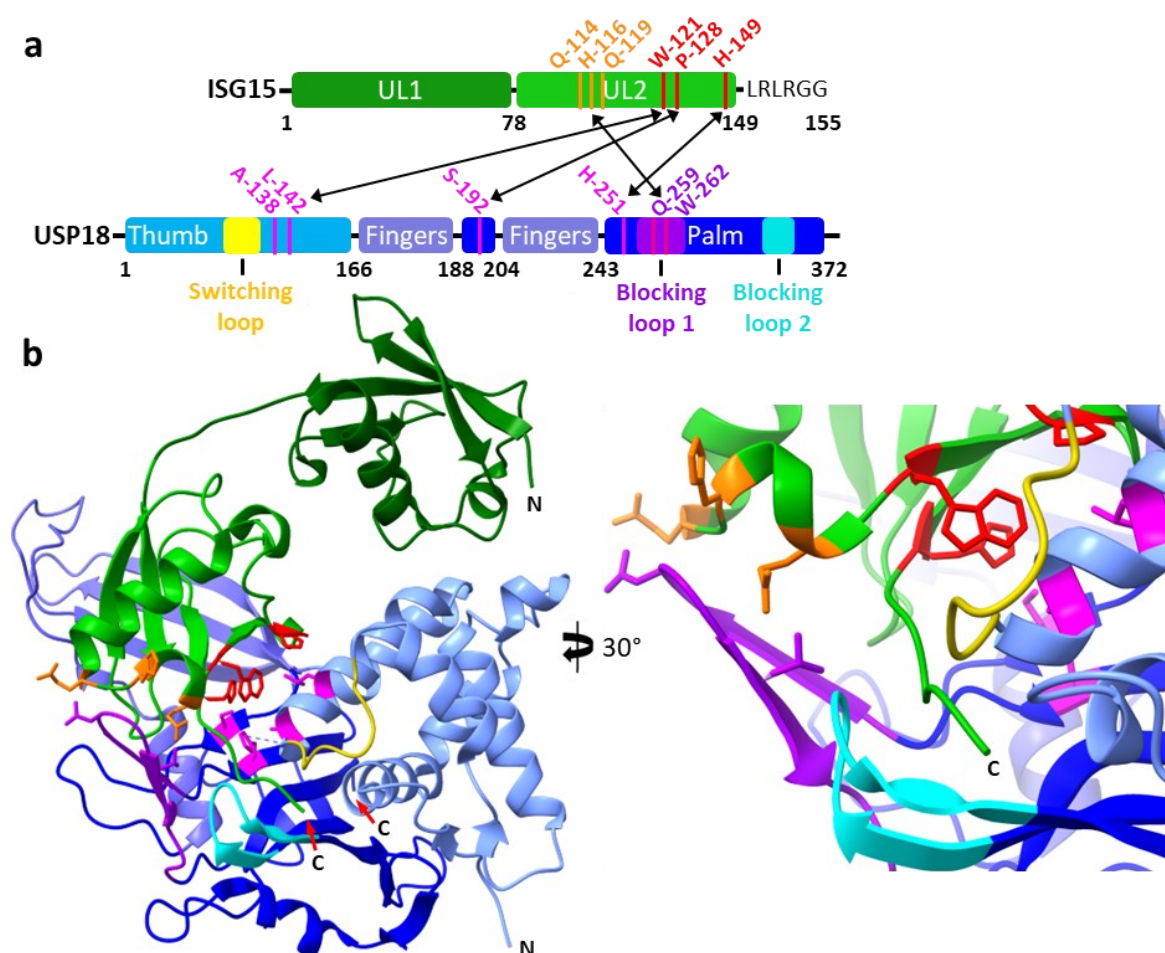


Figure 10: Structure of USP18 bound ISG15. (a) Schematic representation of ISG15 containing ubiquitin-like domains UL1 & UL2 (green), and USP18 featuring thumb, fingers and palm domains (blue). Amino acid residues of IBB1 (magenta) are localized across the thumb and palm domain of USP18 and interact with marked residues (red) within UL2 of ISG15. Amino acid residues of IBB2 (purple) are localized in blocking loop 1 and interact with marked residues (orange) of UL2. (b) Crystal structure of the USP18-ISG15 complex. PDB: 5CHV. Figure based on [109].

Additionally, USP18 features an unstructured N-terminal region from position 1-48, which remained unresolved in crystallography [109]. This N-terminal region is known to feature two additional translation initiation sites downstream of AUG1 [110]; The non-canonical start codon CUG16, which is regarded to play a role in expressing full-length USP18 due to a strong Kozak consensus sequence [111], and start codon AUG36, which leads to expression of an N-terminal truncated isoform, caused by a rather inefficient translation initiation of CUG16 [110]. Although both isoforms induce negative feedback of type I interferon signaling, the full-length isoform is mainly localized within the cytosol, whereas the N-terminal truncated isoform is equally distributed between cytosol and nucleus, and is thus responsible for performing most of USP18's deISGylation in the nucleus [110]. However, apart from the cellular localization of USP18 isoforms, this N-terminal domain remains to be tackled, regarding its influence on the USP18 interaction dynamics and negative feedback regulation.

Finally, given that the negative feedback regulation of USP18 relies not only on the recruitment to IFNAR2 via STAT2 as a docking site [103], but also on the interaction with free cytosolic ISG15 to stabilize USP18 by reducing degradation and enabling a prolonged negative feedback activity [57, 109], the question arises whether ISG15 is influencing the USP18-STAT2 interaction, which would imply a more direct involvement in the regulation of the negative feedback mechanism at the ternary receptor complex.

1.4 Methodologies for investigating protein-protein interactions

In order to probe and investigate protein-protein interactions (PPIs), many methodologies have been developed over time, growing ever more sophisticated compared to early methods such as SDS-page and western blotting [112]. As an overview, well-known screening and hybrid methods include (co-)immunoprecipitation (Co-IP) [113-115], pull-down assays [116], tandem affinity purification (TAP) [117, 118], and yeast-two hybrid (Y2H) [119, 120], or even split-ubiquitin [121]. These Screening methods have historically been followed up by methods used to validate specific interactions, for instance employing bimolecular fluorescence complementation (BiFC) [122, 123], proximity ligation assay (PLA) [124, 125], or Förster resonance energy transfer (FRET) [126]. For quantitative characterization of PPIs, fluorescence spectroscopy can be employed, utilizing the highly sophisticated methods of confocal FRET [127, 128], fluorescence (cross-)correlation spectroscopy (FCS, FCCS) [129], solid phase detection [130], as well as single-molecule fluorescence imaging [19].

As demonstrated by these different methods, a wide variety of strategies are employed depending on the specific biological question. It is however important to consider the strengths and potential shortcomings of the specific methods, as almost every biological method is somewhat artificial to some extent, which in turn can impose severe limitations. Of the aforementioned methodologies, some claim to investigate PPIs *in vivo*, but rely on purification or pull-down of proteins from whole cell lysates, realistically making them *in vitro* techniques. *In vitro* methods such as western blotting and Co-IP are a robust solution for quickly identifying binding partners, but may nevertheless lack in transfer and blotting efficiency. Moreover, harsh washing steps and prolonged purifications of protein lysates may potentially render highly transient PPIs non-detectable. In contrast, *in vivo* methods are advantageous for being carried out in living cells, enabling experiments under the biological context of a specific PPI, such as the native membrane environment. Depending on the application however, some *in vivo* methods require relatively high protein expression levels, introducing a potential bias caused by artificially altered rate and affinity constants of PPIs, which are naturally fine-tuned for their respective physiological expression levels. By design, some *in vivo* and *in vitro* methods are artificial to such an extent, that they are described as *in cellulo* or *in situ*, instead. It is therefore crucial to investigate PPIs not only within their biological context, but also as close as possible to their physiological conditions.

Exemplifying the importance of these critical conditions is the controversy covered in previous chapters, over the mechanism of cytokine receptor assembly, as correlation of structure, mechanism and function remained enigmatic for a long time. Already in 1991, ligand-induced receptor dimerization was proposed as a model to trigger cytokine signal activation [131]. However, later models concluded ligand-induced conformational changes of preformed receptor dimers as the activation mechanism [75, 132, 133]. Supported with considerable structural and biochemical studies, the growth hormone receptor was established as the paradigm of pre-dimerized cytokine receptors [132, 134-136]. In fact, several studies supported dimerization independent activation of both class I and class II cytokine receptors [137-141], leading to the suggestion of receptor predimerization as the general concept for the whole receptor family [75, 132]. Not only biochemical data, but even confocal FRET analysis of the type I IFN receptor concluded ligand-independent pre-dimerization of receptor subunits, disregarding the artificially high expression levels required to perform such an analysis [128].

Most importantly however, this model could clearly be refuted by live-cell single-molecule tracking experiments of the prototypical type I cytokine receptors TpoR, EpoR and GHR (see **chapter 1.3.1**)[20], as well as of the class II cytokine receptor IFNAR (see **chapter 1.3.3**) [19]. This discrepancy to previous biochemical studies and even confocal FRET studies can be explained primarily by the fact that live-cell single-molecule tracking experiments could not only be carried out in the biological context of these receptors, but also closer to their physiological conditions, such as receptor expression levels. Thus it can clearly be summarized that live-cell single-molecule methods are suitable methods for investigating receptor dimerization. Similarly, suitable methods are required to investigate cytosolic interactions of cytokine signaling pathways, in order to characterize the interaction dynamics and complex stoichiometry of the cytosolic PPIs involved in type I IFN signaling, which is the main topic of this thesis.

To summarize, traditional pull-down methods are most suitable for qualitatively identifying interaction partners, but not for quantifying such interactions. In contrast, cell micropatterning techniques are emerging and are probably the desired techniques to study living cells, post-translational modifications (PTMs), the plasma membrane, or multiple interaction partners in their biological context. For these reasons, in this thesis I have developed several live-cell and pull-down micropatterning assays that offer a simplified multilayer biocompatible surface procedure and a generalized protein targeting to enable a quantitative investigation of cytosolic protein-protein interactions.

2 Objective

Cytokines are key factors of cellular signaling that regulate hematopoiesis as well as homeostasis and activation of diverse immune functions. The JAK-STAT signaling pathway is the hallmark of the class I and II cytokine receptor families, characterized by signaling plasticity and pleiotropy. Subtle and precisely tuned protein-protein interactions (PPI) play an important role in defining signal activation and signaling specificity, and their dysregulations can lead to catastrophic repercussions, such as cancerous cell growth, pathogen susceptibility, or autoimmune diseases. Some of these features are prominently represented by type I interferon (IFN) signaling, initiated by a heterodimeric class II cytokine receptor with its unique negative feedback regulators ISG15 and USP18. While interactions of the receptor subunits in the plasma membrane have been well characterized, the exact molecular mechanisms of cytosolic PPIs remained elusive, requiring quantitative characterization of interaction dynamics and stoichiometry. Analysis by classical biochemical and biophysical methodologies is not suitable to quantify these transient PPIs involving multiple, partially intrinsically disordered proteins.

The objective of this thesis was to develop micropatterned pull-down assays for investigating interaction dynamics and stoichiometry of PPIs. The pull-down is directed against the popular green fluorescent protein (GFP), while relying on simple micropatterned surface architectures, tremendously simplifying the workflow for qualitative and quantitative PPI analysis. To this end, a cell- and protein-compatible surface functionalization was established based on microcontact printing of polymers, while utilizing an anti-GFP nanobody for specific and efficient pull-down of GFP-tagged proteins. These techniques allowed capturing of cytosolic protein complexes inside living cells, enabling quantitative analysis of even transient PPIs via total internal fluorescence microscopy (TIRFM). Additionally, *in situ* single cell pull-down (SiCPull) was established to quickly transfer protein complexes during cell lysis from the cytosol to NB surface micropatterns, enabling to investigate interaction dynamics of transient protein complexes, and even their stoichiometry on the single molecule level. Using effector and regulator interaction involved in type I IFN signaling, I demonstrate the capabilities of these approaches for quantitative interaction analyses, thus providing a versatile toolbox for scrutinizing cytosolic protein complexes in a cellular context.

2.1 Strategies

2.1.1 GFP protein tags as generic pull-down targets

Since the discovery of genetically encoded fluorescent proteins, prominent protein tags like GFP and its derivatives have been employed as fusions with virtually any protein of interest for visualization via fluorescence microscopy [142]. Considering the abundance and ease of creating these fusion proteins, it stands to reason to target the commonly used GFP-tag with an efficiently binding protein, serving as a generic assay to readily enable pull-down of any GFP-tagged target protein, while significantly reducing the need for sophisticated target-specific optimizations.

2.1.2 Antibody-related protein binders

All living organisms are continuously exposed to potentially harmful substances. However, vertebrates have evolved an additional line of defense, the adaptive immune system. Upon immunization of a host animal, B cells are undergoing affinity maturation and are expressing antibodies for the sole purpose of binding the invasive antigen, creating extremely efficient protein binders suitable for pull-down assays. Although generally featuring a high affinity and being deployed against many different targets in biological and medical applications, antibodies such as Immunoglobulin G (IgG) are limited in their applications due to their large size (IgG ~150 kDa), complex oligochain structure and bivalent binding (**Figure 11a**). To this end, smaller and monovalent antibody-related binders have been developed, offering efficient binding and less complexity, while differing in stability and production capabilities [143]. For example, both the antigen-binding fragment (Fab) and the single chain variable fragment (scFv) are simpler antigen-binding proteins consisting of one constant and one variable domain (Fab), or only one variable domain (scFv) of each of the heavy and light chain (**Figure 11a**). While the Fab is obtained from papain digestion and the scFv from artificial cloning, both are antibody-derived and their features can therefore be fine-tuned when employing screening methods like phage, yeast and ribosome display, as well as enzyme-linked immunosorbent assays (ELISA) [143].

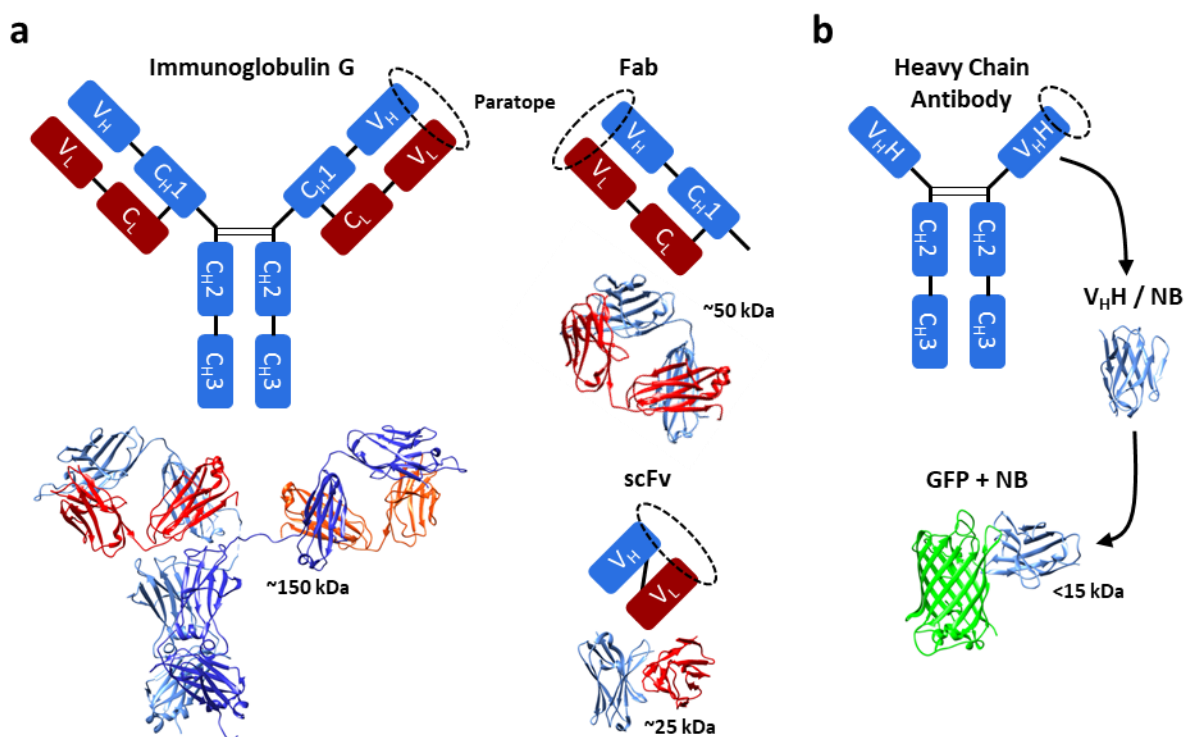


Figure 11 Antibody-related protein binders. (a) Scheme and crystal structure of an immunoglobulin G (IgG) antibody (IgG PDB: 1HZH) and derived proteins. Paratope marked as dashed line. Antigen binding fragment (Fab) can be obtained via papain digestion and single chain variable fragment (scFv) can be obtained from artificial fusion of heavy and light chain variable fragments. (b) Scheme of a cameloid heavy chain antibody lacking in light chains. Variable domains (V_{HH}) can be isolated to obtain a Nanobody. Crystal structure of the anti-GFP enhancer NB binding GFP (PDB: 3K1K). All structures are of similar scale.

However, the paratope of these antibody-related proteins consists of two variable domains, both being required for antigen binding and moreover, their intra- and interdomain disulfide bonds and hydrophobic domain interfaces are often harmful for colloidal stability [144, 145]. Fortunately, heavy chain antibodies are found in cameloids, which feature a simpler structure by lacking the light chains, while also undergoing affinity maturation following immunization of a host animal (**Figure 11b**) [146, 147]. Most importantly, their paratope consists of only a single variable domain (V_{HH}) which can therefore be genetically isolated as a single-domain antibody, called nanobody (NB). Since a single gene is encoding a nanobody, they can be utilized for genetic engineering and fusion proteins, offering a wide range of applications. Although cysteine bonds are still present, NBs offer greater colloidal stability than Fab or scFv fragments [147] and can likewise be screened to further improve their features. As such, GFP-binding NBs have been screened to modulate the conformation and spectral properties of GFP, yielding an anti-GFP NB ‘enhancer’ which is able to enhance GFP fluorescence fourfold, while also binding GFP with a high affinity [148]. Thus, the anti-GFP NB enhancer was used in this work as the main pull-down strategy of GFP-fused proteins.

2.1.3 Micropatterned surface architectures

Soft lithography offers a variety of patterning techniques based on printing, molding and embossing of organic and polymeric materials, called soft matter, while employing elastomeric stamps made of polymers such as poly-dimethylsiloxane (PDMS) [149, 150]. Production of elastomeric stamps simply requires a commercially available master, which is generated via photolithography to feature the desired microstructures for molding of PDMS stamps. Microcontact printing (μ CP) employs PDMS stamps to generate well-defined and controllable surface micropatterns suitable for pull-down assays, while being compatible with a variety of materials like proteins, polymers and metal surfaces (**Figure 12a**) [151].

However, one major challenge of surface-based pull-down assays is direct protein adsorption onto the substrate, which is generally leading to denaturation and loss of protein activity [150, 152]. This in turn renders directly micropatterned protein binders inactive and introduces non-specific binding, biasing fluorescence microscopy readouts. Overcoming this challenge, a biocompatible passivation layer is typically employed to prevent non-specific binding, which in turn requires a secondary functionalization to bind the target protein. For instance, such a surface passivation is achieved by employing bovine serum albumin (BSA) to prevent non-specific binding of proteins [149]. Other strategies rely on an initial layer to form complexes with the desired proteins, employing protein A to bind IgG antibodies, Ni-(nitriloacetic acid) as a nickel chelator to bind histidine tags, or utilizing the interaction of the co-factor biotin with avidin or streptavidin [150]. However, these systems may suffer from cross-reactivity with endogenous biological molecules.

In contrast, protein tagging systems such as the genetically encoded HaloTag or SNAPTag are suicide enzymes, which irreversibly bind to their respective ligand and can be utilized for bio-orthogonal binding of dye conjugates or for protein immobilization [153-156]. The HaloTag is a commercially available mutant of the bacterial haloalkane dehalogenase DhaA from *Rhodococcus rhodocrous*, which was designed for rapid, highly specific and irreversible binding by recognizing halogenated alkanes and remaining in the intermediate state of the enzymatic reaction, forming a covalent conjugate with its synthetic HaloTag ligand (HTL) (**Figure 12c**). This makes the HaloTag an ideal strategy for surface functionalization, especially in combination with a biocompatible layer to prevent non-specific binding.

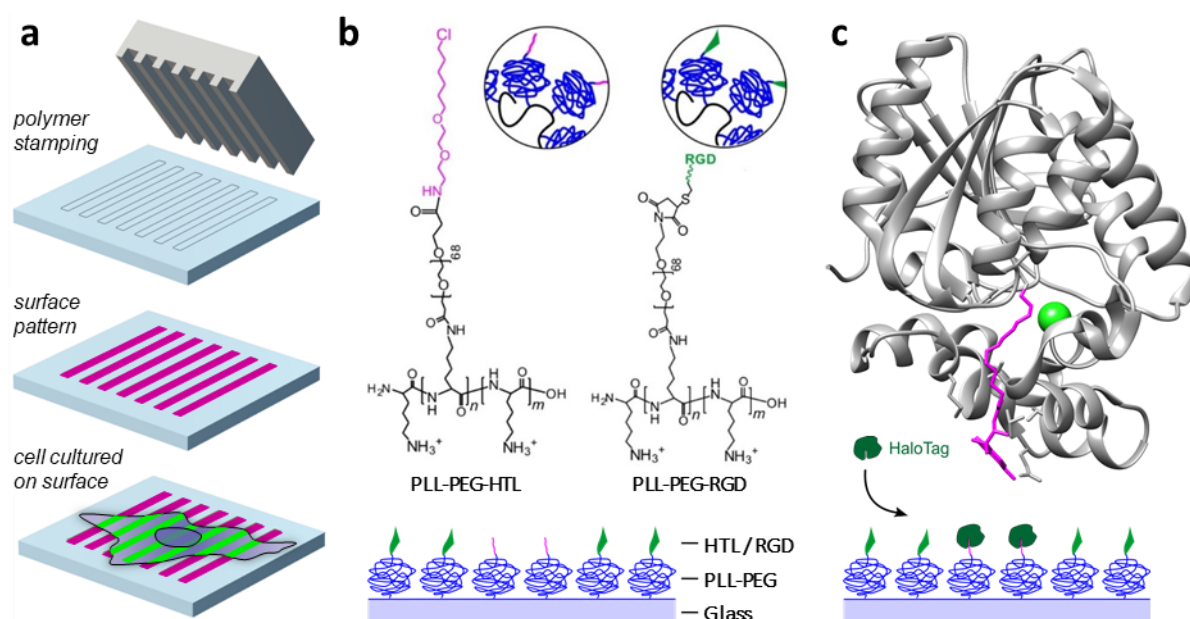


Figure 12: Micropatterned surface architecture. (a) Microcontact printing. A stamp is loaded with PLL-PEG-HTL and pressed onto a surface to generate a micropattern. Cells are grown on the micropatterned surface, with HaloTag-fused proteins interacting with the micropattern. Image kindly provided by Christoph Drees. (b) Polymers and scheme of the resulting binary micropattern. (c) Crystal structure of HaloTag (grey) and HTL (magenta) (PDB: 5VNP). Scheme of HaloTag binding the HTL micropattern.

As an alternative approach to protein surface passivation, self-assembled monolayers (SAMs) are often utilized for surface fabrication. These highly versatile hydrocarbon-based structures control the physicochemical properties of the surface by anchoring to the substrate and closely interacting along their chains, forming a polymer-brush on the surface [150]. For instance, SAMs of poly-L-lysine grafted poly(ethylene glycol) (PLL-PEG) are rapidly adhering to negatively charged glass substrates via the positively charged PLL, whereas PEG chains create a hydrophilic polymer-brush, preventing non-specific protein adsorption and cell adhesion, thus requiring a cellular adhesion motif. [150, 157] (**Figure 12b**). Furthermore, SAMs can be terminated with a variety of functional groups, like biotin or HTL, in turn enabling protein immobilization and cellular adhesion on a passivated surface, as were described previously [158-160].

Among various cell surface adhesion receptors including integrins, syndecans, cadherins and other proteoglycans, cell attachment to substrates is mostly mediated by the prominent integrin family of transmembrane heterodimeric receptors. Integrins are involved in the dynamic formation of contacts between cells and the extracellular matrix (ECM), by binding specific sequence motifs found in proteins such as fibronectin, collagen and other ECM proteins [161, 162]. A prominent example is the arginine-glycine-aspartic acid (RGD) tripeptide, which is specifically recognized by integrins via an RGD tripeptide active site [162] and is therefore utilized to promote cell adhesion [163, 164].

2.1.4 Generic nanobody live cell micropatterning assay

Laying the foundation of this work, μ CP was utilized to generate micropatterned surface architectures, employing PLL-PEG functionalized with HTL and RGD to generate cell- and protein-compatible surface micropatterns, to enable highly efficient and specific intracellular pull-down assays [158]. Aiming to implement a generically applicable live cell micropatterning approach, a ‘NB construct’ was designed, fusing the HaloTag with a blue fluorescent protein (mTagBFP), a transmembrane domain (TMD) and the anti-GFP nanobody enhancer (NB), in order to respectively enable surface immobilization, fluorescence visualization and intracellular capturing (**Figure 13a**). Upon cellular expression, the NB construct immobilizes into PLL-PEG-HTL micropatterns through the HaloTag. Intracellularly, the NB specifically and efficiently captures GFP-fused “bait” proteins into the micropattern, in turn co-capturing interacting “prey” proteins depending on their interaction dynamic and the prevalent equilibrium.

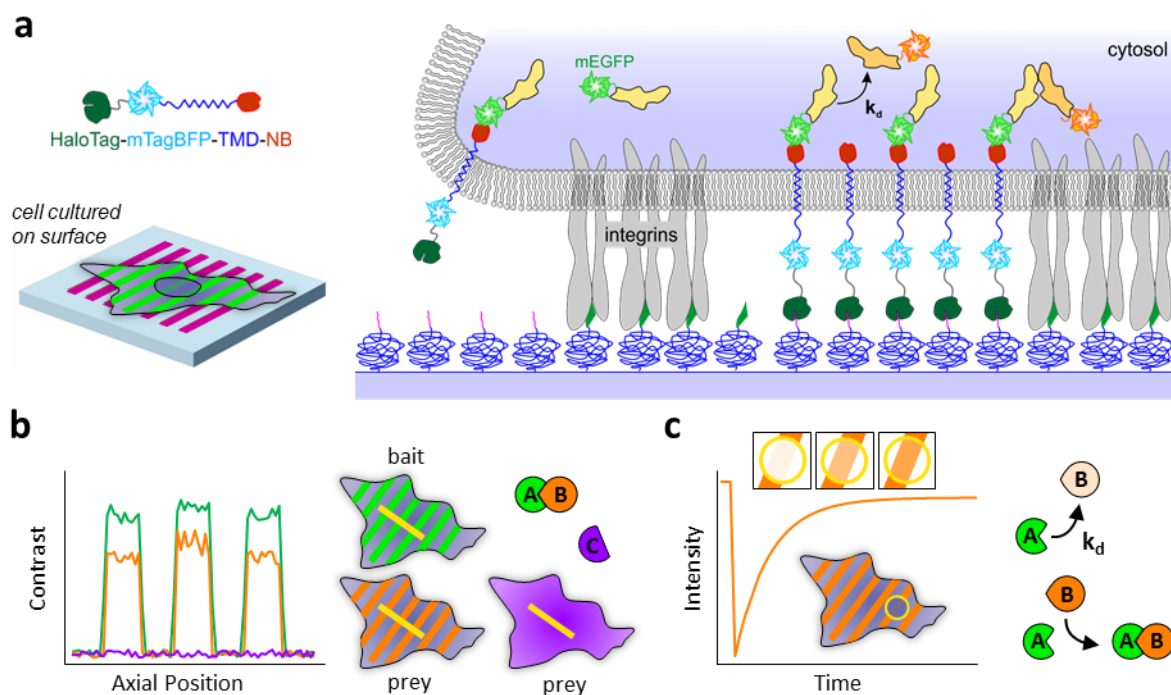


Figure 13: Nanobody live cell micropatterning. (a) Schematic representation of a micropatterned cell and the surface architecture. The ‘NB construct’ is a fusion of HaloTag, mTagBFP, transmembrane domain (TMD) and nanobody (NB). It enables surface immobilization into HTL micropatterns and intracellular pull-down of GFP-tagged bait-proteins. Prey-proteins are co-captured according to their dissociation dynamics (k_d). (b) Contrast Analysis probing protein interaction and competition inside bait-protein enriched micropatterns. Three fluorescent channels representing protein A, B and C are analyzed for normalized fluorescence intensity inside the region of interest (ROI, yellow bar). (c) FRAP Analysis probing the interaction kinetics between bait protein ‘A’ and prey protein ‘B’, by photobleaching a circular area (yellow circle) in the orange fluorescence channel and observing the fluorescence recovery of protein B over time.

Capturing and co-localization is then visualized via total internal reflection fluorescence microscopy (TIRFM) [165], appearing as an enrichment of fluorescent proteins inside the NB micropatterns, which can be evaluated as the fluorescence contrast (**Figure 13b**). However, as protein interactions and occurring contrast levels are not only controlled by affinity but also by concentration of each reactant, cellular expression levels are a major concern for intracellular methods. Moreover, full localization of the NBs and bait proteins within the micropattern is especially crucial to confine the co-localization of prey proteins to the micropattern. Protein overexpression should therefore be avoided, as high NB and bait protein concentrations may potentially exceed the capacity of binding sites in the micropattern, leading to background capturing and localization outside of the micropattern, biasing the analysis by decreasing the apparent fluorescence contrast. Although being a rather qualitative method, live cell micropatterning is further enhanced by performing bait specific fluorescence contrast analysis, correcting for the bait contrast of each evaluated cell (**chapter 3.4.2**), yielding semi-quantitative results indicating the relative protein interaction dynamic (**Figure 13b**). Moreover, by simply combining live cell micropatterning with photomanipulative assays like FRAP [158, 159], quantitative analysis of interaction kinetics of various PPIs can be performed (see **chapter 3.4.3**) (**Figure 13c**). This method thus readily enables pull-down and interaction analysis of a plethora of commonly available GFP-tagged proteins, avoiding the need for target-specific bait proteins, while simply requiring the plasmid of the 'NB construct' and the basic materials to generate the micropatterned surface architecture.

Moreover, this method has several advantages over micropatterning methods that employ antibodies directly print onto glass surfaces [166]. While a surface antibody micropattern can only immobilize intracellular proteins of interest by first binding transmembrane interaction partners such as receptors, this method enables direct capturing of any GFP-fused cytosolic protein in intracellular membrane micropatterns (**Figure 13a**). Additionally, this method enables incubation with labeled molecules, allowing them to interact with the cell without causing any fluorescent background on the surface, as the PLL-PEG passivation prevents non-specific binding. And finally, the PLL-PEG-HTL surface is extremely versatile, as HaloTag-fused receptors, or purified HaloTag-fused proteins can also directly bind to the HTL micropattern, as seen for the next application. The generic nanobody live cell micropatterning is therefore a powerful and robust tool to investigate protein-protein interactions in the cellular context.

2.1.5 *In situ* single cell pull-down (SiCPull) assay

Whereas in-cell methods such as live cell micropatterning are challenging with regards to controlling protein expression and concentrations *in vivo*, protein production or purification remains very demanding for *in vitro* methods. Aiming to overcome these fundamental challenges, protein production inside living cells was closely linked with a highly sensitive and robust surface-based protein interaction analysis. To this end, the *in situ* single cell pull-down (SiCPull) was developed as a novel method for specific and efficient pull-down of protein complexes from individual cells, based on the micropatterned surface architectures generated via μ CP of PLL-PEG (**Figure 14**).

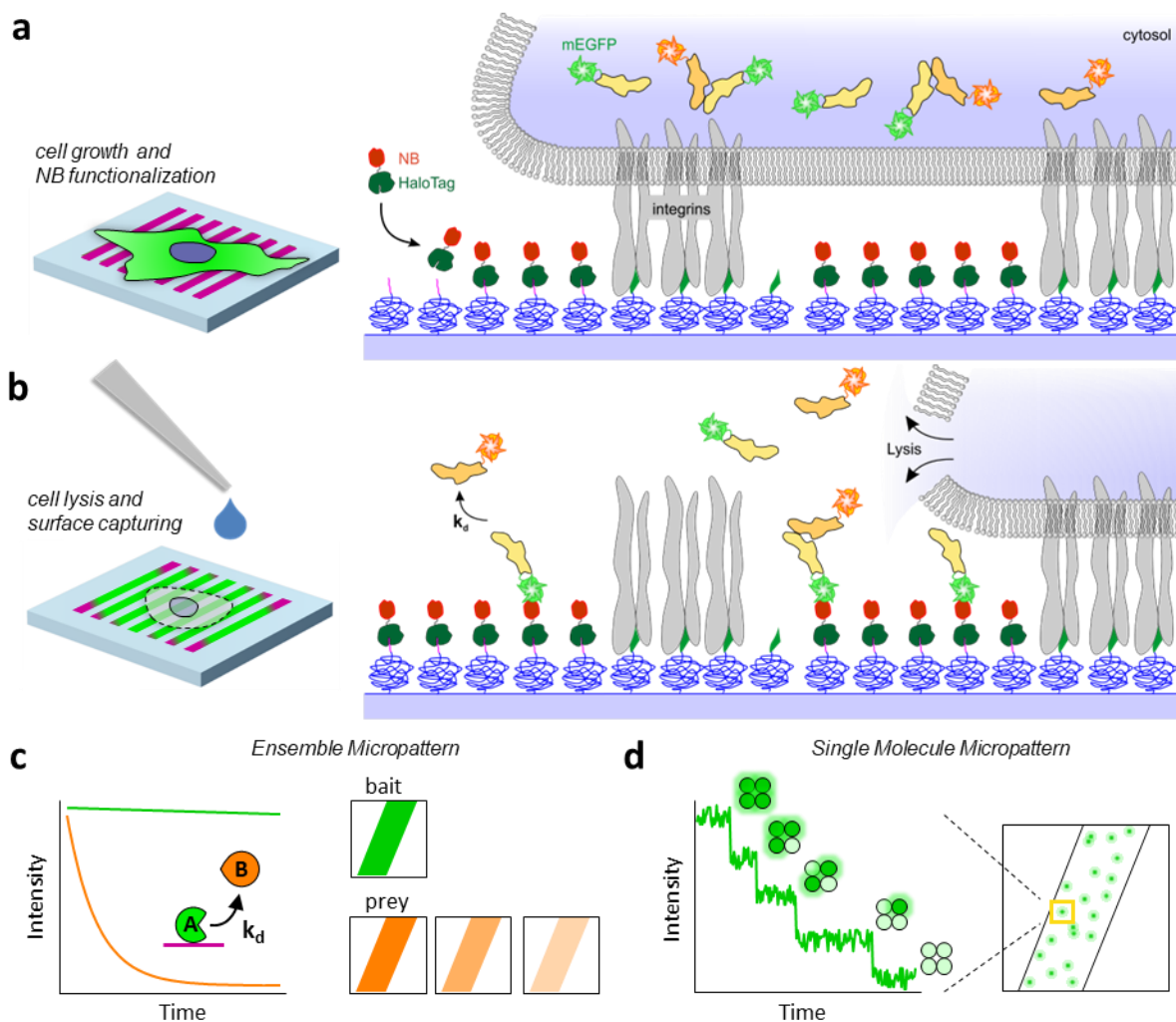


Figure 14: Single cell pull-down (SiCPull). (a) Schematic representation of a cell growing on a micropatterned surface and of the surface architecture. The cell is expressing GFP-tagged bait proteins and prey proteins. Prior to the experiment, the surface is functionalized with the HaloTag-NB fusion protein, by binding HTL on the surface. (b) Addition of a lysis buffer initiates cell lysis and the release of cytosolic proteins from the living cell. GFP-tagged proteins are captured *in situ* into the NB micropattern within close proximity to the host cell, co-capturing interacting prey proteins. The cell undergoes visible shrinkage following the cytosolic release. (c) Dissociation analysis: Interaction kinetics between bait and prey proteins are analyzed by observing the dissociation of co-captured prey from the micropattern, leading to a decrease of the fluorescence signal over time. (d) Photobleaching analysis determines the stoichiometry of distinct captured complexes by observing photobleaching steps.

As previously published, a purified fusion of the HaloTag with the anti-GFP NB enhancer (HaloTag-NB) is employed for generating a functionalized anti-GFP surface on a PLL-PEG-HTL micropattern [160] (**Figure 14a**). Cells cultured on these surfaces are lysed by mild detergents, leading to instantaneous *in situ* capturing of GFP-tagged bait proteins, while co-capturing any interacting prey proteins (**Figure 14b**). SiCPull thus exploits cellular protein expression of mammalian cells while avoiding demanding protein purification from whole-cell lysates, as the entirety of the assay is performed on-chip.

Importantly, protein concentrations exceeding the micropattern binding capacity are swiftly diluted in the sample volume, leading to a distinct single-cell capturing within close proximity of the host cell (**Figure 14b, left**), effectively eliminating typical cellular background signals caused by overexpression of fluorescent proteins. Complex interactions are then readily characterized by monitoring the dissociation of co-captured prey proteins from the micropattern via TIRFM, as plotting of the fluorescence signal and exponentially fitting of the decay over time yield the dissociation rate constant and characteristic lifetime of an interaction (**Figure 14c**)[160]. Moreover, highly sensitive and versatile detection of proteins down to the single molecule level enables stoichiometric analysis of individual protein complexes captured from single cells (**Figure 14d**). Due to the diffraction limitation defined by Abbe's law, micropatterns with a sufficiently low surface density of binding sites need to be employed, avoiding biased analysis caused by overlapping fluorescence signals. After acquiring single molecule bleaching movies, the quantitative analysis is aided by sophisticated software yielding robust and reproducible stoichiometry data for thousands of individual molecules, while reliably correcting for inhomogeneous sample illumination (**see chapter 3.4.6**).

In comparison, this pull-down assay features significant improvements compared to similar single molecule pull-down methods which employ randomly distributed antibodies on PEGylated surfaces and require secondary antibodies for labeling [167]. Most importantly, micropatterns serve as an internal control for surface passivation and binding specificity, as baseline background fluorescence and non-specific binding events can easily be determined for each experiment. Also, employing the anti-GFP Nanobody for pull-down renders labeling obsolete, since only the GFP-fused target proteins are visible in the corresponding fluorescence channel. This in turn overcomes cross-reactivity between primary and secondary antibodies, as well as non-specific antibody binding of random proteins, which requires a plethora of control experiments in pull-down assays.

2.1.6 Bimolecular fluorescence complementation in pull-down assays

Bimolecular fluorescence complementation (BiFC) is an assay commonly used to visualize protein interactions in living cells. In principle, two non-fluorescent fragments of a fluorescent protein are fused with two distinct proteins of interest, which upon interaction facilitate assembly and folding of a bimolecular fluorescent complex that can be visualized via fluorescence microscopy [122, 123]. To this end, N- and C-terminal split domains of GFP and its derivatives are commonly generated by truncating either at position 155 or 173 of the peptide chain, offering a high complementation efficiency, as well as very low fluorescence of non-interacting split domains [168]. Strikingly, these truncations enable complementation between fragments of fluorescent proteins with different spectral characteristics (BFP, CFP, GFP, YFP) and even between fragments truncated at position 155 and 173, yielding complexes with slightly altered spectral properties and enabling multicolor BiFC in a single cell [168]. Moreover, newer fluorescent fragments obtained from fluorescent proteins such as Venus and Cerulean have also been introduced, overcoming the higher temperature sensitivity of YFP while featuring a 13-fold increased BiFC efficiency over original YFP fragments [169], demonstrating generation of fragments of many autofluorescent proteins. Reminiscent of yeast two-hybrid, split-GFP fragments can be easily implemented into the nanobody-based pull-down assays presented in this work, offering selective pull-down into micropatterns and visualization of specific protein complexes upon complementation (**Figure 15**).

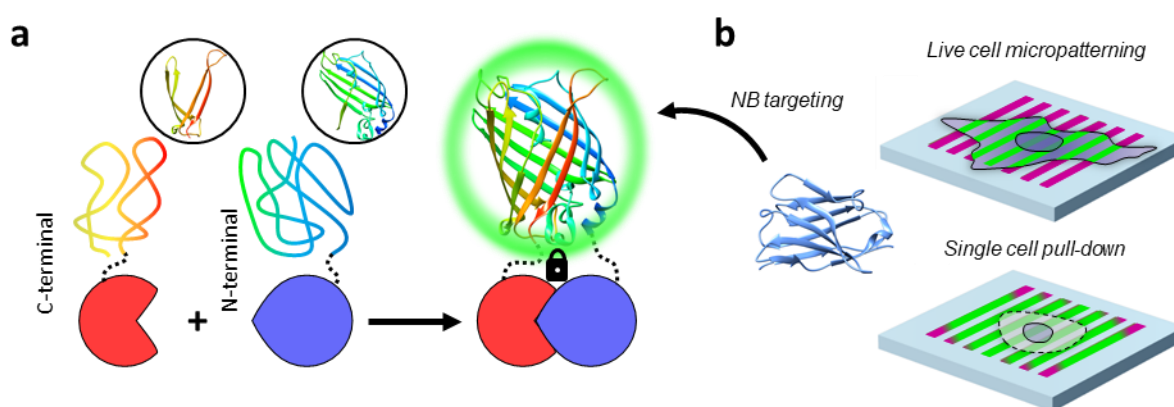


Figure 15: Two-hybrid NB pull-down assays. (a) C-terminal fragment 155-238 and N-terminal fragment 1-154 of GFP are fused with proteins of interest, which upon interaction facilitate complementation and folding of the split GFP, preventing the interaction from dissociating. Complementation yields chromophore maturation and a fluorescence signal. (b) Complemented GFP can be targeted by the anti-GFP Nanobody ‘enhancer’, enabling pull-down of defined complexes in NB pull-down assays. Structure shown: PDB 3k1k.

Moreover, the individual non-interacting split-GFP domains not only remain non-fluorescent, but also unfolded and thus unrecognizable by the paratope of the employed anti-GFP NB, ensuring an unbiased and almost background-free detection. This way, even artificial formation of non-native complexes caused by cellular overexpression can be eliminated, leaving overexpressed and endogenous proteins invisible and enabling the selective investigation of only the complexed proteins of interest [122]. Over time, even transient protein interactions are accumulated in complexes, being locked via the irreversible protein complementation of the split fragments, enabling characterization of highly transient complexes following their enrichment in NB micropatterns. Additionally, the fluorescence signal of the bimolecular complex serves as an important internal control for proper interaction between the generated fusion-proteins, as certain fusion protein combinations may run the risk of failing to undergo complementation [168]. In conclusion, incorporating BiFC into the NB live cell micropatterning and SiCPull assays would require minimal effort, as both strategies are centered around the use of the anti-GFP NB, while readily enabling a specific two-hybrid pull-down of protein complexes of interest, disregarding any non-interacting proteins. The possibilities of such two-hybrid pull-down assays was therefore additionally explored in this thesis, by conducting initial proof-of-concept experiments for validation purposes.

3 Materials and Methods

For this work, basic compounds including medium, supplements and antibiotics for cell culture (Carl Roth, PAN Biotech, Biochrom, Biomol), as well as enzymes and solutions for molecular biology (New England Biolabs), chemicals and polymers for synthesis (Sigma Aldrich, Rapp Polymere, SurfaceSolutions GmbH) and imprint master and chemicals for PDMS stamp manufacturing (NB Technologies, Dow Chemicals), were all obtained from corresponding suppliers and used according to standard protocols or their instructions.

3.1 Molecular Biology

3.1.1 Mammalian cell culture and transfection

HeLa cells were cultivated at 37°C and 5% CO₂ in minimum essential medium (MEM) supplemented with 10% fetal calf serum, 1% non-essential amino acids and 1% HEPES buffer. HeLa cells were seeded on 60 mm petri dishes, in an appropriate amount to yield approximately 50% confluence and were used for transfection, following standard calcium phosphate precipitation protocols [170]. Cells were handled as previously described [171], subsequently seeded on polymer functionalized surfaces generated via microcontact printing.

3.1.2 Plasmid generation

All constructs used for transfection were cloned into the pSEMS-26m (Covalys) plasmid vector, with genes inside the multiple cloning site being controlled by the CMV promoter, to allow high expression in mammalian cells. Genes used in constructs include the HaloTag (Promega) [156] and a fast labeling variant of the SNAP-tag (fSNAP) [172] for specific protein binding and labeling and an artificial transmembrane domain (TMD) comprised of the sequence ASALAALAALAALAALAALAKSSRL (ALA7) [173]. As fluorescent proteins, monomeric blue fluorescent protein (mTagBFP)[174], monomeric enhanced green fluorescent protein (mEGFP) obtained by A206K mutation of EGFP [175], monomeric red fluorescent protein (mCherry) [176] and red fluorescent protein (TagRFpT) [177] were used. The anti-GFP nanobody (NB) named “GFP-enhancer” was cloned for specific capturing of mEGFP [148]. For specific capturing of interacting protein complexes, bimolecular fluorescence complementation (BiFC) was adopted [122], cloning both the N-terminal (1-155, NmEGFP) and C-terminal (156-239, CmEGFP) domains of mEGFP to proteins of interest, allowing capturing of complemented mEGFP upon co-expression and interaction.

3.1.3 Protein purification

Both HaloTag-mEGFP and mEGFP were cloned into pET28b (Novagen), which carries an N-terminal His₆-tag, and were expressed in *E. coli* (BL21 strain) at 37°C, followed by purification via immobilized metal ion affinity chromatography (IMAC) and size exclusion chromatography (SEC) as previously described [178].

HaloTag-anti GFP nanobody fusion protein (HaloTag-NB) was generated by fusion of the NB, His₁₀-tag, ybbR-tag [179] and HaloTag sequences and cloning into the pBAC insect vector (Novagen) as previously described [159]. Linearized viral DNA (BD Biosciences) and expression vector were co-transfected into Sf9 cells and subsequent protein expression and purification by IMAC and SEC were carried out as previously described [180]. Purified mEGFP, HaloTag-mEGFP and HaloTag-NB were kindly provided by Hella Kenneweg (University of Osnabrück).

3.2 Synthesis of PLL-PEG derivatives

3.2.1 HaloTag ligand-functionalized poly-L-lysine-graft-(polyethylene glycol) copolymer (PLL-g-PEG-HTL)

Synthesis of PLL-PEG-HTL was altered since being previously reported [159]. Here, 13.5 mg bis-(2-(3-carboxy-1-oxopropyl)-amino)-ethyl polyethylene glycol (COOH-PEG-COOH, Mw: 3000 Da, Sigma-Aldrich) and 5 mg of N-(3-Dimethylaminopropyl)-N'-ethylcarbodiimide hydrochloride (EDC, Mw: 192 g/mol, Sigma-Aldrich) were solved in 50 µl HEPES buffer (100 mM HEPES, pH 7.5). Next, 1.1 mg of amino group-functionalized HaloTag ligand (HTL-NH₂, Mw: 223 g/mol, synthesized as previously reported [178]), was solved in 40 µl N,N-Dimethylformamid (DMF) and was added to the solution. The reaction solution was stirred overnight at room temperature. Afterwards, the mixture was added to a solution of 4 mg poly-L-lysine hydrobromide (Mw: 15.000-30.000 g/mol, Sigma-Aldrich) in 50 µl HEPES buffer (100 mM HEPES, pH 7.5). A freshly prepared EDC solution with 5 mg of EDC in 40 µl of the same buffer was added to this solution. After stirring overnight at room temperature, the mixture solution was dialyzed against MilliQ water for 24 hours. The sample was lyophilized, resulting in a white powder.

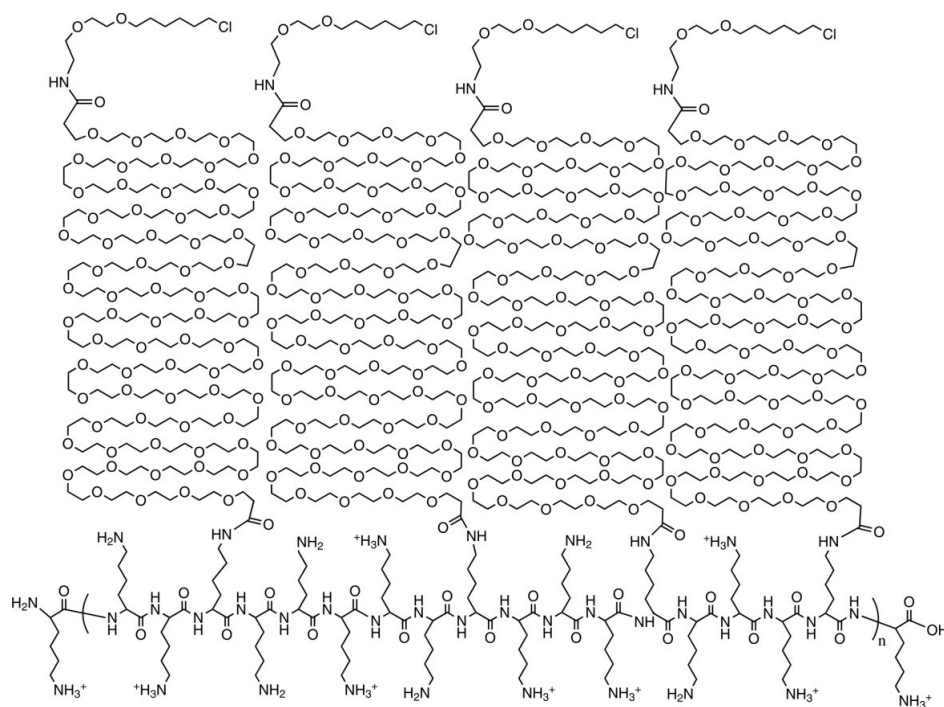


Figure 16: Molecular structure of PLL-g-PEG-HTL.

3.2.2 RGD-functionalized poly-L-lysine-graft-(polyethylene glycol) copolymer (PLL-g-PEG-RGD)

Synthesis of PLL-PEG-RGD was altered from published protocol [164]. 36 mg maleimide-PEG-NHS ester (Mw ~3000 Da) was solved in 0.1 ml HBS buffer (100 mM HEPES, 1 mM EDTA, pH 7.5). 7.6 mg Ac-CGRGDS-COOH peptide (Mw: 636 g/mol, custom-synthesized from Coring System GmbH, Gernsheim/Germany) was solved in 0.1 ml of the same HBS buffer together with 1.5 mg of Tris(2-carboxyethyl)phosphine hydrochloride (TCEP, Mw: 287 g/mol, Sigma-Aldrich), check the pH of TCEP in HBS buffer (pH-indicator paper). Both solutions were mixed for 15 minutes at room temperature for the coupling of cysteine-containing RGD peptide to maleimide-PEG-NHS. Afterwards, the mixture was added to a solution of 7.5 mg poly-L-lysine hydrobromide (Mw: 15.000-30.000 g/mol, Sigma-Aldrich) in 0.3 ml HEPES buffer (100 mM HEPES, 1 mM EDTA, pH 7.5). After overnight stirring at room temperature, the reaction mixture was dialyzed (Slide-A-Lyzer 10 kDa) against MilliQ water for 24 hours. The sample was lyophilized, resulting in a white powder.

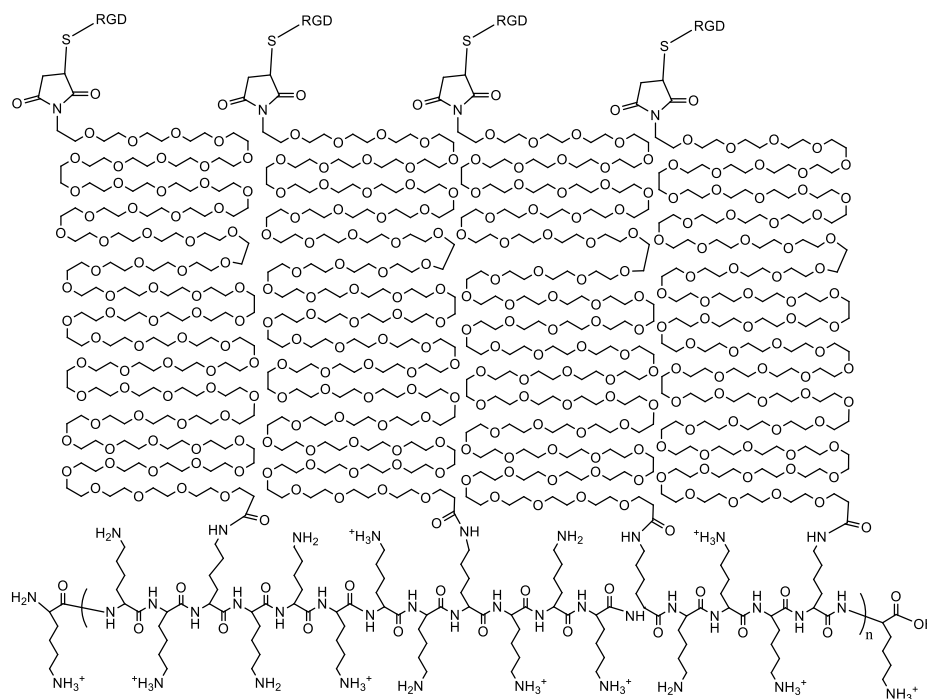


Figure 17: Molecular structure of PLL-g-PEG-RGD.

3.3 Stamp manufacturing and microcontact printing

Poly(dimethylsiloxane)(PDMS) stamp manufacturing was carried out by molding on a microstructured custom-designed gold-master plate (NB Technologies). In order to avoid PDMS sticking to the gold-master, it was first modified with a self-assembling monolayer of 1-octadecane-thiol, generated via incubation with 10 mM 1-octadecane-thiol in acetonitrile overnight. Unreacted thiols were removed by excessive washing with acetonitrile and chloroform and the sides of the gold-master were sealed with aluminum foil and adhesive tape. PDMS was generated by mixing and stirring of basic elastomer (Sylgard 184, Dow Chemicals) with the curing agent (Dow Chemicals) in a 10:1 ratio and with a final volume of 40-50 ml. Mixture was poured onto the sealed gold-master and placed in a desiccator to carefully remove air bubbles and to avoid defects of the stamps micropattern. Polymerization was carried out overnight at 75°C, following careful detachment from the gold-master and cutting of the PDMS stamps with a scalpel.

Before first use and after each subsequent use, PDMS stamps were sonicated for 15 min in EtOH (p.a.), followed by 15 min in MQ-water. Equal amounts of microscopy coverslides and smaller coverslides (\varnothing 24mm, 1.5 & \varnothing 12mm) were plasma-cleaned. Stamps were wetted by placing them with the pattern facing upwards, adding a 10 μ l droplet of PLL-PEG-HTL (0.5 mg/ml) via pipetting on top and covering the stamp with a small \varnothing 12mm coverslide for 10 min. After discarding the small coverslide, remaining liquid drops were

removed by washing with MQ water and the stamp was gently blown dry with N₂ gas. For printing, stamps were pressed with small weights onto microscopy coverslides (ø 24mm) for 10 min. After carefully removing the stamps, microscopy coverslides were backfilled in order to functionalize remaining bare glass. Depending on cell type and experiment, pure PLL-PEG-RGD or a mixture with PLL-PEG-Methoxy (Meo, SurfaceSolutions GmbH) can be employed. For HeLa cells, mixture of 20% PLL-PEG-RGD with 80% PLL-PEG-Meo (each 0.5 mg/ml) was used for backfilling, by sandwiching two microscopy coverslides with 10 µl for 10 min. Coverslides were washed in MQ-water, gently blown dry with N₂ gas and stored in 3.5 cm petri dishes at 4°C for subsequent cell seeding. Stamps were repeatedly used for wetting and printing and were cleaned afterwards as described above. Following the same protocol, micropatterns with reduced binding sites were generated for single-molecule experiments. To this end, a mixture of 0.5% PLL-PEG-HTL with 99.5% PLL-PEG-Meo (each 0.5 mg/ml) was used instead of 100% PLL-PEG-HTL for microcontact printing. PLL-PEG-Meo was commercially available (SurfaceSolutions GmbH), while PLL-PEG-HTL and PLL-PEG-RGD were kindly provided by Sara Löchte [164].

3.4 Fluorescence microscopy and data analysis

3.4.1 Total internal reflection fluorescence microscopy (TIRFM)

Ensemble imaging of *in vitro* micropatterning, live cell micropatterning, as well as single cell pull-down (SiCPull) of a high density micropattern were acquired via TIRFM, using an inverted IX81 microscope (Olympus) with an NA 1.49 oil immersion UAPON 60x TIRF objective (Olympus) for TIR excitation, a 4-Line TIRF condenser (Olympus), a laser system (Olympus) containing a 405 nm 100 mW diode laser, a 488 nm 150mW diode laser, a 561 nm 150 mW diode laser and a 640 nm 140 mW diode laser. Images were acquired using a scientific CMOS camera ORCAFlash 4.0 (Hamamatsu), featuring a pixel size of 6.5 µm x 6.5 µm, 2048 x 2048 pixels and using a fixed exposure time of 32 ms with a typical power output of 0.1 - 1 mW at the objective. DIC imaging was carried out with a 100 W halogen lamp for transmission light, utilizing a Mid-long working distance condenser IX2-LWUCD, a polarizer (U-POT), a DIC prism for 60x objective (IX2-MDIC60), a DIC slider (U-DICTS) and a DIC analyzer (IX2-MDICT).

Single molecule imaging for *in vitro* experiments and single molecule single cell pull-down (SM-SiCPull) was acquired via TIRFM using an inverted IX-83 microscope (Olympus) with

an NA 1.49 oil immersion UAPON 100x TIRF objective (Olympus) for TIR excitation, an additional 1.6x optovar lens, a 4-Line TIRF condenser (Olympus), a 405 nm 100 mW diode laser (CrystaLaser), a 488 nm 200 mW laser diode (Omicron), a 561 nm 500 mW fiber laser (MPB Communications) and a 642 nm 500 mW fiber laser (MPB Communications). The iXon Ultra 897 EMCCD camera (Andor) was used for acquisition at an EM gain of 300, featuring a pixel size of 16 μm x 16 μm , 512 x 512 pixels and using a fixed exposure time of 32 ms with a typical power output of 1-2 mW at the objective.

3.4.2 Bait specific fluorescence contrast analysis

Accumulation of proteins in micropatterns was analyzed as the fluorescence contrast of the micropattern, based on the fluorescence intensity inside and outside the pattern, as well as the camera offset intensity. In case of live cell micropatterning, the capability to pull-down prey proteins into a micropattern depends strongly on the saturation of immobilized bait protein in the micropattern. However, transient transfection can lead to an overexpression of bait proteins that exceeds the binding capacity of a micropattern. In turn, micropattern oversaturation creates a background of non-immobilized bait, which can also interact with the prey, thus reducing both observable fluorescence contrasts. For this purpose, a normalized fluorescence contrast analysis was employed, in which the contrast of the captured bait and prey proteins was corrected for the ratio of directly immobilized proteins within the micropattern. This allowed the statistical analysis of transiently transfected cells that exhibited fluctuating protein expression.

For evaluation, ImageJ can be used in order to select regions of interest (ROI) in the respective regions and thus acquire mean fluorescence values per ROI. However, depending on the ROI position, resulting contrast values are susceptible to fluorescence differences within a heterogeneous pattern, resulting in biased evaluation. To this end, a Matlab application was employed, where ROIs are set over the whole cellular micropattern, thus yielding a robust analysis tool. Whole cells can be analyzed by manually defining the outline of the cell shape, while the cellular micropattern and non-patterned area are defined by applying a mask, which exactly matches the features of the employed micropattern. In order to precisely separate the micropattern from the non-patterned background, a small border region of several pixels was excluded from evaluation. Camera offset intensity was obtained by selecting a large region outside of the cell, which was visually devoid of non-specific fluorescence signals. The Matlab application was developed and kindly provided by Christian P. Richter for evaluation.

First, the contrast of immobile bait proteins C_{bait} was calculated following **Equation 1**, using the average cellular fluorescence intensity inside the micropattern ($I_{pattern}$) and outside the micropattern (I_{cell}), as well as the camera offset (I_{offset}).

$$C_{bait} = \frac{(I_{pattern} - I_{cell})}{(I_{pattern} - I_{offset})} \quad \text{Equation 1}$$

Subtracting ($I_{pattern} - I_{cell}$) gives the micropatterned bait protein signal above the background signal inside the cell, whereas subtracting ($I_{pattern} - I_{offset}$) gives the micropatterned bait signal above the camera offset. The contrast C_{bait} is then calculated as the quotient of micropatterned bait over total cellular proteins, giving values of C_{bait} between 0 - 1, with $C_{bait} \cong 0$ representing a non-specific micropattern and $C_{bait} \cong 1$ representing a highly specific micropattern.

Next, the bait or prey contrast C_{prey} is calculated following **Equation 2**, using the same designations for the average cellular fluorescence intensity inside and outside of the micropattern and camera offset as before.

$$C_{prey} = \frac{(I_{pattern} - I_{offset})}{(I_{cell} - I_{offset})} \quad \text{Equation 2}$$

Subtracting ($I_{pattern} - I_{offset}$) gives the cellular micropatterned prey protein signal above the offset, or co-captured prey protein signal, whereas subtracting ($I_{cell} - I_{offset}$) gives the cellular background signal above the offset, or non-captured prey protein signal. The prey contrast is then calculated as the quotient of both, with $C_{prey} \cong 1$ representing a non-specific prey pattern, indicating no enrichment inside the micropattern and therefore lack of interaction with bait proteins.

Finally, the prey contrast is divided by the bait contrast (**Equation 3**), yielding a corrected prey contrast $C_{prey,corr}$.

$$C_{prey,corr} = \frac{C_{prey}}{C_{bait}} \quad \text{Equation 3}$$

While bait specific contrast analysis enables investigation of cells with different expression levels by correcting for bait specificity, it also generates a bias for non-specific prey patterns. Regarding low bait specificity, even non-specific prey contrast values of $C_{prey} \cong 1$ can be moderately increased.

Moreover, micropatterning of membrane-proteins in the basal plasma membrane tends to bias fluorescence contrast analysis, likely by generating an altered membrane topology. Given the distance sensitive nature of TIRF illumination, even negative controls yielded slightly elevated C_{prey} values of 1 – 1.5 for cytosolic and non-interacting proteins, as demonstrated when exclusively transfecting mEGFP, or when missing the bait protein [103, 158]. These C_{prey} values can be further amplified by correcting for low bait specificity. To this end, corrected contrast values of $C_{prey,corr} \leq 2$ were considered non-specific, whereas micropatterned prey showed significantly higher contrast values.

Note: when employing nanobody live cell micropatterning, the above considerations regarding the bait do not apply to GFP-tagged bait proteins, but to the anti-GFP nanobody immobilized in the micropattern. In this case, the immobilized nanobody is the limiting factor which determines the possible fluorescence contrast of the captured bait and prey proteins. The nanobody contrast is then calculated according to Equation 1, whereas bait and prey contrasts are calculated and corrected according to Equation 2 and 3. For statistical analysis, a two-sample t-tests (Welsh's t-test) [181] was performed in this work, and the significance levels were indicated according to the following p-values of $p > 0.05$ (ns), $p \leq 0.05$ (*), $p \leq 0.01$ (**), and $p \leq 0.001$ (***)

3.4.3 Fluorescence recovery after photobleaching (FRAP)

Fluorescence recovery after photobleaching (FRAP) was carried out using the inverted IX81 microscope (Olympus) for TIRFM with an NA 1.49 oil immersion UAPON 60x TIRF objective as stated in **chapter 3.4.1**. By utilizing pinholes within the TIRF condenser, a circular area with a diameter of $\sim 20 \mu\text{m}$ was placed on the cellular micropattern, bleaching the area by 405 nm excitation for 20 s with a laser power of 20 mW at the objective. Image acquisition before and after bleaching was performed with a typical power output of 0.1 - 1 mW at the objective and an acquisition frame rate of 1 Hz.

Fluorescence intensity values were evaluated using a Matlab application, by selecting rectangular regions of interest (ROI) at multiple positions inside and outside of the cell (alternatively using ImageJ software). ROIs within the bleached area of the micropattern ($I_{ROI_{inside}}$), within the bleached area of the cell ($I_{ROI_{outside}}$), outside of the cell (I_{offset}) and within a non-bleached patterned region (I_{ref}) were set for obtaining mean fluorescence intensity values over time.

FRAP curves were then calculated according to **Equation 4**.

$$I_{corr}(t) = \frac{(I_{ROI_{inside}} - I_{offset}) - (I_{ROI_{outside}} - I_{offset})}{\left[\frac{(I_{ref} - I_{offset})}{(I_{ref_{prebleach}} - I_{offset})} \right]} \quad \text{Equation 4}$$

Here, the offset intensity (I_{offset}) was subtracted from all intensity values, while $(I_{ROI_{inside}} - I_{offset})$ was subtracted with $(I_{ROI_{outside}} - I_{offset})$ in order to remove the recovery rate of free cytosolic background diffusion, thus yielding an unbiased recovery over time within the bleached pattern. $(I_{ref} - I_{offset}) / (I_{ref_{prebleach}} - I_{offset})$ was applied as a correction factor for photobleaching, by utilizing the fluorescence intensity over time within a non-bleached reference pattern $(I_{ref} - I_{offset})$, normalized by the original fluorescence intensity before photobleaching $(I_{ref_{prebleach}} - I_{offset})$.

Obtained FRAP curves were then fitted according to **Equation 5**, assuming a non-diffusion limited recovery, where diffusion is in the range of a few seconds, therefore more rapid than protein binding and thus negligible [182, 183].

$$FRAP(t) = A * (1 - e^{-t/\tau}) + y_0 \quad \text{Equation 5}$$

Obtained τ values serve as the characteristic lifetime of a protein-protein interaction and were displayed as a mean value \pm standard deviation of several analysed cells.

3.4.4 Single Cell Pull-down (SiCPull) to characterize interaction dynamics

SiCPull was carried out by growing WT HeLa cells on 6 cm petri dishes and transfecting them overnight. After washing and resting, cells were seeded on PLL-PEG-HTL micropatterned coverslides, backfilled with PLL-PEG-RGD, and grown over night in medium containing penicillin/streptomycin. Prior to SiCPull experiments, coverslides were incubated with 200 nM of HaloTag-NB for 10 min, thus functionalizing the HTL micropattern with anti-GFP nanobody (NB). Coverslides were then mounted on the inverted IX81 microscope (Olympus) with an NA 1.49 oil immersion UAPON 60x TIRF objective for TIRFM as described in chapter 3.4. Cell lysis was initiated as previously published [160], by adding a lysis buffer (0.1% Triton X-100 in PBS buffer) at the sample stage of the TIRF microscope. Image acquisition was started briefly before addition of the lysis buffer, with an image acquisition time-span of 300 s with an acquisition frame rate of 1 Hz and an alternating excitation at 488 nm and 561 nm. Complex stabilities were determined from the decay of fluorescence intensity as previously published [160]. ImageJ was used for extracting the intensity values over time, plotting the fluorescence

decay according to **Equation 6**, with $F_{inside}(t)$ obtained from a ROI within the patterned region under the cell and $F_{outside}(t)$ as the background signal from a non-patterned region outside of the cellular area.

$$F(t) = F_{inside}(t) - F_{outside}(t) \quad \text{Equation 6}$$

After subtracting the background signal, the fluorescence decay $F(t)$ was normalized according to **Equation 7**, with F_0 being the fluorescence intensity at the beginning of protein complex dissociation at time point zero.

$$f(t) = F(t) / F_0 \quad \text{Equation 7}$$

Timepoint zero was set as the time point when a clear exponential dissociation within the pattern occurred, either at the start of lysis or after disappearing of cellular background signal.

Dissociation rate constants of different STAT complexes were then calculated by fitting of the normalized fluorescence decay, either by mono-exponential fitting according to **Equation 8**, or if rejected via bi-exponential fitting according to **Equation 9**.

$$f(t) = A * e^{-t/\tau} + y_0 \quad \text{Equation 8}$$

$$f(t) = A_1 * e^{-t/\tau_1} + A_2 * e^{-t/\tau_2} + y_0 \quad \text{Equation 9}$$

Dissociation rate constants $k_d[s^{-1}]$ were then calculated as the inverse of the characteristic lifetime values $\tau[s]$.

$$k_d[s^{-1}] = \frac{1}{\tau[s]} \quad \text{Equation 10}$$

3.4.5 Single molecule single cell pull-down (SM-SiCPull)

In order to achieve micropatterns with single molecule density, coverslides with reduced binding sites were prepared by microcontact printing of a mixture of 0.5% PLL-PEG-HTL with 99.5% PLL-PEG-Meo (0.5 mg/ml), backfilled with PLL-PEG-RGD and handled as stated in **chapter 3.3**. Prior to experiments, coverslides were incubated with a mixture of 0.5% HaloTag-NB and 99.5% HaloTag at a total of 200 nM for 10 min, thus generating a single molecule anti-GFP NB micropattern. For SM-SiCPull, cell lysis was initiated by adding a lysis buffer (0.1% Triton X-100 in PBS buffer) for 10 – 30 seconds, followed by fixation with 4% PFA (Para-formaldehyde) in PBS. Cell lysis and protein fixation were carried out at the microscope, with fixation preventing dissociation of co-captured proteins from the complex, thus guaranteeing an unbiased stoichiometry analysis via

single molecule bleaching. Moreover, fixation removed any time limitations due to dissociation, enabling acquisition of the whole coverslide, therefore generating high amounts of single molecule data for statistical analysis.

For single molecule imaging, the inverted IX-83 microscope (Olympus) with an NA 1.49 oil immersion UAPON 100x TIRF objective (Olympus) and an additional 1.6x optovar lens was used for TIR excitation as described in **chapter 3.4.1**. Single molecule bleaching experiments were acquired over 150 frames as fast as possible, using a standard exposure time of 100 ms at an effective interval of ~ 111 ms per frame, averaging fluorescence blinking of mEGFP and yielding robust results under constrained analysis parameters. For bleaching, TIR excitation was used at a combined power output of 9 mW for 488 nm and 3 mW for 405 nm, reducing mEGFP blinking via UV light [184].

3.4.6 Single molecule localization and data analysis

Single molecule data was analyzed using the Matlab applications “SLIMfast” and “BleachCounter”, which were kindly provided by Christian P. Richter. ROIs matching the complete micropattern were set in SLIMfast in order to filter out non-specific background binding. Particles were localized with dataset-derived point spread functions (PSF) at a sub-pixel precision of ~ 16 - 20 nm, using the multiple-target tracing (MTT) algorithm [185] as described previously [186, 187]. Immobile particles within the localized dataset were detected by performing a spatio-temporal DBSCAN as described previously [188], combining localizations over multiple frames within a search radius of 80 nm (4 x localization precision) into a cluster. Immobile clusters of a whole dataset (>1000) were then pooled and their 2D coordinates (x, y) and intensity values over time were exported into the BleachCounter tool to determine complex stoichiometry.

In BleachCounter, the fast step transition and state identification (STaSI) algorithm [189] was used to identify fluorescence bleaching steps of individual molecules. Heterogeneous 2D illumination of the sample was then accounted for by plotting the observed bleaching magnitudes according to their 2D position, thus yielding a spatial fluorophore intensity distribution map. This map was used to extrapolate an illumination profile, either by using a 2D-Gaussian model or via smoothing [190], correlating measured bleaching magnitudes of individual molecules with their 2D position. Finally, an intensity-based stoichiometry analysis was performed by applying a Gaussian mixture model [191] to the whole dataset, yielding the molecule number distribution and a molecule number map, which were displayed in the results section of this work.

4 Results

4.1 Micropatterned surface architectures

In order to assess the quality of the surface micropatterns generated via μ CP, *in vitro* experiments were first carried out to observe binding of HaloTag-fused mEGFP to the HaloTag ligand (HTL) functionalized surface. Micropatterned coverslides were incubated with 200 nM HaloTag-mEGFP fusion proteins for 10 minutes, washed and then observed via TIRFM (**Figure 18**). This revealed a very specific binding of HaloTag-mEGFP into PLL-PEG-HTL micropatterns, matching the employed 5 μ m line/10 μ m space PDMS stamps. Plotting the fluorescence intensity across the indicated yellow region of interest (ROI) reveals a high contrast of 20:1 of mEGFP against the background fluorescence signal, demonstrating the maximum contrast in absence of non-specific or background signals.

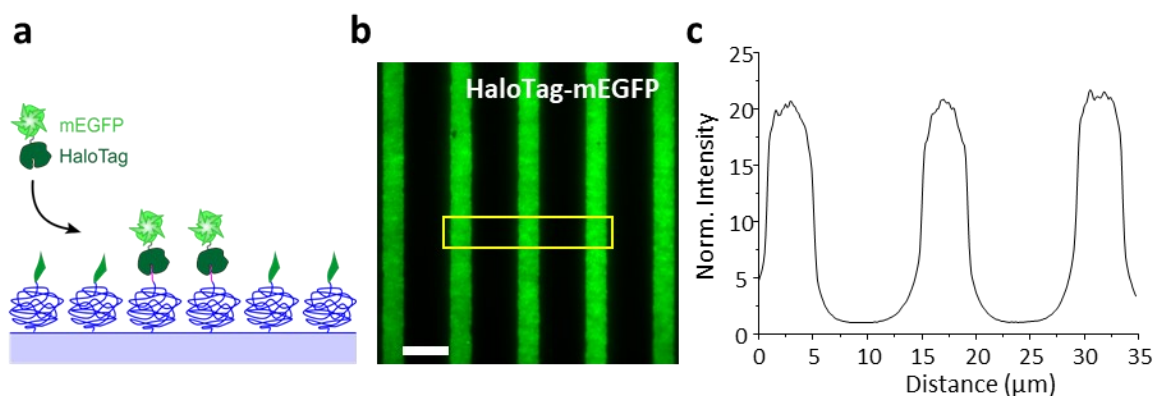


Figure 18: *In vitro* capturing of HaloTag-mEGFP into HTL micropatterns. (a) Scheme illustrating a coverslide micropatterned with PLL-PEG-HTL and PLL-PEG-RGD. Purified HaloTag-mEGFP is specifically binding the micropatterned HaloTag ligand (HTL). (b) TIRFM imaging of the micropatterned HaloTag-mEGFP. Yellow box indicates the ROI evaluated in (c). Scale is 10 μ m. (c) Line profile of the normalized fluorescence intensity plotted against the axial distance of the ROI.

4.1.1 Generic nanobody live cell micropatterning

Our previously reported methodologies relied on fusing a specific protein of interest with the HaloTag, in order to achieve a live cell micropatterning of bait proteins on PLL-PEG-HTL surfaces [158]. This work however aimed to implement a generically applicable anti-GFP nanobody (NB) live cell micropatterning approach, enabling specific capturing of a plethora of GFP-tagged proteins which are often readily available in many microscopy or spectroscopy focused laboratories. In order to achieve this goal, the 'NB construct' (HaloTag-BFP-TMD-NB) was designed for surface immobilization, fluorescence visualization and intracellular capturing of GFP-fused bait proteins and interacting prey proteins, enabling analysis of protein interactions and kinetics.

4.1.2 Immobilization of mEGFP in an anti-GFP NB micropattern

As an *in vivo* proof-of-concept experiment for live cell NB micropatterning, HeLa cells were transiently transfected with HaloTag-mTagBFP-TMD-NB and co-transfected with mEGFP before being seeded overnight on coverslides. These were micropatterned with PLL-PEG-HTL for immobilization and PLL-PEG-RGD for cellular adherence (**Figure 19**). TIRFM imaging revealed immobilization of the NB construct into PLL-PEG-HTL micropatterns through specific HaloTag binding, matching the employed 5 μm line/10 μm space PDMS stamps. Simultaneously, cytosolic mEGFP localized into the same micropattern, being specifically captured to the basal membrane by the anti-GFP NB. Plotting the fluorescence intensity across the indicated region of interest (ROI) reveals an mEGFP fluorescence contrast of 8:1 inside the micropattern, which is typical for intracellularly immobilized bait. Interestingly, the majority of the NB is localized within the micropattern, whereas a cytosolic mEGFP background is still visible.

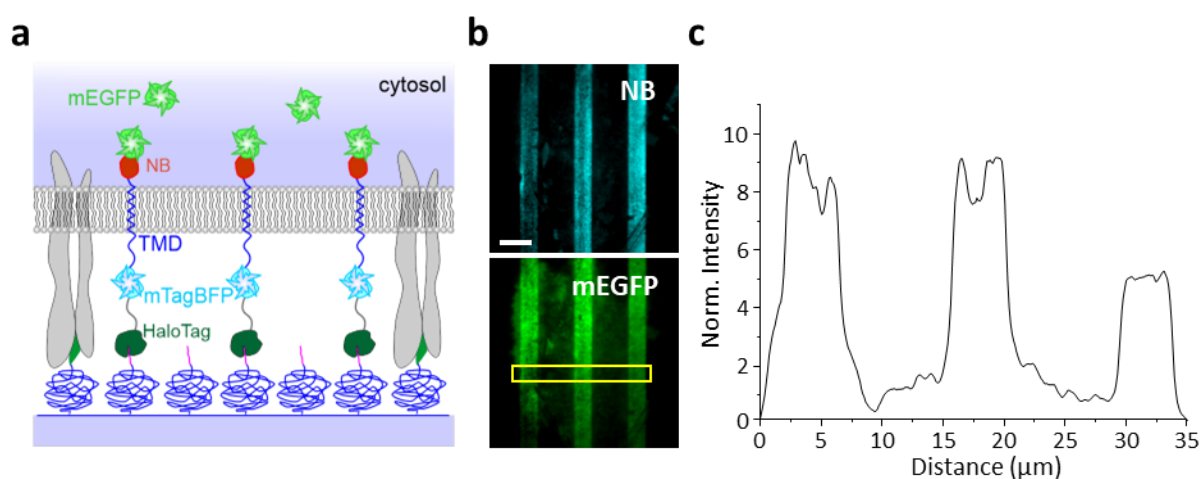


Figure 19: Live cell micropatterning of mEGFP. (a) Scheme illustrating immobilization of an anti-GFP NB into micropatterns, via fusion to a transmembrane domain (TMD), coupled to mTagBFP for visualization and HaloTag for immobilization. mEGFP is specifically recruited into the anti-GFP NB micropattern. (b) TIRFM Images of HaloTag-mTagBFP-TMD-NB (blue channel) and mEGFP (green channel). Yellow box indicates ROI analyzed in (c). Scale is 10 μm . (c) Line profile of the fluorescence intensity of mEGFP, plotted against the axial distance of the ROI. Fluorescence intensity was normalized to 0 for offset and 1 for cellular background. Data kindly provided by Sara Löchte.

These results confirm the HaloTag-mTagBFP-TMD-NB construct's viability to generate live cell micropatterns and to specifically capture mEGFP as bait in a pull-down assay. However, the enrichment of bait proteins is heavily dependent on cellular expression levels, which can be seen from the visible background of cytosolic mEGFP (**Figure 19b**, green channel). In order to eliminate expression levels as a source of bias between cells and experiments, a statistical analysis was henceforth carried out, while correcting for fluorescence intensity signals of the initially micropatterned proteins (see **chapter 3.4.2**).

4.2 Nanobody live cell micropatterning

4.2.1 Characterizing the interaction of USP18 and ISG15

The focus of this work was to investigate the interplay of effector proteins and negative feedback regulators of type I IFN signaling, which in turn demonstrates the potential and reliability of an anti-GFP nanobody-based live cell micropatterning assay. As a first step, the interaction between USP18 and ISG15 was investigated, which canonically consists of the enzymatic activity of USP18 to cleave its substrate ISG15 from conjugated proteins in a process called de-ISGylation [100]. Uniquely to type I IFN signaling, this isopeptidase activity of USP18 against di-ubiquitin-like ISG15 is not required, as USP18 rather functions as a non-enzymatic inhibitor to destabilize the ternary IFNAR complex at the plasma membrane [52, 53]. In turn, free cytosolic ISG15 stabilizes cytosolic USP18 and is thus required for a prolonged negative feedback activity and the α/β differential [57, 109]. It was therefore of great interest to characterize the interaction between USP18 and ISG15 in the cellular context, by employing nanobody live cell micropatterning.

For this characterization, HeLa cells transiently expressing HaloTag-mTagBFP-TMD-NB, mEGFP-USP18 and fSNAP-ISG15 later labeled with BG-SiR were seeded overnight on PLL-PEG-HTL micropatterned coverslides (**Figure 20**). Following TIRFM imaging, these coverslides displayed a specific capturing of mEGFP-USP18 as bait in the anti-GFP NB micropattern, as well as a corresponding capturing of fSNAP-ISG15 as prey into the same micropattern (**Figure 20a, I**, left). Plotting the fluorescence intensity of all channels across the indicated rectangular ROI illustrates the protein capturing inside the micropattern, resulting in a distinct fluorescence contrast clearly above the cytosolic cellular background (**Figure 20a, I**, right). For quantification, fluorescence contrast values of whole cells were evaluated (**chapter 3.4.2**), with mEGFP-USP18 exhibiting a mean contrast of 2.4 ± 0.8 ($n = 20$), and fSNAP-ISG15 a mean contrast of 2.5 ± 0.8 ($n = 20$), confirming their specific capturing as bait and prey, respectively (**Figure 20c, I**).

To validate the specificity of this assay, two negative controls were additionally carried out, this time employing USP18-mCherry to carry out the micropatterning assay in absence of a GFP-tagged bait protein (**Figure 20b, II**), and utilizing HaloTag-mTagBFP-TMD to carry out the assay in absence of any nanobody, thus lacking the ability to pull-down bait proteins (**Figure 20b, III**).

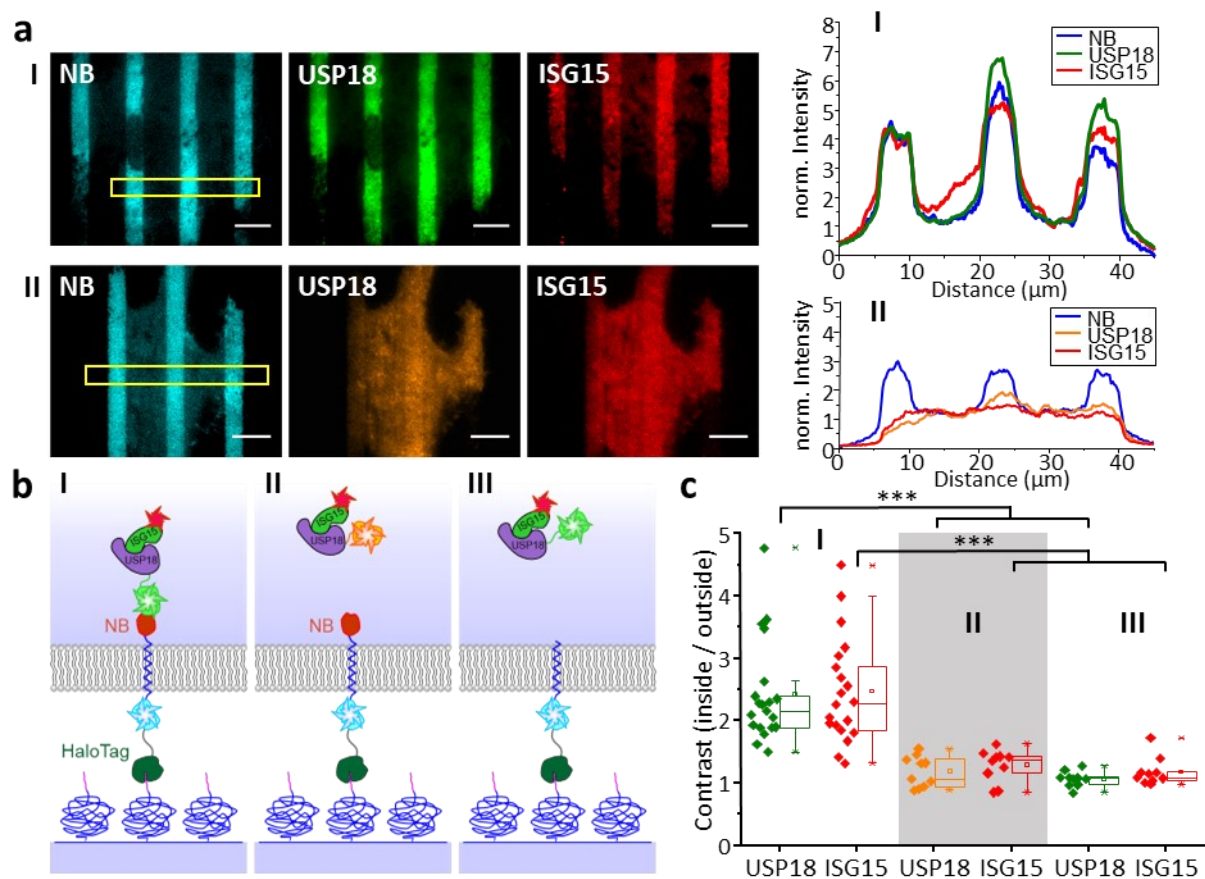


Figure 20: Fluorescence contrast interaction analysis of USP18 and ISG15. (a) Fluorescence images of HeLa cells transiently expressing HaloTag-mTagBFP-TMD-NB (blue channel), mEGFP-USP18 (green channel), and fSNAP-ISG15 labeled with BG-SiR (red channel) on top (I), or alternatively USP18-mCherry (orange channel) on bottom (II). Scale is 10 μm . Yellow box indicates ROI of the line profiles in shown on the right. (b) Scheme illustrating the anti-GFP NB binding experiment (I) and negative controls in absence of mEGFP or absence of NB (II, III). (c) Box plot showing the recruitment into NB micropatterns of the binding experiment (I), and negative controls (II, III). Binding is determined as the contrast of the fluorescence signal inside and outside the patterns. Each dot in the boxplot represents a cell. Previously published by us in [104] and adapted for this thesis.

Regarding the former negative control, TIRFM imaging revealed a clear absence of both USP18-mCherry and fSNAP-ISG15 in the NB micropattern, showing a normalized fluorescence intensity similar to the fluorescence background of the cell (**Figure 20a, II**). The same holds true for the latter negative control, where neither mEGFP-USP18 nor fNSPA-ISG15 were captured in absence of a NB (**III**, not shown). For statistical analysis, both negative controls were again evaluated, yielding a fluorescence contrast of 1.2 ± 0.2 ($n = 10$) for USP18-mCherry and 1.3 ± 0.2 ($n = 10$) for fSNAP-ISG15 (**Figure 20c, II**), as well as 1.1 ± 0.1 ($n = 10$) for mEGFP-USP18 and 1.2 ± 0.2 ($n = 10$) for fSNAP-ISG15 (**Figure 20c, III**). These results clearly confirmed the specificity of the generic anti-GFP nanobody assay, as no proteins were localized within the micropattern either in the absence of a GFP-tagged bait protein or in the absence of a micropatterned nanobody.

Considering that the fluorescence contrast analysis depends on several factors, it can be regarded as a semi-quantitative assay. This is because the quality of the surface functionalization, as well as the expression levels of the NB construct used for immobilization, and the expression levels of GFP-tagged bait proteins and potential prey proteins ultimately affect the observable fluorescence intensity during TIRFM imaging. To precisely characterize the interaction dynamics between USP18 and ISG15, another application of the NB live cell micropatterning was therefore employed.

Here, a fluorescence recovery after bleaching (FRAP) experiment was performed, in order to quantitatively investigate the interaction kinetics. Similar to the previous experiments, HeLa cells transiently expressing HaloTag-mTagBFP-TMD-NB, mEGFP-USP18 and fSNAP-ISG15 labeled with BG-SiR were seeded on micropatterned coverslides (**Figure 21**).

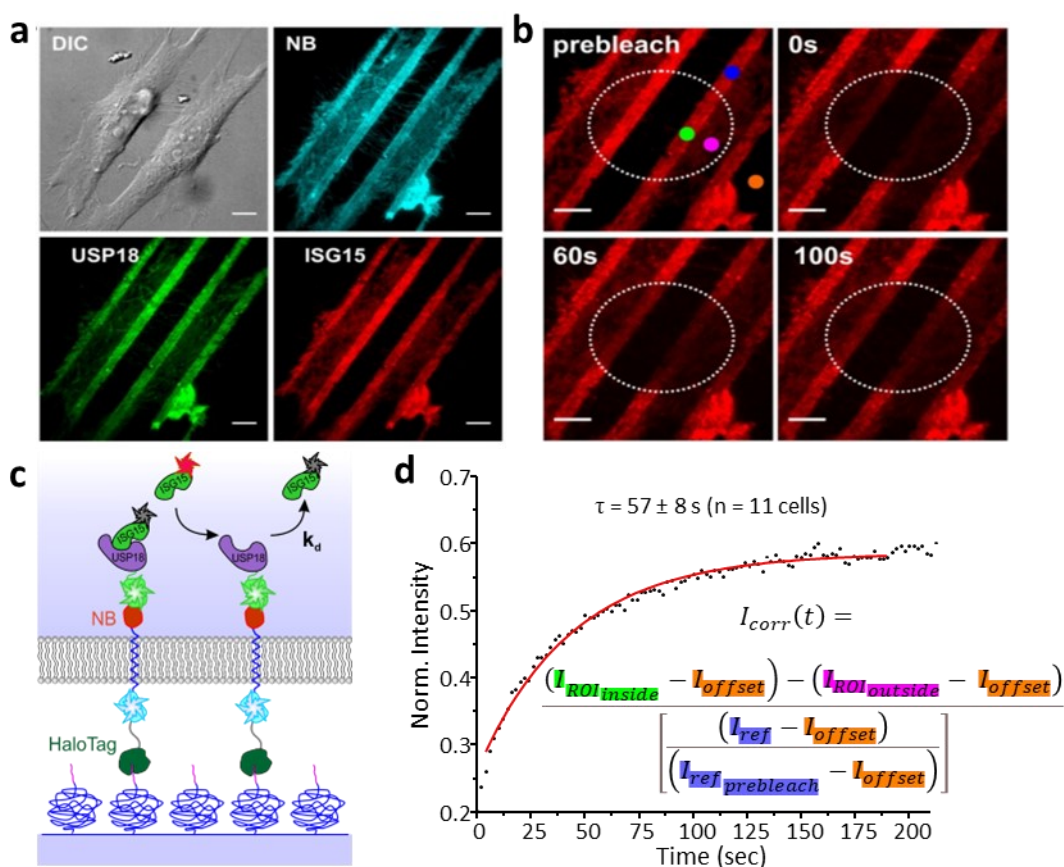


Figure 21: Quantifying the stability of USP18-ISG15 via FRAP. (a) DIC and fluorescence images of HeLa cells transiently expressing HaloTag-mTagBFP-TMD-NB (blue channel), mEGFP-USP18 (green channel), and fSNAP-ISG15 labeled with BG-SiR (red channel). Scale is 10 μm . (b) FRAP of the circular area (dashed line) of BG-SiR labeled ISG15, pre-bleaching, 0 seconds, 60 seconds, and 100 seconds after photobleaching. Scale is 10 μm . (c) Scheme illustrating fluorescence recovery via exchange of bleached ISG15 (black label) with fluorescent ISG15 (red label) according to the dissociation constant (k_d). (d) Exemplary fluorescence recovery of ISG15 interacting as prey with micropatterned USP18 as bait. FRAP curve corrected for background and photobleaching according to **Equation 4** shown in the inset (same coloring as in b). Fluorescence intensity before photobleaching was normalized to 1. Monoexponential fitting depicted as a solid line. Previously published by us in [104] and adapted for this thesis.

Importantly, HeLa cells with a visible background of cytosolic ISG15 were specifically chosen during TIRFM, performing a FRAP experiment by bleaching the SiR label of ISG15 in a small circular area, using a short burst of high power 640 nm laser excitation (**Figure 21b**). Afterwards, bleached proteins dissociate according to their dissociation rate, or complex stability, and are exchanged by fluorescent proteins from the cytosolic background, which results in a visible recovery of the fluorescence signal. Furthermore, control experiments were performed, excluding recovery by potentially dissociating transmembrane HaloTag-mTagBFP-TMD-NB proteins or GFP-fused bait proteins (not shown). Plotting the normalized and corrected intensity values over time and applying a monoexponential fit, as stated previously (**chapter 3.4.3**), then yielded a characteristic lifetime of $\tau = 57 \pm 8$ s ($n = 11$) for the interaction between USP18 and ISG15 (**Figure 21b**). Considering the canonical isopeptidase activity of USP18 and the de-ISGylation of the substrate ISG15 [100], the interaction between USP18 and ISG15 appears unexpectedly stable. Moreover, it is quite comparable to the lifetime of $\tau = 53 \pm 28$ s ($n = 8$) of micropatterned STAT2 (bait) interacting with intracellular USP18 (prey) [103]. The next step was therefore to investigate the effects of the structural domains of USP18 and ISG15 on their protein-protein interaction.

4.2.2 Structural investigation of individual USP18 and ISG15 domains

Dedicated to characterizing the USP18-ISG15 interaction in more detail, the influence of different regions and domains of USP18 and ISG15 were investigated, based on their published structural basis [109] (**chapter 1.3.3**). Note that instead of N-terminally fused mEGFP-USP18, C-terminally fused USP18-mEGFP was used in the following, as this template was more successful in cloning subsequent USP18 truncations. Again, anti-GFP NB pull-down experiments were performed, utilizing HeLa cells transiently expressing HaloTag-mTagBFP-TMD-NB and a variety of USP18-mEGFP truncations as bait, combined with several BG-SiR labeled fSNAP-ISG15 truncations as prey (**Figure 22**).

First the N- and C-terminal domains of di-ubiquitin-like ISG15 were investigated, utilizing USP18-mEGFP as bait, and either fSNAP-ISG15 (WT), fSNAP-C-ISG15 (C-term.), or fSNAP-N-ISG15 (N-term.) as prey. Here, USP18-mEGFP was efficiently captured as bait across all three experiments, with contrast values of 8.1 ± 1.8 ($n = 18$), 8.3 ± 3.3 ($n = 20$) and 7.5 ± 2.0 ($n = 18$) (**Figure 22b**). Both fSNAP-ISG15 and fSNAP-C-ISG15 exhibited a high contrast when micropatterned as prey, with contrast values of 9.3 ± 5.9 ($n = 18$) and 8.4 ± 4.4 ($n = 20$) respectively, whereas fSNAP-N-ISG15 was unable to interact

with USP18, only yielding a contrast of 1.8 ± 0.6 ($n = 18$). These results are thus in perfect agreement with the structural-based expectation that the N-terminal ISG15 domain is not involved in interacting with USP18. Interaction instead solely relies on the C-terminal ISG15 domain, demonstrated by equally strong interactions of full-length ISG15 and C-terminal ISG15 with USP18. Additionally, the ISG15 domains were quantitatively analyzed in the next chapter, again resolving their interaction dynamics via FRAP.

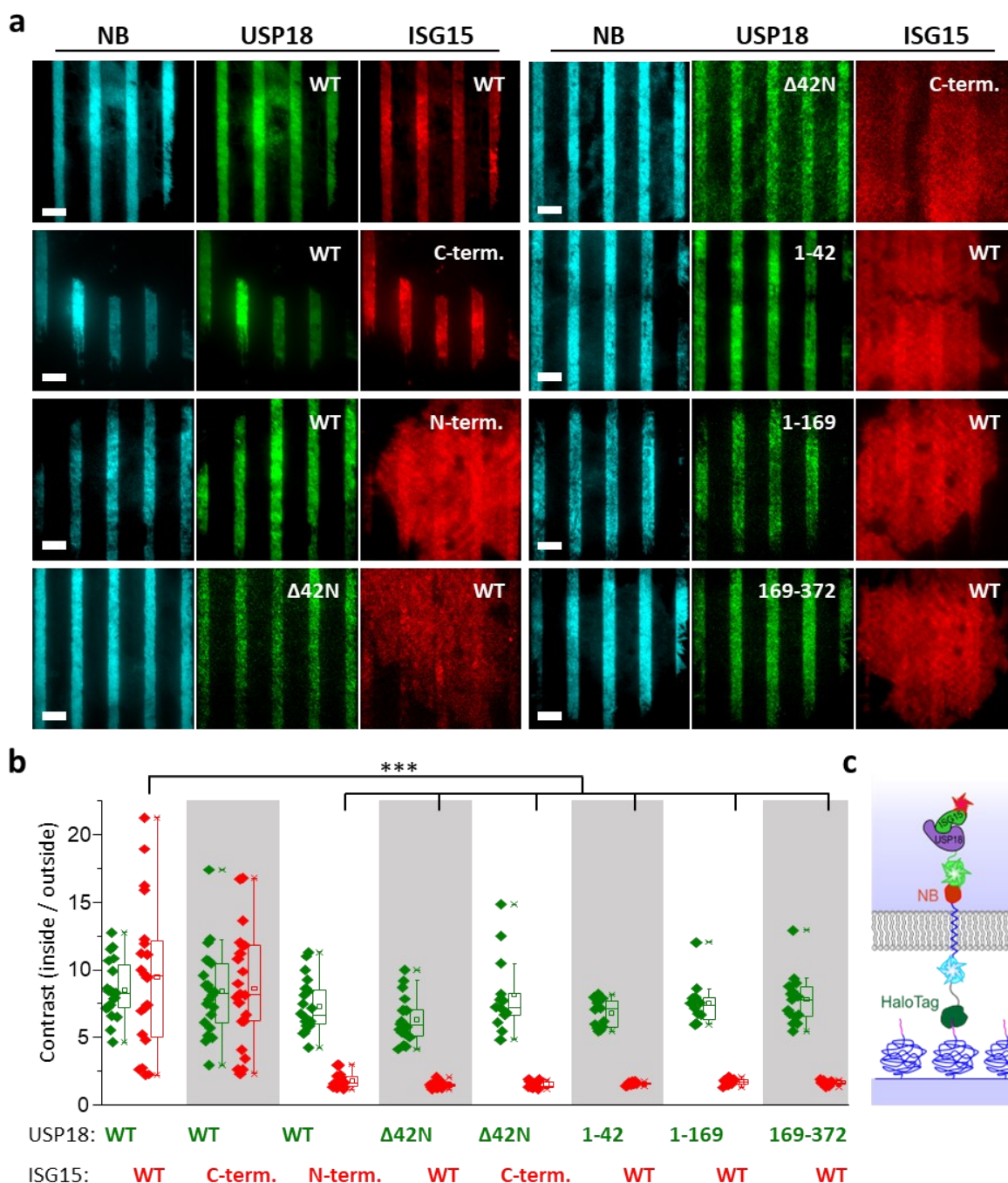


Figure 22: Interaction of USP18 with ISG15. (a) Fluorescence images of HeLa cells transiently expressing HaloTag-mTagBFP-TMD-NB (blue channel), as bait either full-length USP18-mEGFP (WT), USP18 Δ 42N-mEGFP (Δ 42N), USP18-1-42-mEGFP (1-42), USP18-1-169-mEGFP (1-169), or USP18-169-372-mEGFP (169-372) (green channel) and as prey either fSNAP-ISG15 (WT), fSNAP-C-ISG15 (C-term.), or fSNAP-N-ISG15 (N-term.), labeled with BG-SiR (red channel). Scale is 10 μ m. (b) Fluorescence contrast analysis. Each dot in the boxplot represents a cell. (c) Scheme illustrating the immobilization into micropatterns.

Next, the unstructured N-terminus of USP18 was investigated, which covers amino acids 1-42 and is known to feature two additional translation initiation sites downstream of AUG1, namely the non-canonical start codon CUG16, and start codon AUG36, which leads to expression of an N-terminal truncated isoform [110]. Both isoforms are functionally able to deISGylate target proteins, but the full-length isoform is mainly localized within the cytosol, whereas the N-terminal truncated isoform is equally distributed between cytosol and nucleus [110] (**chapter 1.3.3**). However, the influence of the USP18 N-terminus on interaction with ISG15 remained to be tackled. To this end, USP18 Δ 42N-mEGFP (Δ 42N) was utilized as bait, where the first 42 amino acids were truncated, in conjunction with fSNAP-ISG15 (WT) and fSNAP-C-ISG15 (C-term.). For both cases, bait-capturing was efficient, featuring contrast values of 6.3 ± 1.8 ($n = 16$) and 7.6 ± 2.2 ($n = 11$) respectively. However, both prey proteins were seemingly unable to interact with USP18 Δ 42N, as fSNAP-ISG15 yielded a contrast of only 1.5 ± 0.2 ($n = 16$) and fSNAP-C-ISG15 a contrast of 1.5 ± 0.2 ($n = 11$). Albeit being an unstructured region not covered via crystallography, these results imply that the N-terminus of USP18 is either crucial for interaction with ISG15, or crucial for proper folding of the protein, thus requiring to further resolve its molecular mechanisms.

Attempting to further investigate the unstructured N-terminus itself, USP18-1-42-mEGFP (1-42) was used as bait, consisting of only the first 42 amino acids, in order to examine whether this region could be able to interact with fSNAP-ISG15 on its own. Again, capturing of bait was efficient, with USP18-1-42-mEGFP exhibiting a contrast of 6.6 ± 1.1 ($n = 11$), whereas the prey was not able to interact, with fSNAP-ISG15 yielding only a contrast of 1.6 ± 0.1 ($n = 11$). While mEGFP fluorescence at least indicates expression of USP18-1-42-mEGFP, it remains highly ambiguous whether such a small USP18 fragment is also functional. Nevertheless, the importance of the N-terminus was clearly identified, beyond its role of expressing isoforms located in different cellular compartments [110].

Finally, ISG15 binding boxes IBB1 and IBB2 were investigated, by employing USP18-1-169-mEGFP (1-169) containing the thumb-domain and residues A138 and L142 of IBB1, as well as USP18-169-372-mEGFP, featuring the finger and palm domains, including residues S192 and H251 of IBB1 and Q259 and W262 of IBB2 [109]. Again, both bait proteins were successfully captured into micropatterns, with USP18-1-169-mEGFP exhibiting a contrast of 7.7 ± 1.8 ($n = 10$) and USP18-169-372-mEGFP a contrast of 7.8 ± 1.9 ($n = 13$), but the prey was unable to be co-captured, with fSNAP-ISG15 in

both cases yielding a low contrast of 1.7 ± 0.2 ($n = 10$) and 1.7 ± 0.1 ($n = 13$), respectively. Although both USP18-truncations featured ISG15 binding residues, none were able to achieve co-capturing of ISG15, likely due to a lack of structural features. Seeing that USP18 is not an easily segmented multi-domain protein (**chapter 1.3.3**), these larger truncations are likely non-functional and therefore unable to interact with its target protein ISG15. Instead of truncating half of the protein, mutations of specific residues would rather be required in the future, in order to investigate each amino-acids contribution individually.

4.2.3 Resolving USP18-ISG15 interaction dynamics via FRAP

As demonstrated by the previous experiments, both full-length ISG15 and the C-terminal ISG15 domain feature comparably high fluorescence contrasts values upon binding micropatterned USP18. These results were in perfect agreement with structural data, given that only the C-terminal ISG15 domain is reportedly involved in USP18 binding. As stated previously however, the fluorescence contrast analysis serves only as a semi-quantitative method, allowing to observe relative changes between similar sets of experiments, but not to investigate and characterize interaction kinetics of PPIs. To this end, another fluorescence recovery after bleaching (FRAP) experiment was performed, to quantitatively investigate whether the individual C-terminal ISG15 domain interacts as strongly with USP18 as full-length ISG15. Therefore, HeLa cells transiently expressing HaloTag-mTagBFP-TMD-NB, USP18-mEGFP and a variant of fSNAP-ISG15 later labeled with BG-SiR were seeded on micropatterned coverslips, as in previous experiments (**Figure 23a, left**).

Again, HeLa cells with a slightly visible background of cytosolic ISG15 were specifically chosen during TIRFM, performing a FRAP experiment by specifically bleaching the SiR label of ISG15 in a small circular area, using a short burst of high power 640 nm laser excitation (**Figure 23a, right**). As bleached ISG15 are exchanged by fluorescent proteins from the cytosolic background, a visible recovery of the fluorescence signal occurs. Plotting the normalized and corrected intensity values over time and applying a monoexponential fit (**chapter 3.4.3**) again yielded their characteristic lifetime τ (**Figure 23b**). Interaction with full-length ISG15 exhibited a mean lifetime of $\tau = 54.2 \pm 10.1$ s ($n = 14$), whereas C-terminal ISG15 results in $\tau = 68.9 \pm 26.3$ s ($n = 7$). Both values are therefore in good agreement with each other and do not differ significantly from each other, with a p-value of $p = 0.17$. It is also worth noting that the previous FRAP experiment yielded a similar lifetime of $\tau = 57 \pm 8$ s ($n = 11$) for the interaction between N-terminally

fused mEGFP-USP18 and fSNAP-ISG15, thus confirming both experimental results. However, recovery of the N-terminal ISG15 domain could not be determined, as 11 out of 11 cells did not show a stronger recovery in the bleached micropattern than the recovery of the non-specific cytosolic signal (**Figure 23b, blue**). Again, this also confirms the earlier results that USP18 interacts solely with the C-terminal domain of ISG15 and that the N-terminal domain is not involved.

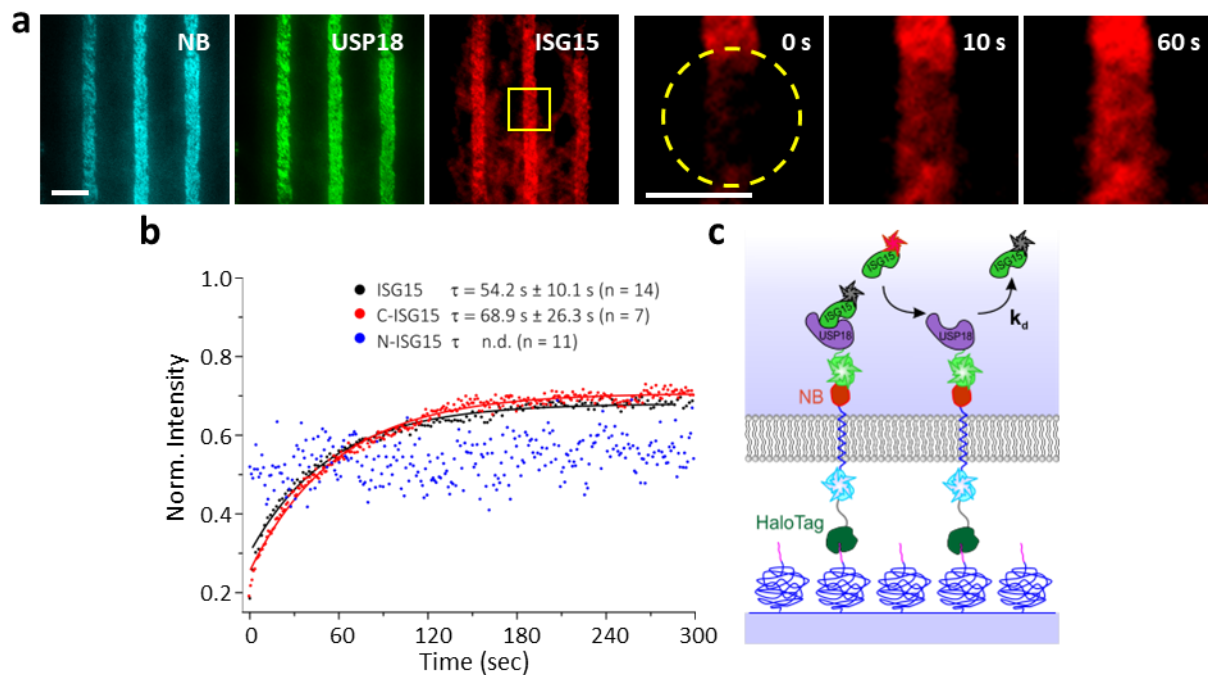


Figure 23: Interaction Dynamics of ISG15 and USP18. (a) Left: Fluorescence images of HeLa cells transiently expressing HaloTag-mTagBFP-TMD-NB (blue channel), USP18-mEGFP (green channel) and fSNAP-ISG15 labeled with BG-SiR (red channel). Yellow square indicates the zoom-in of the right row, scale is 10 μm . Right: FRAP of the circular area (dashed line) of BG-SiR labeled ISG15, 0 seconds, 10 seconds, and 60 seconds after photobleaching. Scale is 10 μm . (b) Exemplary fluorescence recovery of ISG15 (black), C-terminal ISG15 domain (C-ISG15) (red), and N-terminal ISG15 domain (N-ISG15) (blue), interacting as prey with micropatterned USP18 as bait. Fluorescence intensity before photobleaching was normalized to 1. Monoexponential fitting depicted as a solid line. (c) Scheme illustrating fluorescence recovery via exchange of bleached ISG15 (black label) with fluorescent ISG15 (red label) according to the dissociation constant (k_d).

4.2.4 Nanobody live cell micropatterning to examine cytosolic competition

Concluding the characterization of the interaction between USP18 and ISG15, the next step was to investigate their interplay with the effector protein STAT2. To reiterate, the negative feedback mechanism of type I IFN signaling heavily relies on USP18, which exhibits two distinct interaction partners. First, STAT2 is required as a docking site for USP18 recruitment to IFNAR2 and is therefore crucial for the negative feedback mechanism [103]. Second, interaction with the di-ubiquitin like protein ISG15 stabilizes cytosolic USP18 and is therefore required for a prolonged negative feedback activity and the α/β differential [57, 109].

Featuring two prominent binding partners immediately raised the question whether both ISG15 and STAT2 would be able to simultaneously interact with USP18. Again, this could easily be investigated via live cell micropatterning, capturing readily available GFP-fusion proteins. In this instance however, pull-down of GFP-fused USP18 would not have been advisable, as both STAT2 and ISG15 would be able to bind individual USP18 bait proteins and co-localize within the micropattern, thus yielding an obscured result. Instead, either ISG15 or STAT2 was pulled down as bait, while observing co-recruitment of transiently expressed proteins of interest into the same micropattern as prey.

First, HeLa cells transiently expressing HaloTag-mTagBFP-TMD-NB, mEGFP-ISG15, USP18-mCherry and fSNAP-STAT2, later labeled with BG-SiR, were seeded overnight on PLL-PEG-HTL micropatterned coverslides (**Figure 24**). These coverslides were imaged via TIRFM, revealing specific capturing of mEGFP-ISG15 as bait into NB micropatterns, which in turn co-captured USP18-mCherry as prey into the micropattern (**Figure 24a**). fSNAP-STAT2 on the other hand did not colocalize with ISG15 and USP18, displaying only a faint contrast across the stripes of the patterned cell.

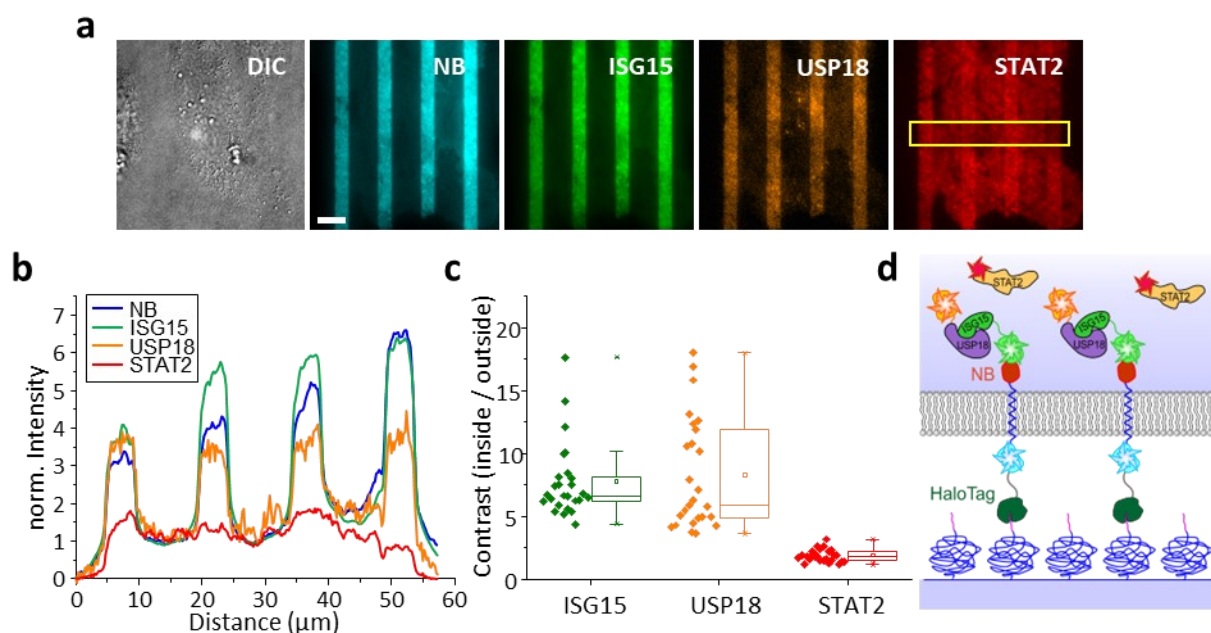


Figure 24: Competition between ISG15 and STAT2 for USP18. (a) DIC and fluorescence images of HeLa cells transiently expressing HaloTag-mTagBFP-TMD-NB (blue channel), mEGFP-ISG15 (green channel), USP18-mCherry (orange channel) and fSNAP-STAT2 labeled with BG-SiR (red channel). Scale is 10 μm . Yellow box indicates ROI of the line profile in (b). (b) Line profile of the fluorescence intensity in each channel, plotted against the axial distance of the ROI. Fluorescence intensity was normalized to 0 for offset and 1 for cellular background. (c) Recruitment into NB micropatterns is determined as the contrast of the fluorescence signal inside and outside the patterns. Each dot in the boxplot represents a cell. (d) Scheme illustrating the immobilization into micropatterns.

Plotting the fluorescence intensity of all channels across the rectangular ROI illustrates the difference in protein accumulation inside the micropatterns, with the fluorescence intensity of the STAT2 fluorescence signal only ranging between a contrast of 1-1.5 (**Figure 24b**). For statistical analysis, contrast values of whole cells were evaluated (**chapter 3.4.20**), with mEGFP-ISG15 exhibiting a high contrast of 7.8 ± 3.0 ($n = 26$) and USP18-mCherry of 8.3 ± 4.4 ($n = 26$), being comparable to the *in vivo* control experiment of cytosolic GFP, thus confirming their specific capturing as bait and prey, respectively (**Figure 24c**). In comparison, fSNAP-STAT2 depicted a very low contrast of 1.9 ± 0.5 ($n = 26$), illustrating its apparent inability to interact with ISG15-bound USP18 inside the micropatterns and revealing a competition between ISG15 and STAT2 for binding USP18. Taking advantage of the versatility of the anti-GFP NB-based pull-down, another experiment was easily carried out in vice versa orientation, utilizing mEGFP-STAT2 as bait in order to validate the previous result. HeLa cells transiently expressing HaloTag-mTagBFP-TMD-NB, mEGFP-STAT2, USP18-mCherry and fSNAP-ISG15, were seeded on PLL-PEG-HTL micropatterned coverslides (**Figure 25**) and labeled with BG-SiR.

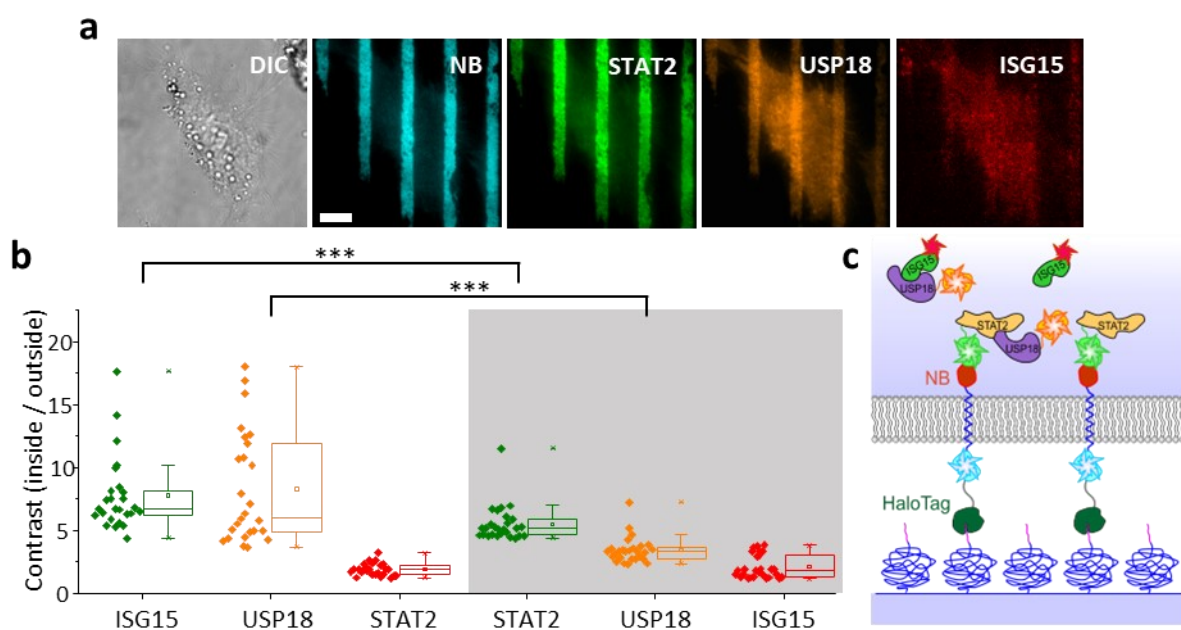


Figure 25: Recruitment to STAT2 prevents USP18 interaction with ISG15. (a) DIC and fluorescence images of HeLa cells transiently expressing HaloTag-mTagBFP-TMD-NB (blue channel), mEGFP-STAT2 (green channel), USP18-mCherry (orange channel) and fSNAP-ISG15 labeled with BG-SiR (red channel). Scale is 10 μm . (b) Recruitment into NB micropatterns is determined as the contrast of the fluorescence signal inside and outside the patterns. First 3 boxplots from the previous pull-down experiment. Each dot in the boxplot represents a cell. (c) Scheme illustrating the immobilization into micropatterns.

Likewise, TIRFM then revealed specific capturing of mEGFP-STAT2 as bait into NB micropatterns, while less specifically co-capturing USP18-mCherry as prey, which showed a distinct background of cytosolic proteins (**Figure 25a**). Again, the remaining cytosolic interaction partner of USP18, in this case fSNAP-ISG15, showed no binding inside the micropattern. These findings were also supported by a statistical analysis of a multitude of cells, with mEGFP-STAT2 yielding a contrast of 5.5 ± 1.4 ($n = 27$) as bait, and USP18-mCherry yielding a lowered contrast of only 3.4 ± 1.0 ($n = 27$), whereas fSNAP-ISG15 gave a contrast of only 2.1 ± 0.9 ($n = 27$) (**Figure 25b**). Comparing these results to the previous experiment revealed significant differences for the bait proteins (mEGFP-ISG15/STAT2 $p = 0.0009$) and for USP18-mCherry ($p = 0.000001$), but no meaningful significance for the second prey protein (fSNAP-STAT2/ISG15 $p = 0.4$) (**Figure 25b**).

This lowered contrast of mEGFP-STAT2 was likely caused by overexpression, which can lead to a saturation of available nanobody binding sites in the micropattern. In such a case, more fluorescent proteins remain in the cytosolic background, thus reducing the observable fluorescence contrast. Similarly, the significantly reduced contrast of USP18-mCherry can be attributed to the visibly high background of cytosolic proteins, which may either bind cytosolic mEGFP-STAT2, or cytosolic fSNAP-ISG15. Importantly, the absence of fSNAP-ISG15 in the micropattern validates the previous result, confirming the competition between ISG15 and STAT2 for binding USP18.

These results demonstrate the competition between STAT2 and ISG15 as unbiased as possible, by performing separate pull-downs in vice versa orientations, utilizing both interaction partners as bait. Seeking further validation for the anti-GFP NB pull-down assay, the next logical step was to compare these results to a pull-down assay where one of the interaction partners is directly immobilized and micropatterned at the plasma membrane, a methodology with which we acquired a lot of experience in the past.

4.2.5 Directly immobilizing STAT2 as bait for live cell micropatterning

As stated, the next step was to compare the anti-GFP NB pull-down to a pull-down assay utilizing STAT2 fused to a transmembrane domain and the HaloTag, thus omitting the NB-GFP interaction in the pull-down architecture. Replacing the NB with STAT2, HeLa cells transiently expressing HaloTag-mTagBFP-TMD-STAT2, USP18-mEGFP and fSNAP-ISG15 were seeded overnight on PLL-PEG-HTL micropatterned coverslides, labeled with BG-SiR and observed via TIRFM imaging (**Figure 26**).

In contrast to the previous experiments, only the immobilized bait protein STAT2 was clearly micropatterned (**Figure 26a**, top), whereas the prey proteins USP18 and ISG15 exhibited low non-specific contrast values of 1.6 ± 0.4 ($n = 9$) and 1.2 ± 0.2 ($n = 9$), respectively (**Figure 26b**, left). These results show that USP18 and ISG15 were mostly present within a cytosolic fraction, as USP18 was not exclusively co-localized within the STAT2 micropattern. Again, this result confirmed the competition between ISG15 and STAT2 for USP18 and thus the validity of the NB pull-down assay.

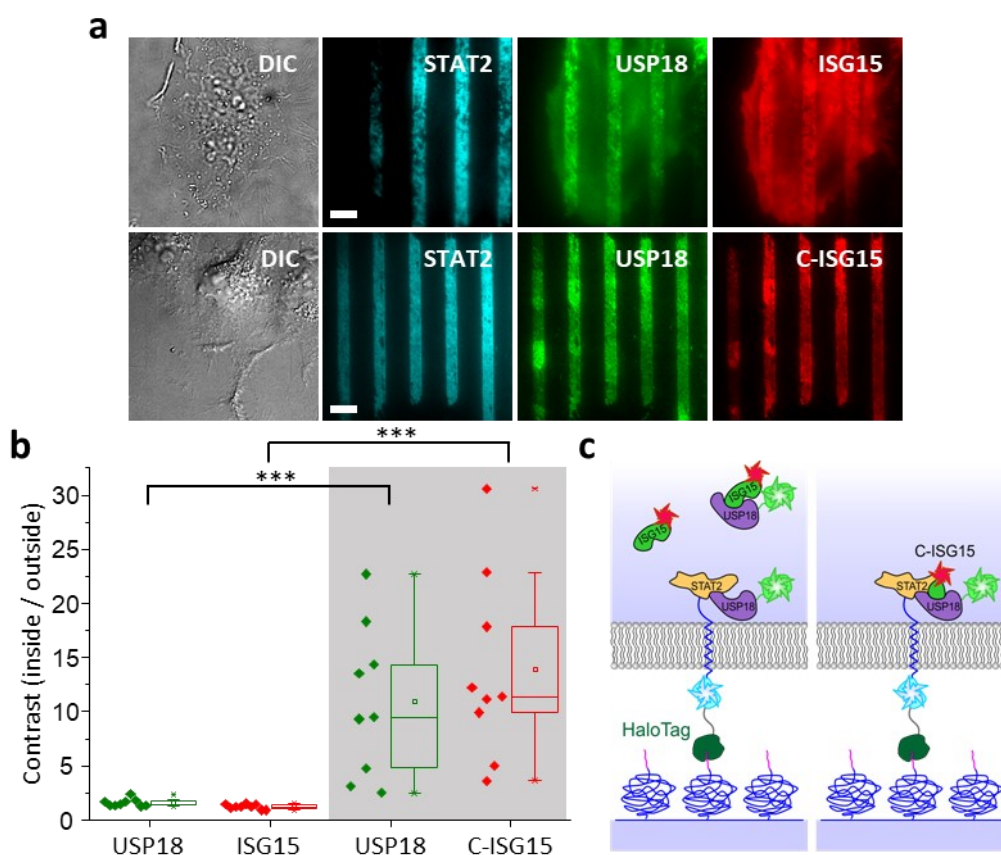


Figure 26: C-terminal ISG15 interacts with STAT2-bound USP18. (a) DIC and fluorescence images of HeLa cells transiently expressing HaloTag-mTagBFP-TMD-STAT2 (blue channel), USP18-mEGFP (green channel) and fSNAP-ISG15 labeled with BG-SiR (red channel). ISG15 was transfected as full-length ISG15 (top lane), or C-terminal ISG15 domain (bottom lane). Scale is 10 μ m. (b) Recruitment into STAT2 micropatterns is determined as the contrast of the fluorescence signal inside and outside the patterns. Each dot in the boxplot represents a cell. (c) Scheme illustrating the immobilization into micropatterns.

As previously published [109] and demonstrated in the previous experiments (**chapter 4.2.2**), it was clear that only the C-terminal ISG15 domain is interacting with USP18, whereas the N-terminal domain of ISG15 is seemingly not involved in the interaction. By again utilizing truncations of ISG15, it was feasible to investigate whether the competition between STAT2 and C-terminal ISG15 for USP18 would also occur, therefore gaining more mechanistic insights on the nature of the observed competition.

Thus, HeLa cells transiently expressing HaloTag-mTagBFP-TMD-STAT2, USP18-mEGFP and truncated fSNAP-C-ISG15 were seeded overnight on PLL-PEG-HTL micropatterned surfaces, labeled with BG-SiR and observed via TIRFM. Here, both prey proteins were clearly captured into micropatterns (**Figure 26a**, bottom), with USP18-mEGFP exhibiting a high contrast of 10.9 ± 6.9 ($n = 9$) and fSNAP-C-ISG15 an even higher contrast of 13.9 ± 8.6 ($n = 9$), both being significantly higher than when utilizing full-length ISG15 (**Figure 26b**, right).

These findings lead to the conclusion that the observed competition between STAT2 and ISG15 for USP18 is likely attributed to steric hindrance induced by full-length ISG15, which is abolished when utilizing only the C-terminal ISG15 domain. Moreover, an overlapping binding site on USP18 for STAT2 and ISG15 could be excluded, as binding, but not competition, is perceived when using the C-terminal ISG15 domain.

4.2.6 Excluding direct interactions between STAT2 and ISG15

Due to the finding that competition between STAT2 and C-terminal ISG15 for USP18 was seemingly abolished, it became mandatory to verify that STAT2 is unable to directly interact with either full-length or C-terminal ISG15, which would also lead to the observation of STAT2 and C-ISG15 localizing in the same micropattern. To demonstrate this negative control as clear as possible, directly immobilized STAT2 was again utilized, avoiding the expression of a third construct such as the anti-GFP NB. To this end, another pull-down experiment with immobilized STAT2 was performed, utilizing both full-length, as well as C-terminal ISG15. HeLa cells transiently expressing HaloTag-BFP-TMD-STAT2 and either fSNAP-ISG15 or fSNAP-C-ISG15 were seeded on PLL-PEG-HTL micropatterned coverslips, labeled with BG-SiR and observed via TIRFM (**Figure 27**).

In both experiments, only immobilized STAT2 exhibited a clear micropattern, whereas both full-length and C-terminal ISG15 were visibly unable to interact with STAT2. This is further supported by statistical analysis, which revealed an fSNAP-ISG15 fluorescence

contrast of just 1.2 ± 0.1 ($n = 20$) and for fSNAP-C-ISG15 a similarly low contrast of 1.2 ± 0.1 ($n = 20$), indicating no direct interaction between ISG15 and STAT2. These results prove that the truncation of ISG15 did not lead to a gain-of-function of being able to bind STAT2 directly, but rather that C-terminal ISG15 truly abolished the competition between ISG15 and STAT2 for USP18 in the previous experiments, most likely due to lack of steric hindrance when truncating the N-terminal ISG15 domain.

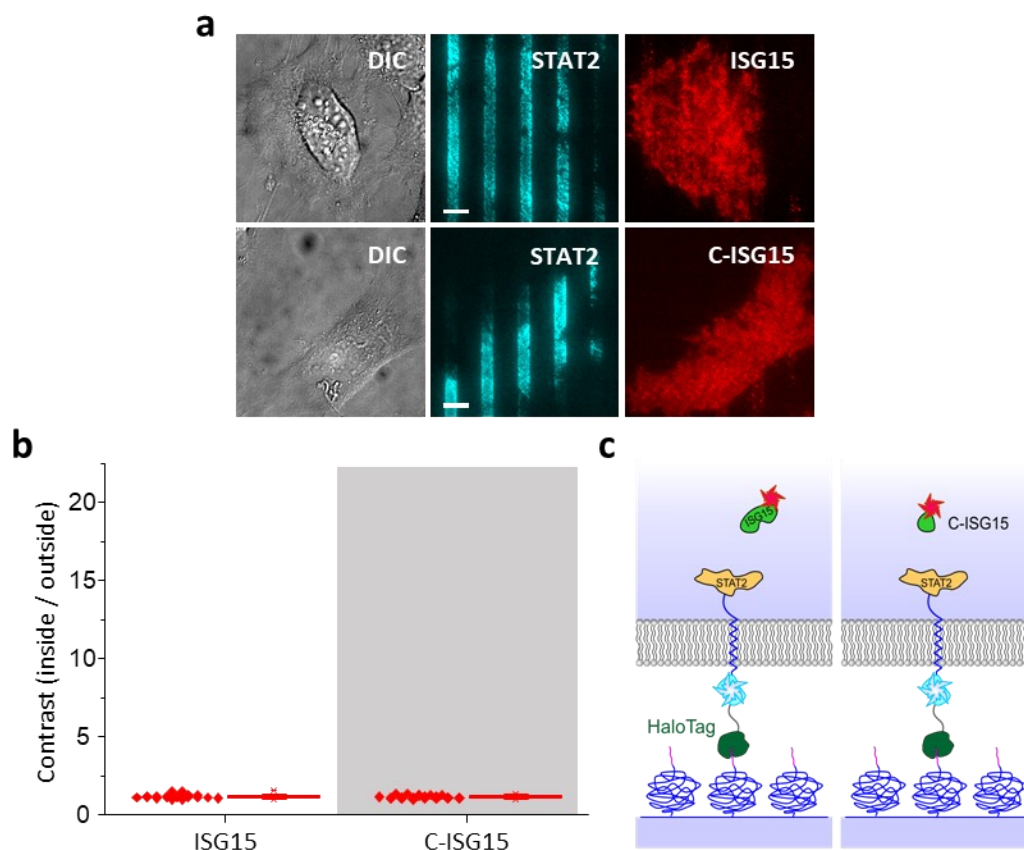


Figure 27: ISG15 does not interact with STAT2. (a) DIC and fluorescence images of HeLa cells transiently expressing HaloTag-mTagBFP-TMD-STAT2 (blue channel) and fSNAP-ISG15 labeled with BG-SiR (red channel). ISG15 was either transfected as full-length ISG15 (top lane), or C-terminal ISG15 domain (bottom lane). Scale is 10 μ m. (b) Recruitment into STAT2 micropatterns is determined as the contrast of the fluorescence signal inside and outside the patterns. Each dot in the boxplot represents a cell. (c) Scheme illustrating the immobilization into micropatterns.

4.2.7 Investigating competition at the interferon receptor

While the NB pull-down assay enables investigation of cytosolic protein interactions, previously obtained results were also reviewed in context of the actual site of action, the interferon alpha receptor subunit 2 (IFNAR2). Here, IFNAR2 was immobilized, recruiting STAT2 as bait via its binding site, which in turn serves as an adaptor for USP18 [103], allowing to investigate co-recruitment of ISG15.

To this end, HeLa cells transiently expressing HaloTag-mTagBFP-IFNAR2, USP18-mEGFP, STAT2-tdmCherry and fSNAP-ISG15 labeled with BG-SiR were employed (**Figure 28**).

TIRFM revealed highly specific immobilization of HaloTag-mTagBFP-IFNAR2, as well as a high contrast binding of STAT2-tdmCherry as bait, which efficiently recruited USP18-mEGFP as prey (**Figure 28a, top**), exhibiting a contrast of 8.0 ± 3.2 ($n = 14$) and 7.2 ± 2.0 ($n = 14$) respectively. Only fSNAP-ISG15 was found unable to interact with the receptor-bound proteins, displaying a low contrast of 1.7 ± 0.3 ($n = 14$).

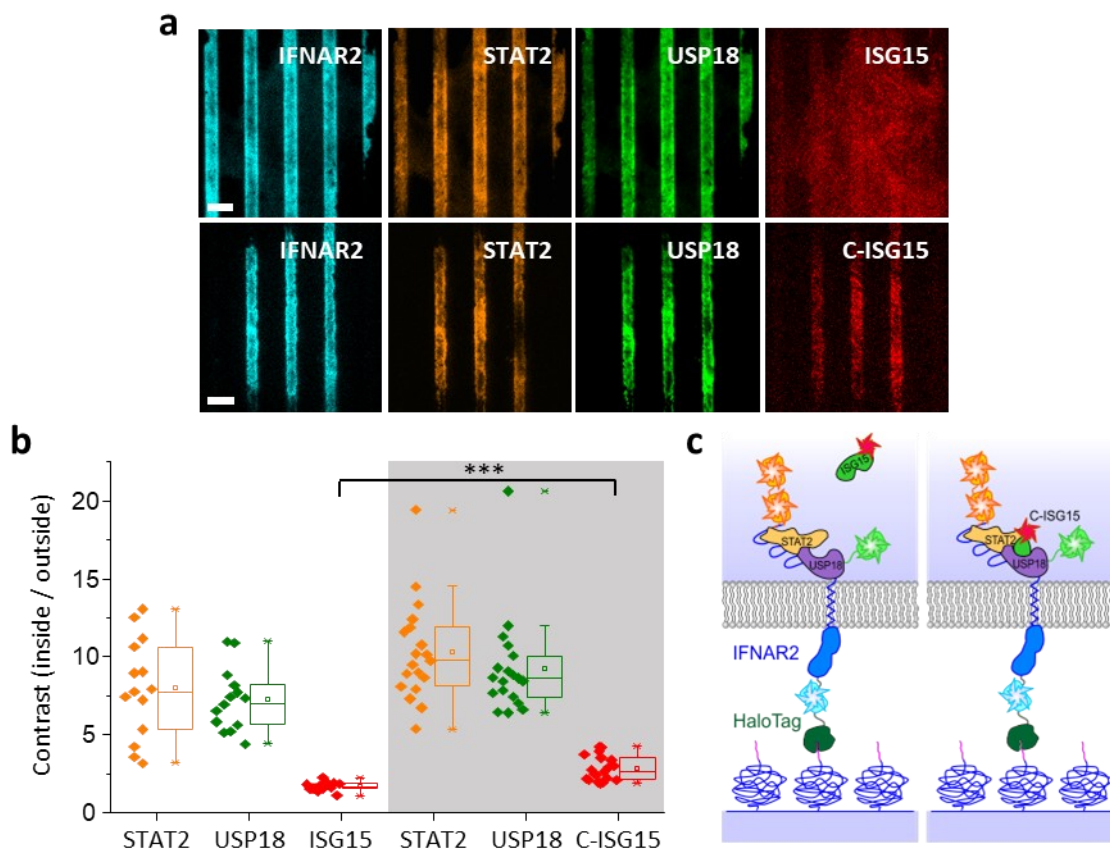


Figure 28: Competition at the cytokine signaling complex. (a) Fluorescence images of HeLa cells transiently expressing HaloTag-mTagBFP-IFNAR2 (blue channel), USP18-mEGFP (green channel), STAT2-tdmCherry (orange channel) and fSNAP-ISG15 labeled with BG-SiR (red channel). ISG15 was transfected as fulllength (top lane), or C-terminal domain (bottom lane). Scale is 10 μ m. (b) Recruitment into IFNAR2 micropatterns is determined as the contrast of the fluorescence signal inside and outside the patterns. Each dot in the boxplot represents a cell. (c) Scheme illustrating the immobilization into micropatterns.

Additionally, a similar experiment using fSNAP-C-ISG15 was performed, investigating the C-terminal domain of ISG15 in context of IFNAR2 binding (**Figure 28a, bottom**). Like the previous experiments, IFNAR2 efficiently bound STAT2-tdmCherry as bait, while both USP18-mEGFP and fSNAP-C-ISG15 could be specifically recruited into the micropattern, displaying a contrast of 10.3 ± 3.2 ($n = 19$), 9.2 ± 3.2 ($n = 19$) and 2.8 ± 0.8 ($n = 19$), respectively. In comparison, fSNAP-C-ISG15 displayed a significantly higher contrast than full-length fSNAP-ISG15 (**Figure 28b**). These results are therefore in good agreement with the previous findings, confirming the competition between STAT2 and ISG15 at IFNAR2, while also observing the abolished competition when utilizing the C-terminal ISG15 domain, in turn confirming the validity of the NB pull-down assay.

4.2.8 N-terminus of USP18 is required for STAT2 binding

Having demonstrated that the unstructured N-terminal region of USP18 is crucial for binding its interaction partner ISG15, and having concluded that ISG15 and STAT2 are binding competitively towards USP18, it stands to reason that the N-terminus of USP18 might also affect STAT2 binding. Consequentially, the effect of the N-terminal USP18 truncation was investigated for interaction with STAT2. Like the previous experiments, HeLa cells transiently expressing HaloTag-mTagBFP-TMD-NB and either USP18-mEGFP, or USP18 Δ 42N-mEGFP, as well as STAT2-tdmCherry were seeded overnight on micropatterned coverslides and observed via TIRFM (**Figure 29a**).

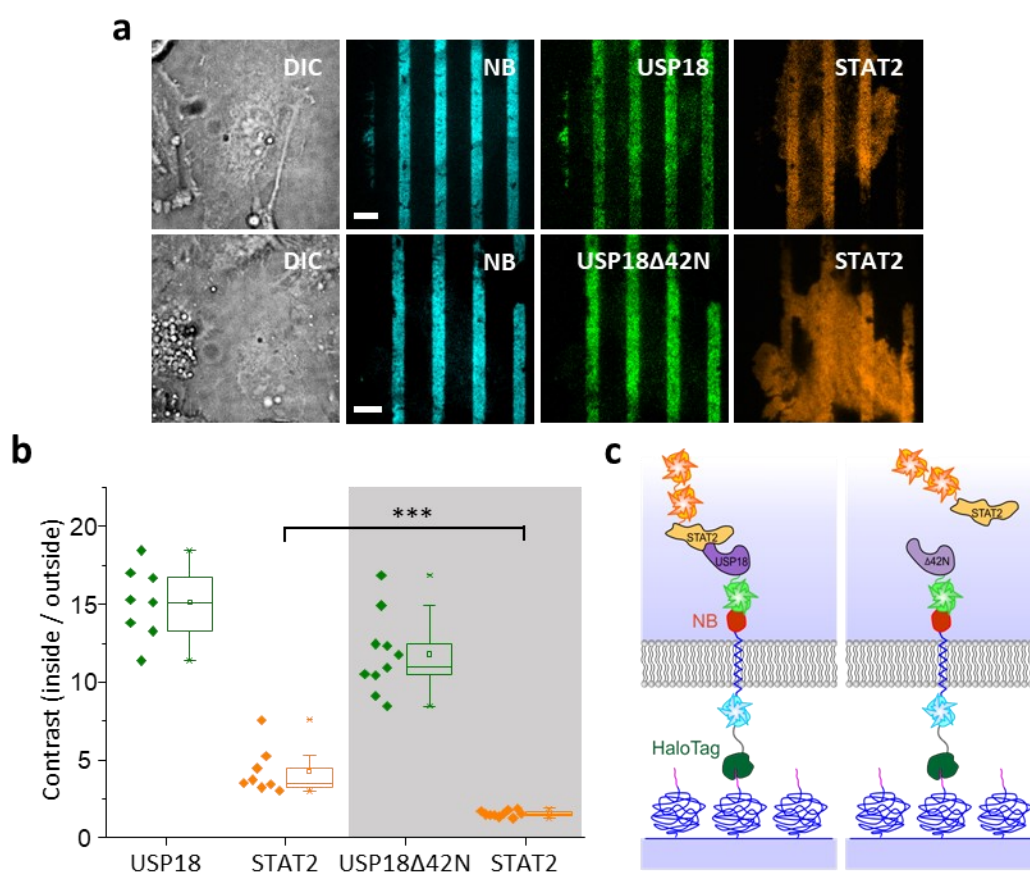


Figure 29: N-terminus of USP18 required for STAT2 binding. (a) DIC and fluorescence images of HeLa cells transiently expressing HaloTag-mTagBFP-TMD-NB (blue channel), USP18-mEGFP (green channel) and STAT2-tdmCherry (orange channel). USP18 was transfected as fulllength (top lane), or N-terminal truncation of Aminoacids 1-42 (USP18 Δ 42N, bottom lane). Scale is 10 μ m. (b) Recruitment into NB micropatterns is determined as the contrast of the fluorescence signal inside and outside the patterns. Each dot in the boxplot represents a cell. (c) Scheme illustrating the immobilization into micropatterns.

In both experiments, USP18-mEGFP and USP18 Δ 42N-mEGFP exhibited a clear micropattern, with contrasts of 15.1 ± 2.3 ($n = 8$) and 11.8 ± 2.5 ($n = 10$) respectively, confirming efficient capturing of bait proteins. However only full-length USP18 was able to capture STAT2-tdmCherry with a contrast of 4.3 ± 1.5 ($n = 8$), whereas USP18 Δ 42N

did not interact with STAT2-tdmCherry, as depicted by a contrast of merely 1.6 ± 0.2 ($n = 10$) (**Figure 29b**). In conclusion, both full-length ISG15, C-terminal ISG15 and STAT2 are thus affected by truncating the unstructured N-terminal region of USP18, despite C-terminal ISG15 and STAT2 not sharing an overlapping binding site. The unstructured N-terminus of USP18 therefore remains enigmatic, demanding additional, future investigation.

4.2.9 Split two-hybrid nanobody live cell micropatterning

Attempting to further enhance the NB live cell micropatterning assay, bimolecular fluorescence complementation (BiFC) was implemented. Similar to common BiFC assays, the N- and C-terminal domains of split mEGFP (NmEGFP, CmEGFP) were fused to proteins of interest, leading to induced complementation of the unfolded split mEGFP upon specific protein-protein interaction. This offers two distinct advantages in combination with an anti-GFP NB pull-down: First, complementation leads to fluorophore maturation, therefore only complemented mEGFP can be observed. Second, only complemented mEGFP can be specifically captured via the anti-GFP NB, omitting non-interacting proteins from the pull-down assay.

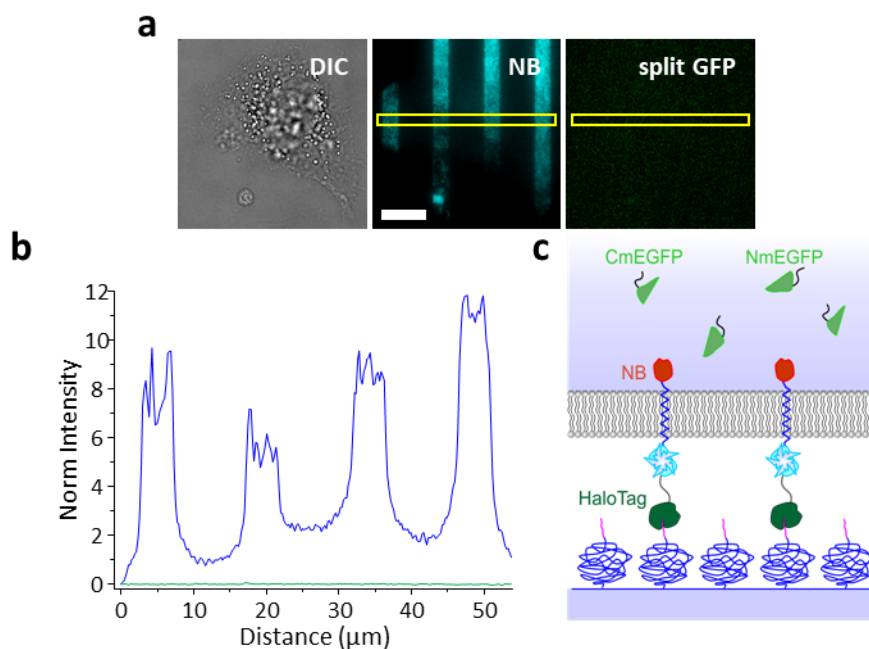


Figure 30 BiFC is not induced by the anti-GFP NB enhancer. (a) DIC and fluorescence images of HeLa cells transiently expressing HaloTag-mTagBFP-TMD-NB (blue channel), NmEGFP and CmEGFP (split GFP domains, each nonfluorescent). Complementation of split GFP would lead to fluorescence maturation and specific capturing into NB patterns (green channel). Scale is 10 μm . (b) Line profile of the fluorescence intensity in each channel, plotted against the axial distance of the ROI. Fluorescence intensity was normalized to 0 for offset and 1 for cellular background. (c) Scheme illustrating the expressed NB construct and split mEGFP proteins.

However, since complementation is induced via protein interactions, an important negative control was to verify the inability of the NB to bind and induce complementation of the unfolded split mEGFP domains. This was demonstrated by HeLa cells transiently expressing HaloTag-mTagBFP-TMD-NB and both NmEGFP and CmEGFP, which were seeded overnight on micropatterned coverslides and observed via TIRFM, resulting in no observable fluorescence contrast in the mEGFP channel (**Figure 30**).

As a proof-of-concept experiment, the USP18-ISG15 interaction was employed as a known model system, in order to demonstrate a NB pull-down of a complemented protein complex. HeLa cells transiently expressing HaloTag-mTagBFP-TMD-NB, USP18-NmEGFP and CmEGFP-ISG15 were again seeded on micropatterned coverslides and observed after overnight incubation (**Figure 31**). TIRFM revealed a specific, high contrast binding of the complemented USP18-mEGFP-ISG15 complex, featuring a contrast of 7.3 ± 1.5 ($n = 17$) inside the micropattern.

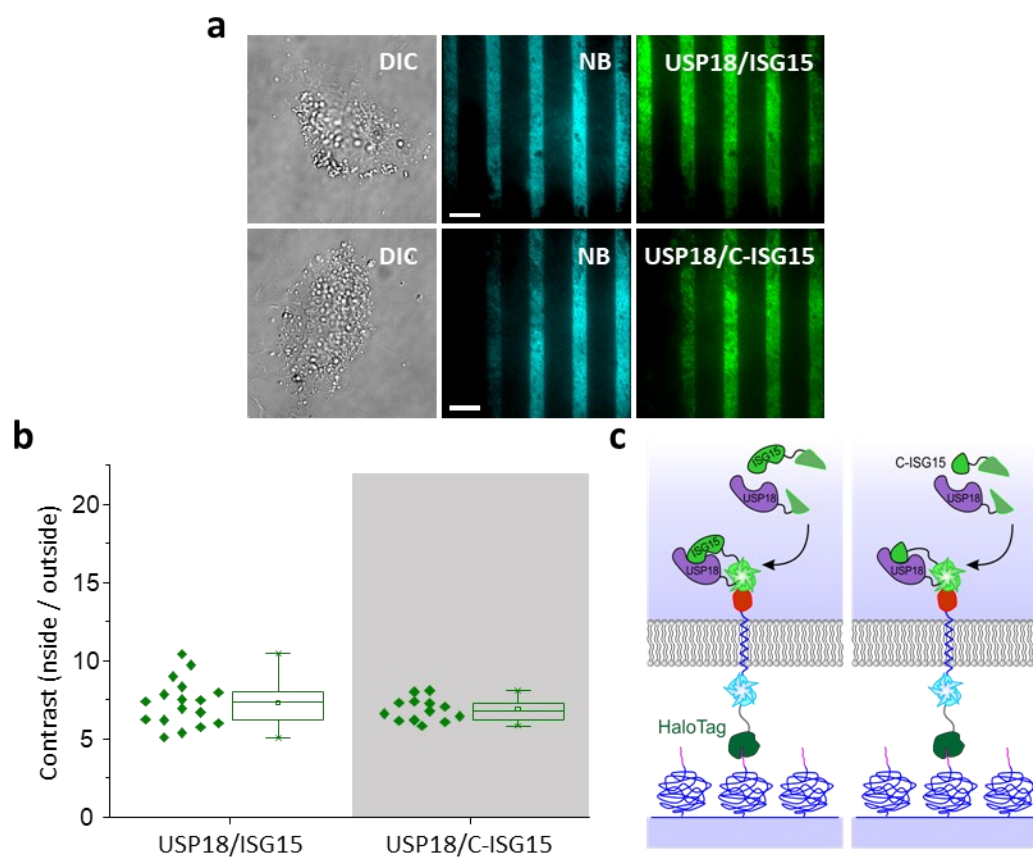


Figure 31: Specific capturing of complemented USP18-mEGFP-ISG15. (a) DIC and fluorescence images of HeLa cells transiently expressing HaloTag-mTagBFP-TMD-NB (blue channel), USP18-NmEGFP and CmEGFP-ISG15 (split GFP domains, each nonfluorescent). Complementation of split GFP leads to fluorescence maturation and specific capturing into NB patterns (green channel). ISG15 was transfected as full-length (top lane), or C-terminal domain (bottom lane). Scale is 10 μm . (b) Recruitment into NB micropatterns is determined as the contrast of the fluorescence signal inside and outside the patterns. Each dot in the boxplot represents a cell. (c) Scheme illustrating the immobilization into micropatterns.

Additionally, the same experiment was performed with C-terminal ISG15 instead of full-length ISG15. Here, complemented USP18-mEGFP-C-ISG15 was also displaying a high contrast binding of 6.9 ± 0.7 ($n = 13$), with both experiments being in good agreement with each other (**Figure 31**). These results clearly demonstrate that USP18-NmEGFP together with CmEGFP-ISG15 and CmEGFP-C-ISG15 are able to form a complemented protein complex, which can be captured in a nanobody pull-down experiment.

4.2.10 STAT2 prevents fluorescence complementation by USP18-ISG15

As stated previously, combining the anti-GFP NB pull-down with a two-hybrid assay enables visualization and capturing of specifically interacting proteins via GFP complementation. However, when simultaneously investigating multiple interacting proteins, not only the non-interacting proteins are omitted, but also proteins currently engaged in another protein interaction. This assay was therefore envisioned to selectively pull-down a specific arrangement of proteins, depending on the employed combination of split-GFP fusions. Following the previous experiments, the BiFC pull-down assay was refined offering STAT2 as an additional binding protein for USP18, while demonstrating an impaired mEGFP-complementation. To this end, HeLa cells transiently expressing HaloTag-mTagBFP-TMD-NB, USP18-NmEGFP, CmEGFP-ISG15 and STAT2-tdmCherry were seeded on micropatterned coverslides and investigated via TIRFM (**Figure 32**).

Although a distinct NB micropatterning was visible, capturing of USP18-mEGFP-ISG15 was hampered, displaying relatively low amounts of complemented, fluorescent mEGFP inside the micropatterns (**Figure 32a, top**), featuring a detectable contrast of only 3.6 ± 0.7 ($n = 11$). STAT2-tdmCherry however displayed a low contrast of 2.3 ± 0.7 ($n = 11$) featuring a visibly high cytosolic fraction. These results indicate that cytosolic STAT2-tdmCherry is interacting with USP18-NmEGFP, preventing interaction with CmEGFP-ISG15 and therefore mEGFP-complementation. In a similar manner, it was shown that cytosolic STAT2 can interact with USP18, thus preventing interaction with micropatterned ISG15 and therefore leading to a visible background of cytosolic USP18 (**chapter 4.2.4**).

Next it was analyzed whether interference of mEGFP-complementation can be abolished by employing C-terminal ISG15 instead of full-length ISG15, therefore preventing competition with STAT2. To this end, a similar experiment was carried out, using CmEGFP-C-ISG15 in combination with USP18-NmEGFP and STAT2-tdmCherry (**Figure 32a, bottom**).

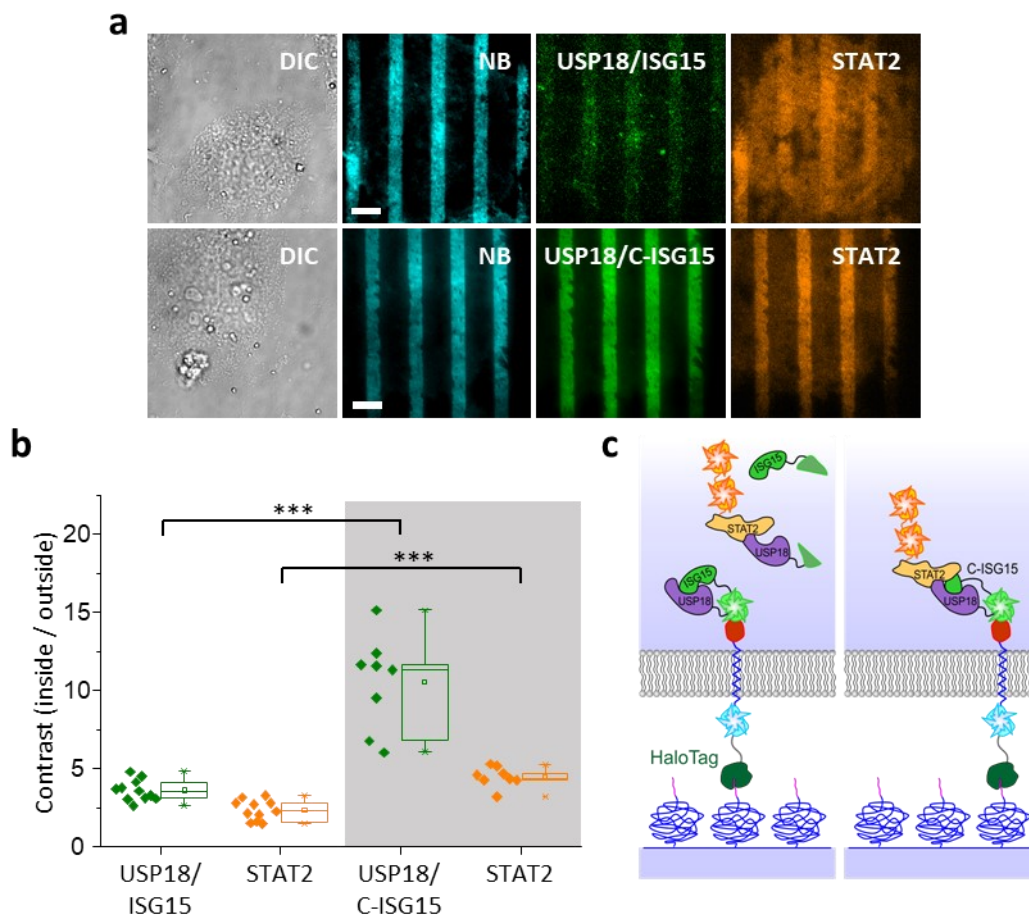


Figure 32: Competition between STAT2 and ISG15 prevents two-hybrid complementation. (a) DIC and fluorescence images of HeLa cells transiently expressing HaloTag-mTagBFP-TMD-NB (blue channel), USP18-NmEGFP and CmEGFP-ISG15 (split GFP domains, each nonfluorescent) and STAT2-tdmCherry (orange channel). Complementation of split GFP leads to fluorescence maturation and specific capturing into NB patterns (green channel). ISG15 was transfected as full-length (top lane), or C-terminal domain (bottom lane). Scale is 10 μm . (b) Recruitment into NB micropatterns is determined as the contrast of the fluorescence signal inside and outside the patterns. Each dot in the boxplot represents a cell. (c) Scheme illustrating the immobilization into micropatterns.

Here, complemented USP18-mEGFP-C-ISG15 was efficiently captured by the NB micropattern, displaying a high contrast of 10.5 ± 3.0 ($n = 8$), whereas STAT2-tdmCherry featured a distinct contrast of 4.5 ± 0.6 ($n = 8$). Both values were significantly higher than when employing full-length ISG15, confirming the loss of competition. To summarize, these model pull-down experiments illustrate the capabilities of a combined two-hybrid NB pull-down assay, which were even further adapted for single cell pull-down (SiCPull) in later experiments (**chapter 4.3.7**).

4.3 *In situ* single cell pull-down (SiCPull)

The *in situ* single cell pull-down (SiCPull) is a novel technique developed to probe affinity, kinetics, and stoichiometry of captured protein complexes. As previously published by us, purified HaloTag-NB is employed in order to functionalize PLL-PEG-HTL micropatterned coverslides, generating an anti-GFP surface micropattern [160]. Mammalian cells expressing GFP-fused proteins are grown and then directly lysed on these coverslides, exploiting their efficient protein expression while avoiding sophisticated protein purification from whole-cell lysates, offering almost instantaneous bioanalytical investigations. Enabling to investigate even very transient protein-protein interactions, SiCPull was utilized to tackle cytosolic PPIs of the type I IFN signaling pathway.

4.3.1 *In vitro* capturing of mEGFP into anti-GFP NB micropatterns

As an initial proof-of-concept experiment, *in vitro* micropatterning was carried out, demonstrating specific GFP capturing into anti-GFP NB surface micropattern. First, PLL-PEG-HTL micropatterned coverslides were incubated with 200 nM HaloTag-NB for 10 min, washed and subsequently incubated with 200 nM tagless mEGFP for 10 min (**Figure 33**). Imaging via TIRFM revealed very specific capturing of mEGFP into the anti-GFP micropattern, featuring high contrast values of ~ 7 . Yielding a contrast similar to intracellular NB micropatterning (**chapter 4.1.2**), binding to the NB functionalized micropattern remained extremely specific due to the PLL-PEG surface preventing non-specific binding (see **chapter 4.3.4, Figure 36b** for single molecule imaging). These Nanobody surfaces lay the foundation for SiCPull, enabling to capture proteins directly to the substrate via generic fluorescence tags, rather than affinity handles or antibodies.

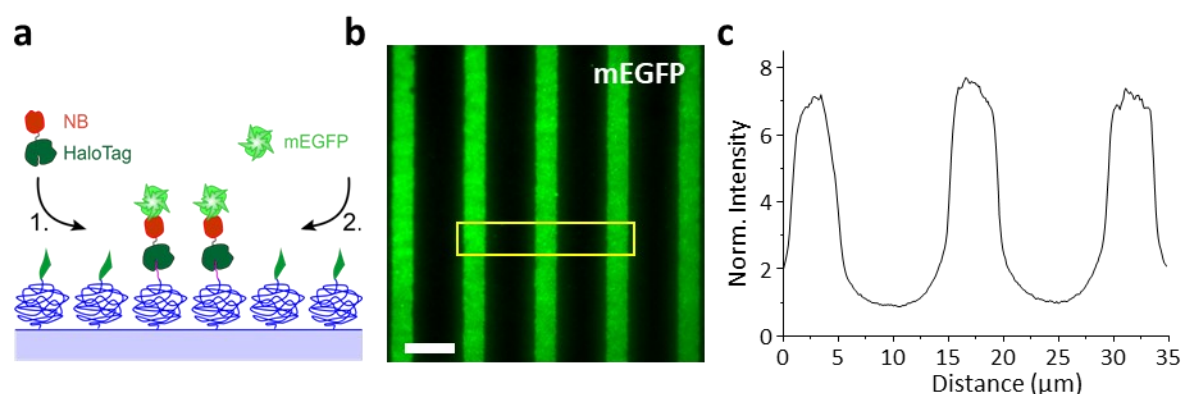


Figure 33: Efficient *in vitro* capturing of mEGFP. (a) Scheme illustrating a coverslide micropatterned with PLL-PEG-HTL and PLL-PEG-RGD. Purified HaloTag-NB is specifically binding HaloTag ligand (HTL), while the NB captures purified mEGFP. (b) TIRFM imaging of captured mEGFP. Scale is 10 μm . Yellow box indicates ROI for evaluation. (c) Line profile of the normalized fluorescence intensity plotted against the axial distance of the ROI.

4.3.2 Specific single cell pull-down

As a proof-of-concept experiment for capturing GFP-fused proteins from living cells via SiCPull, HeLa cells transiently expressing STAT1-mEGFP were grown on anti-GFP NB micropatterned coverslides and observed via TIRFM during cell lysis (**Figure 34**).

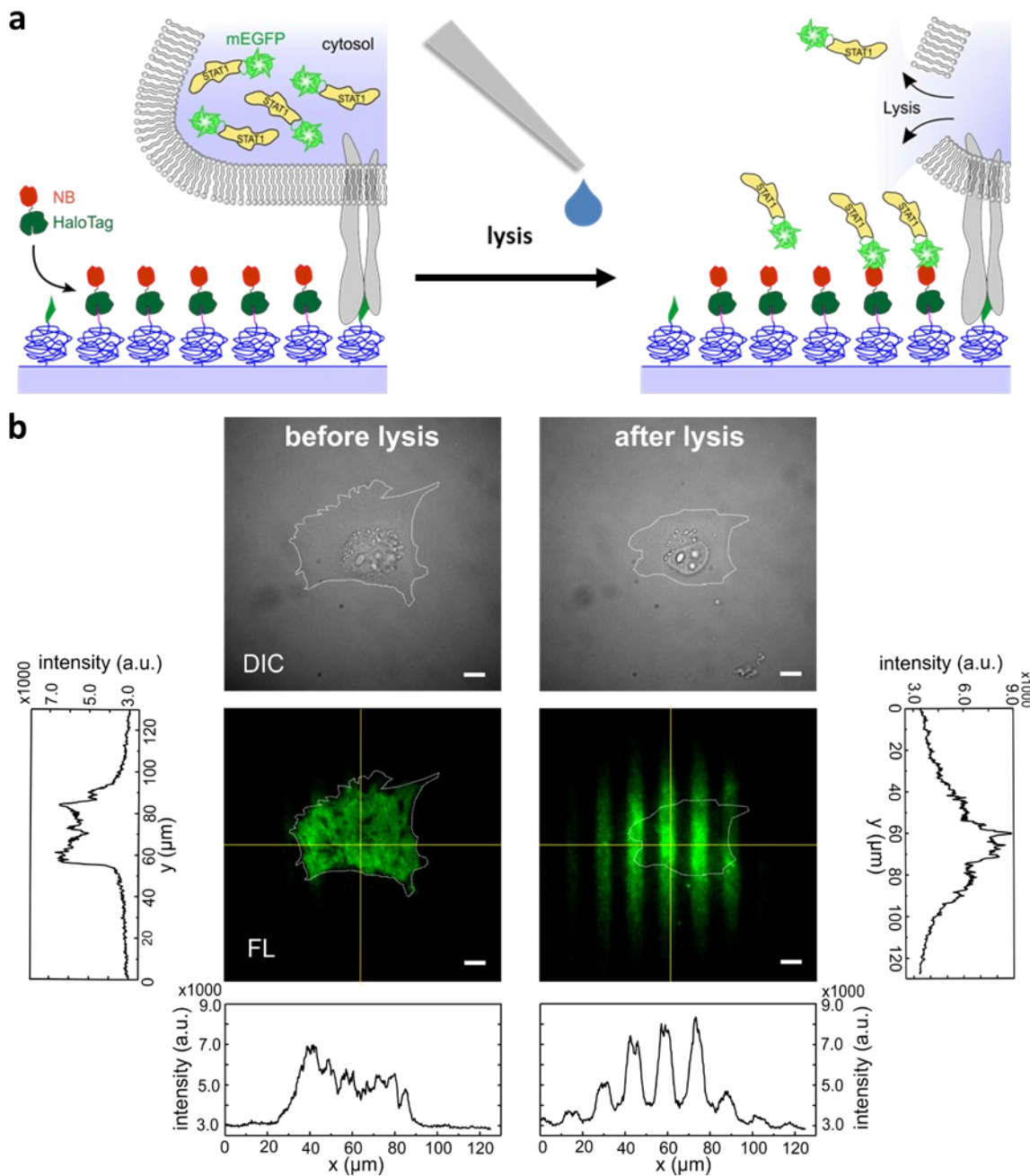


Figure 34: SiCPull strategy to capture GFP-fused STAT1. (a) HeLa cells expressing STAT1-mEGFP are grown on micropatterned coverslides functionalized with HaloTag-NB. Addition of a lysis buffer leads to cell lysis, release of cytosolic proteins and capturing into NB micropatterns. (b) DIC and TIRFM imaging of a HeLa cell expressing STAT1-mEGFP, before and after lysis. Cell shapes before and after lysis are indicated as white outlines. Fluorescence intensity is plotted against indicated yellow lines. Scale is 10 μm . Figure taken from [160], with altered outline to represent the cell shape after lysis.

Cell lysis was initiated by pipetting a lysis buffer containing a mild detergent (PBS + 0.1% Triton X-100) to the microscopy medium, which immediately lead to a visible collapse of the cell and release of STAT1-mEGFP from the cytosol into the surrounding medium (**Figure 34b**). Importantly, cellular debris and the nucleus visibly remained in the DIC image under these lysis conditions, as the lysis buffer simply induces leakage of the membrane, but not a complete dissolution of the cell. Due to the high affinity of the NB micropattern, released STAT1-mEGFP was captured *in situ*, within close proximity of just tens of micrometers distance to the host cell, demonstrating highly efficient capturing of bait proteins in a distance dependent manner from single cells. Similar to the micropatterning experiments inside living cells, this method enables specific capturing of bait proteins onto surface micropatterns, which are in turn able to co-recruit, or in this case, co-capture interacting prey proteins. Precisely this method of co-capturing was used in the following chapters, to investigate the more transient cytosolic interactions of type I IFN signaling, and even to investigate their stoichiometry on the single molecule level.

4.3.3 Investigating STAT protein interaction dynamics via SiCPull

STAT phosphorylation and subsequent dimerization are crucial processes of the type I IFN signaling pathway and cytokine signaling. And yet, interaction dynamics and stoichiometry of non-phosphorylated STATs remain to be tackled, as they have been postulated to play an important regulatory role, by dimerizing and in turn activating their own sets of target genes, while even being able to form so called statosomes [46] (see **chapter 1.3.2**). However, intracellular micropatterning investigations of PPIs are unable to resolve stoichiometry, and moreover face a crucial prerequisite which makes investigations of interaction dynamics relatively challenging. FRAP is often employed to measure the recovery of bleached proteins and therefore the dissociation constant and complex lifetime, but it requires a balanced cellular expression level of proteins, as too high background signals may bias the analysis, or even mask more transient interactions.

To this end, SiCPull was developed, which can be used to avoid any cellular background signal, independent of the expression level, thus enabling an unbiased investigation of cytosolic PPIs. In order to investigate protein interaction dynamics of unphosphorylated STATs, SiCPull experiments utilizing combinations of STAT1 as bait and either STAT1, STAT2, or STAT3 as prey, were carried out [160]. Here, HeLa cells transiently co-expressing STAT1-mEGFP as bait and STAT2-TagRFpT as prey were grown on anti-GFP NB micropatterned coverslides and SiCPull was observed via TIRFM (**Figure 35**).

Cytosolic proteins were immediately released from the cell upon addition of lysis buffer (**Figure 35a**, 0 s), instantaneously capturing STAT1-mEGFP into the anti-GFP NB micropattern as bait, while co-capturing interacting STAT2-tagRFpT as prey. Prey proteins were then dissociating over time according to their complex stability, which was observed as a decrease in the STAT2-TagRFpT fluorescence signal (**Figure 35a**). Control SiCPull experiments utilizing a fusion protein of mEGFP-TagRFpT were used to correct for photobleaching and confirmed that the observed fluorescence decay was indeed attributed to prey dissociation (**Figure 35b**). Additionally, TagRFpT and STAT-TagRFpT-fusions showed no surface binding [160] (not shown here), refuting non-specific binding and confirming the specificity of the NB towards GFP-fusion proteins.

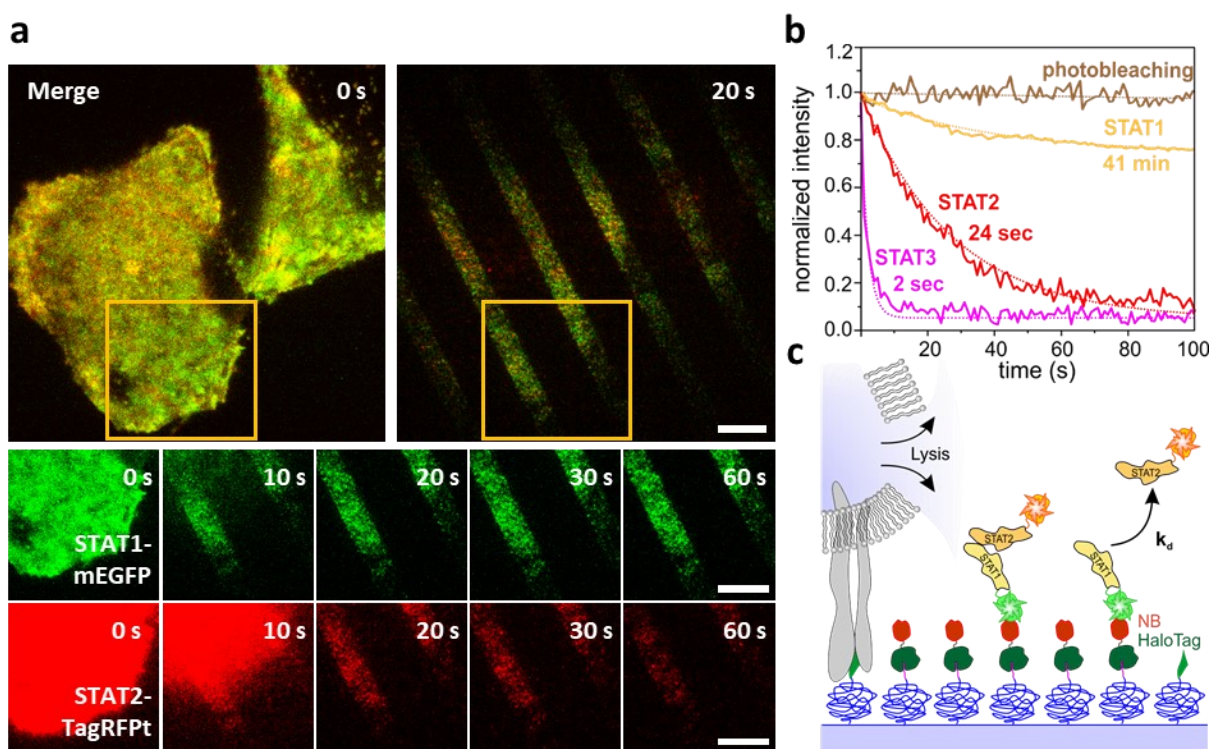


Figure 35: Probing dissociation rate constants of STAT complexes. (a) TIRFM imaging of HeLa cells transiently coexpressing STAT1-mEGFP (bait) and STAT2-TagRFpT (prey). Time points indicate time past after addition of lysis buffer. Merge image shows overlay of both fluorescence channels, yellow square indicating image crops below. Scale is 10 μm . (b) Corrected fluorescence decay of TagRFpT-fused prey proteins STAT1 (yellow), STAT2 (red) and STAT3 (magenta), co-captured via STAT1-mEGFP as bait. Photobleaching control is shown as a pull-down of a mEGFP-TagRFpT fusion protein (brown). Time point zero was set for all curves as the start of dissociation. Respective dissociation rate constants were determined via exponential fitting shown in dotted lines. Graph has been published in [160] and was altered for this work. (c) Scheme illustrating lysis of HeLa cells during SiCPull, releasing and co-capturing bait and prey proteins, with prey proteins dissociating according to their complex stability.

Exponential fitting of the corrected fluorescence decay over time was performed (**Figure 35b**, dotted line), yielding the characteristic lifetime values $\tau[\text{s}]$ as the inverse of the respective dissociation rate constants $k_d[\text{s}^{-1}]$ (**chapter 3.4.4**).

Thus, STAT1-STAT2 heterodimers yielded a complex lifetime of 24.4 ± 4.7 s and a k_d of 0.041 ± 0.008 s⁻¹, while STAT1-STAT3 heterodimers interacted much more transient and yielded a complex lifetime of only 2.1 ± 0.5 s and a k_d of 0.48 ± 0.11 s⁻¹ [160]. However, as seen in the graph (**Figure 35b**), STAT1-STAT1 homodimer dissociation followed a bi-exponential behavior, which likely indicated two distinct interactions, with the stable interaction (79.6 ± 14.7 %) giving a complex lifetime of 41 ± 7.6 min and a k_d of $(4.0 \pm 0.7) \times 10^{-4}$ s⁻¹ and the transient interaction (20.4 ± 3.7 %) giving a complex lifetime of 22.2 ± 4.1 s and a k_d of 0.045 ± 0.008 s⁻¹. These results confirm the formation of homo- and heterodimers even in absence of IFN stimulation and tyrosine phosphorylation, while quantitatively characterizing stable, as well as extremely transient PPIs of the cytosolic STATs, demonstrating the capabilities of this method.

4.3.4 Single molecule micropatterning for investigating stoichiometry

Further advancing the single cell pull-down (SiCPull), single molecule detection enables to probe the stoichiometry of individual protein complexes captured from single cells. For this single molecule single cell pull-down (SM-SiCPull), micropatterns with a sufficiently low surface density were required to avoid an analysis biased by overlapping fluorescence signals caused by diffraction limitations. This protocol has been refined since our publication [160], relying on a more sophisticated analysis and a robust, reproducible single molecule surface functionalization.

First, a mixture of 0.5% PLL-PEG-HTL and 99.5% PLL-PEG-Meo was used for microcontact printing, greatly reducing the amount of HaloTag ligand (HTL) on the substrate. Second, different mixtures of HaloTag-NB and a non-functionalized HaloTag were incubated, in order to saturate free HTL on the surface and thus to effectively control the anti-GFP NB density. A suitable density was titrated by incubating 1 μ M HaloTag-NB mixtures diluted with HaloTag for 10 min, ranging from 100%, 10%, 5%, 1%, 0.5%, down to 0.2% HaloTag-NB. Surfaces were then washed, incubated with 1 μ M tagless mEGFP for 10 min and imaged via TIRFM (**Figure 36**). Specific capturing of mEGFP was revealed for all samples, again confirming PLL-PEG surfaces preventing non-specific binding. Performing single molecule localization via SLIMfast (**chapter 3.4.6**) and the multiple-target tracing (MTT) algorithm [185] revealed high particle densities of 0.88 particles/ μ m² for 100%, 0.82 particles/ μ m² for 10% and 0.74 particles/ μ m² for 5% HaloTag-NB samples.

This saturated, non-linear scaling of surface density and incubated concentrations demonstrate the challenges of the MTT algorithm, which does not account for overlapping particles at high densities, thus over-estimating the average complex stoichiometry.

The 1% HaloTag-NB sample revealed 0.51 particles/ μm^2 , but many localized particles were visibly brighter or overlapping. Moreover, single molecule bleaching confirmed double bleaching steps for many particles when plotting the intensity over time (**Figure 36c**), confirming an inappropriate density for single molecule detection given the localization algorithm used. However, both 0.5% and 0.2% surfaces gave promising results, yielding 0.49 particles/ μm^2 and 0.32 particles/ μm^2 , respectively, with both surfaces almost exclusively yielding single bleaching events. Thus, 0.5% HaloTag-NB surfaces were chosen as standard for single molecule bleaching experiments, striking a compromise between separated particles and highest particle density for optimal statistical analysis.

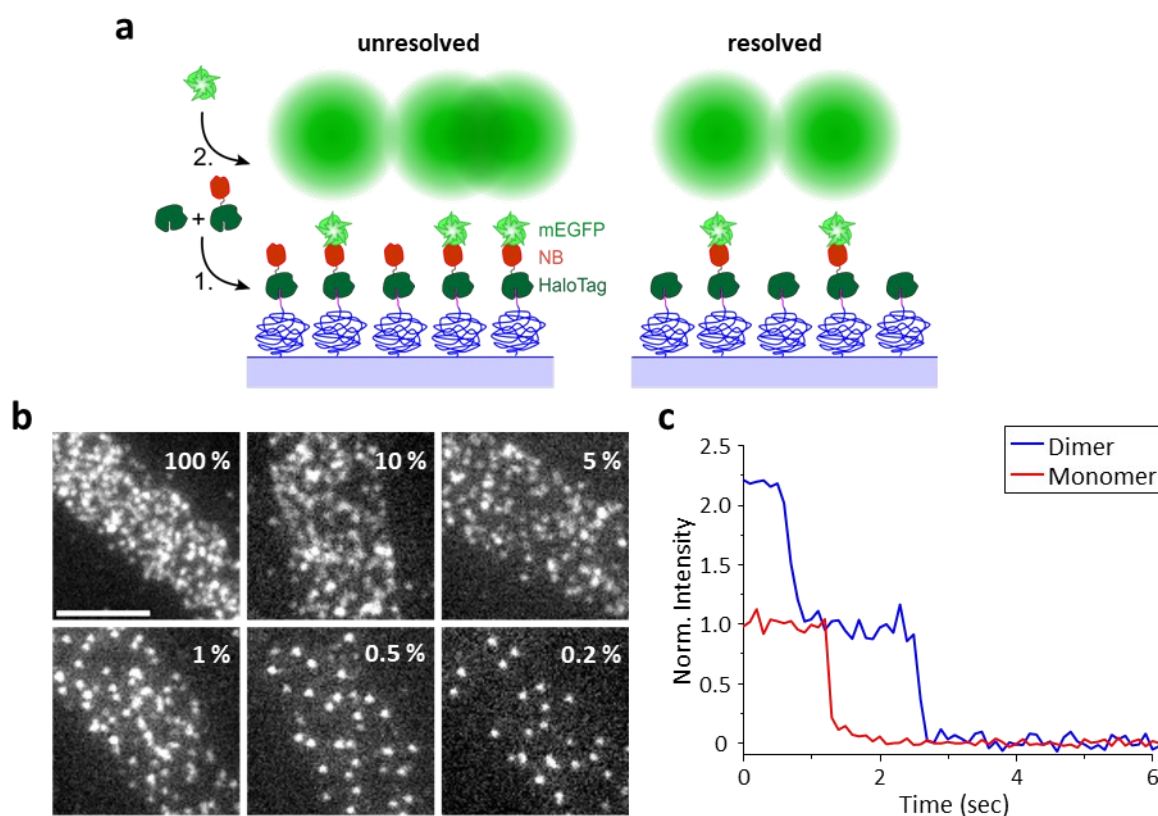


Figure 36: In vitro single molecule density titration. (a) Scheme illustrating a two-step surface functionalization with HaloTag-NB and mEGFP. Ensemble functionalized surface (left) and single molecule functionalized surface (right). Green circles represent diffraction limited signals of individual fluorophores. (b) TIRFM imaging of mEGFP captured into HaloTag-NB micropatterns with HaloTag-NB mixtures given in %. Scale is 10 μm . (c) Exemplary fluorescence over time traces depicting a single bleaching event of an individual molecule (red) and two bleaching events of overlapping and brighter molecules (blue).

4.3.5 Single molecule analysis workflow

Having achieved a single molecule micropattern suitable for detection, first control experiments were carried out, analyzing SM-SiCPull of monomeric EGFP (mEGFP), serving as a negative control for falsely detected dimers due to overlapping signals. Additionally, tandem mEGFP (tdmEGFP) was employed, serving as a positive control to define the maximum observable dimeric mEGFP signal, which is limited by stochastic maturation of the fluorophore [192]. For analysis, two Matlab software applications were employed, utilizing SLIMfast for high precision particle localization and cluster detection, subsequently using BleachCounter for bleaching step and stoichiometry analysis, as well as correction for inhomogeneous illumination bias. Demonstrating the workflow, HeLa cells transiently expressing tdmEGFP were grown on single molecule HaloTag-NB (0.5%) functionalized coverslides and SM-SiCPull was observed via TIRFM. Single molecule imaging revealed the desired density of 0.5 particles/ μm^2 for captured tdmEGFP (**Figure 37a**, left) and bleaching movies were subsequently acquired for 150 frames under different exposure times, trialing suitable conditions for subsequent analysis.

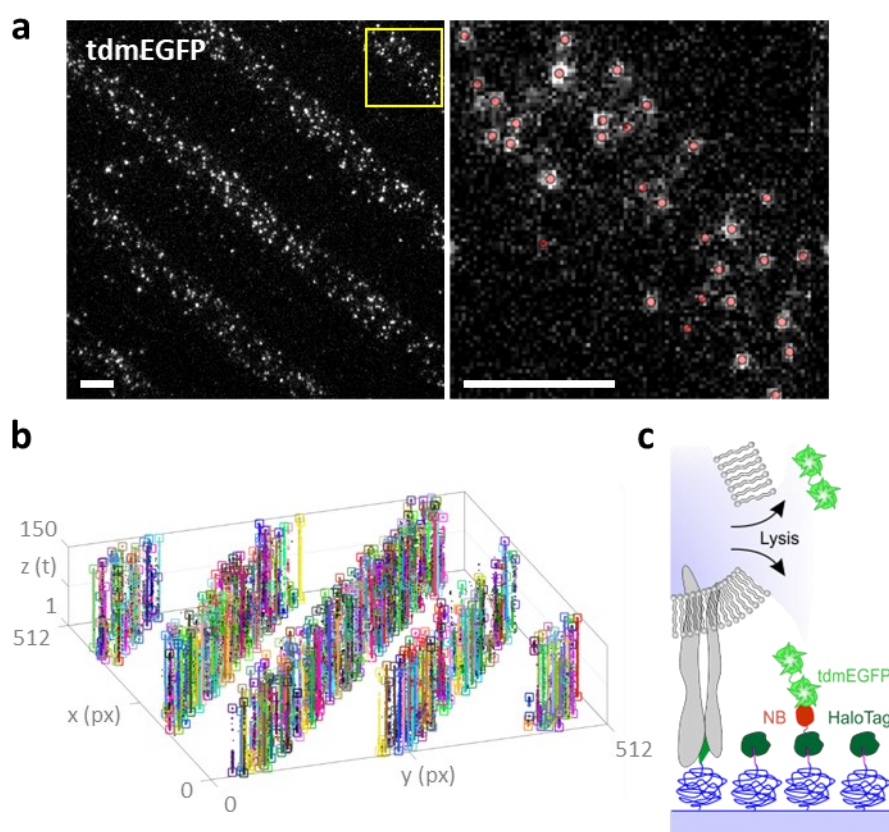


Figure 37: Localization and Cluster analysis using SLIMfast. (a) TIRFM of tdmEGFP captured into HaloTag-NB micropatterns via SM-SiCPull. Left image shows raw image, yellow box indicates the zoom in area of the right image. Right image shows localized particles as red squares. Both scales: 10 μm . (b) 3D representation of the cluster analysis. Each cluster is displayed in another colour. (c) Scheme illustrating SM-SiCPull of tdmEGFP into a HaloTag-NB micropattern.

Here, 32 ms exposure revealed typical GFP blinking behavior, leading to interrupted signals which in turn required relaxed parameters for cluster and bleaching step detection, potentially biasing the analysis. Instead, exposure time was raised to 100 ms, effectively averaging the mEGFP blinking within each frame and yielding more robust analysis results under more constrained evaluation parameters. Moreover, blinking was slightly reduced under additional 405 nm irradiation, utilizing the optically induced switching effect of UV irradiation [184]. Analysis was carried out as stated in **chapter 3.4.6**, using SLIMfast for localization within ROIs matching the micropattern, filtering out non-specific binding which occurred during cell lysis (**Figure 37a**). Next, immobile cluster detection was performed, combining localizations over multiple frames within a search radius of 80 nm into individual clusters (**Figure 37b**). For robust stoichiometry analysis, all detected clusters acquired from several videos of the same sample were pooled and exported into the BleachCounter, yielding hundreds or thousands of molecules for the analysis.

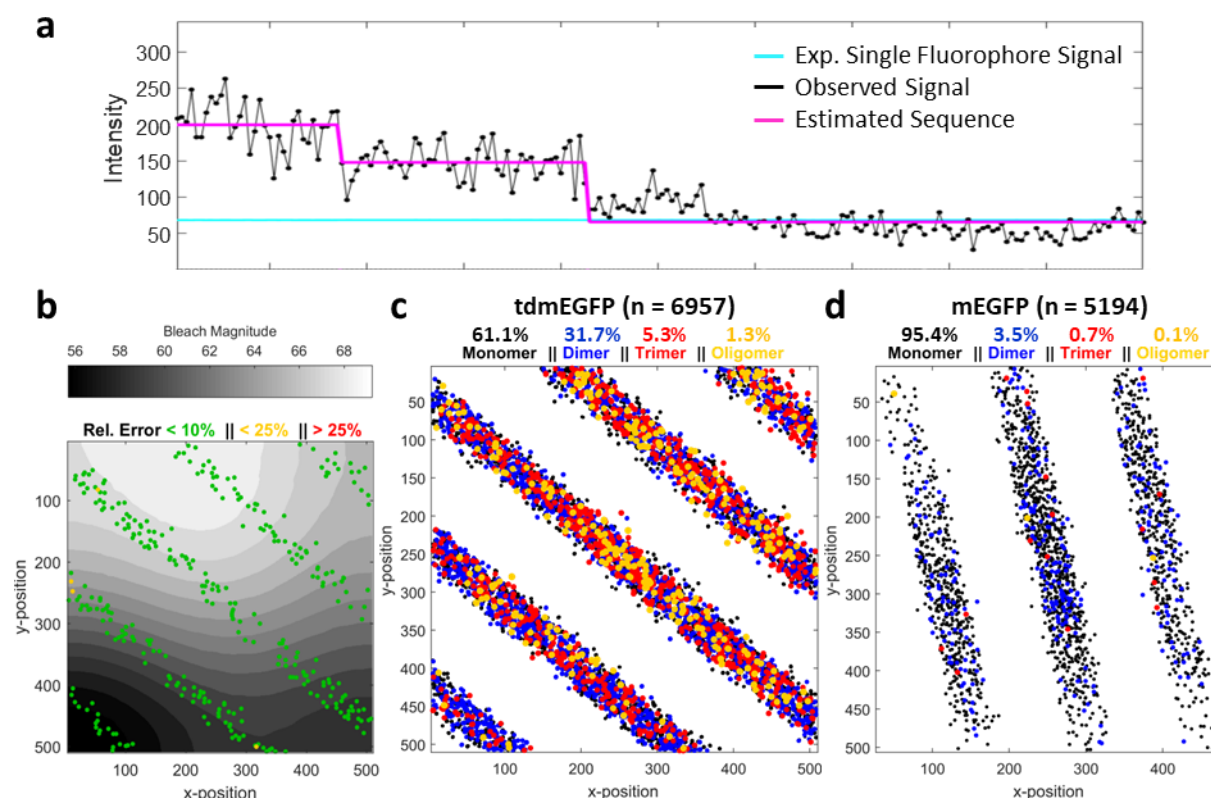


Figure 38: Single molecule analysis using the BleachCounter. (a) Fluorescence intensity trace of an individual cluster. Bleaching sequence is estimated (magenta) from the observed signal and the magnitudes are utilized to generate an illumination profile in b. Expected single fluorophore signal (cyan) is based on the illumination profile. (b) Spatial fluorophore intensity distribution map. This Illumination profile was fitted from the correlated 2D data and all detectable bleaching step magnitudes. Relative error for each bleached particle and illumination profile is shown as an internal control for profile fitting. (c-d) Molecule number maps displaying the entirety of clusters and their stoichiometry according to the illumination profile. Monomers (black), dimers (blue), trimers (red), and even higher oligomers starting from tetramers (yellow) are shown, all consecutively overlaid on top of each other.

The BleachCounter properly identified fluorescence bleaching steps from the observed fluorescence intensity over time (**Figure 38a**) and most importantly correlated all bleaching magnitudes with their 2D coordinates, generating a spatial fluorophore intensity distribution map accounting for heterogeneous sample illumination (**Figure 38b**). This map was fitted with a relative error < 10% for almost every particle to generate an illumination profile, which was used to estimate the single fluorophore signal at any given 2D coordinate in the sample and being in good agreement with the observed signal (**Figure 38a**, cyan line). The specific illumination profile of the dataset was then applied to deduce the stoichiometry of all clusters based on their 2D coordinate and fluorescence intensity as shown in the molecule number map (**Figure 38c**). Serving as a control for dimeric mEGFP signals, stoichiometry analysis of tandem mEGFP (tdmEGFP) (n = 6957) revealed 61.1% monomers, 31.7% dimers, 5.3% trimers and 1.3% oligomers, which included tetramers and above, setting the highest amount of observable mEGFP dimers to ~32%, which is achievable in this experiment due to fluorophore maturation[192]. Stoichiometries of trimers and above in turn resulted from overlapping signals of fully, or partially matured tdmEGFP. Additionally, SM-SiCPull was carried out using HeLa cells transiently expressing mEGFP as a control for monomeric capturing and false dimer detection. Here, single molecule analysis of mEGFP (n = 5194) revealed a stoichiometry of 95.4% monomers, confirming properly separated signals for 95% of particles and thus a low bias of unresolved overlapping particles, with only 3.5% dimers, 0.7% trimers and 0.1% higher oligomers being found, each corresponding to two, three or more binding sites overlapping. These results thus illustrate the maximum range of GFP signals that can be observed when examining monomeric proteins or dimeric protein interactions under these experimental conditions.

4.3.6 Stoichiometry of STATs following type I IFN stimulation

Next, intermolecular interactions between cytosolic effector proteins were investigated, utilizing STAT1 as an ideal model system featuring well characterized dimerization, and even a reported tetramerization [46, 80, 82]. Moreover, the influence of phosphorylation on STAT interaction was investigated, as dimerization in absence of phosphorylation was proposed to play a role in the transcription and regulation of gene expression [99]. However, since activated transcription factors translocate into the nucleus [51], a control experiment was carried out to investigate capturing of nuclear localized phosphorylated pSTAT1, following cell lysis. To this end, SiCPull was carried out using HeLa cells transiently transfected with STAT1-mEGFP, which were stimulated with 5 nM IFN for 20 min before cell lysis (**Figure 39**). Using the TIRF microscope in HILO mode, cell lysis was observed during addition of lysis buffer, however minutes after lysis, nuclear pSTAT1 was still retained in the nucleus, unable to be captured by the NB surface micropattern.

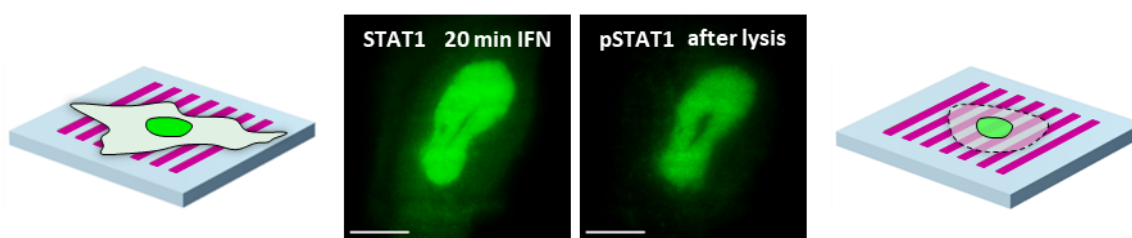


Figure 39: Inhibited capturing of nuclear proteins. HILO imaging of HeLa cells expressing STAT1-mEGFP. STAT1 was localized within the nucleus after 20 min stimulation with 5 nM IFN (left) and was still retained minutes after cell lysis (right). Scale is 10 μm .

Instead, STAT1-L407A-mEGFP was utilized as a mutant unable to bind importin- α 5 and thus to translocate into the nucleus [40], allowing to capture all STAT1-L407A molecules directly from the cytosol during SiCPull. However, nuclear translocation of phosphorylated STAT1-L407A could potentially be rescued by STAT2, requiring the use of cells deficient of wild type STAT1 and STAT2. To this end, HeLa double knockout cells (STAT1 $-/-$, STAT2 $-/-$, provided by Gideon Schreiber, Weizmann Institute, Israel) transiently expressing STAT1-L407A-mEGFP were grown on single molecule coverslides and SM-SiCPull was observed via TIRFM (**Figure 40**). Cells were either directly lysed, or first stimulated with 5 nM IFN for 20 min before addition of the lysis buffer. Both samples were fixed with 4% PFA after 30 seconds of lysis, preventing potential biases caused by dissociation of co-captured STAT1 molecules from the surface. Fixation by PFA was not necessary for the previous control experiments because they featured either monomeric GFP or a tandem GFP fusion that cannot dissociate, but fixation is a crucial step when performing pull-down experiments with freely interacting proteins.

Bleaching movies were then acquired and analysis was performed, revealing a stoichiometry of 36.9% monomers, 25.2% dimers, 14.2% trimers and 21.64% oligomers of unstimulated STAT1 ($n = 2052$) (**Figure 40a**, left). Strikingly, IFN stimulated pSTAT1 ($n = 2575$) yielded similar distributions, with 37.8% monomers, 21.7% dimers, 16.6% trimers and 20.4% oligomers (**Figure 40a**, right).

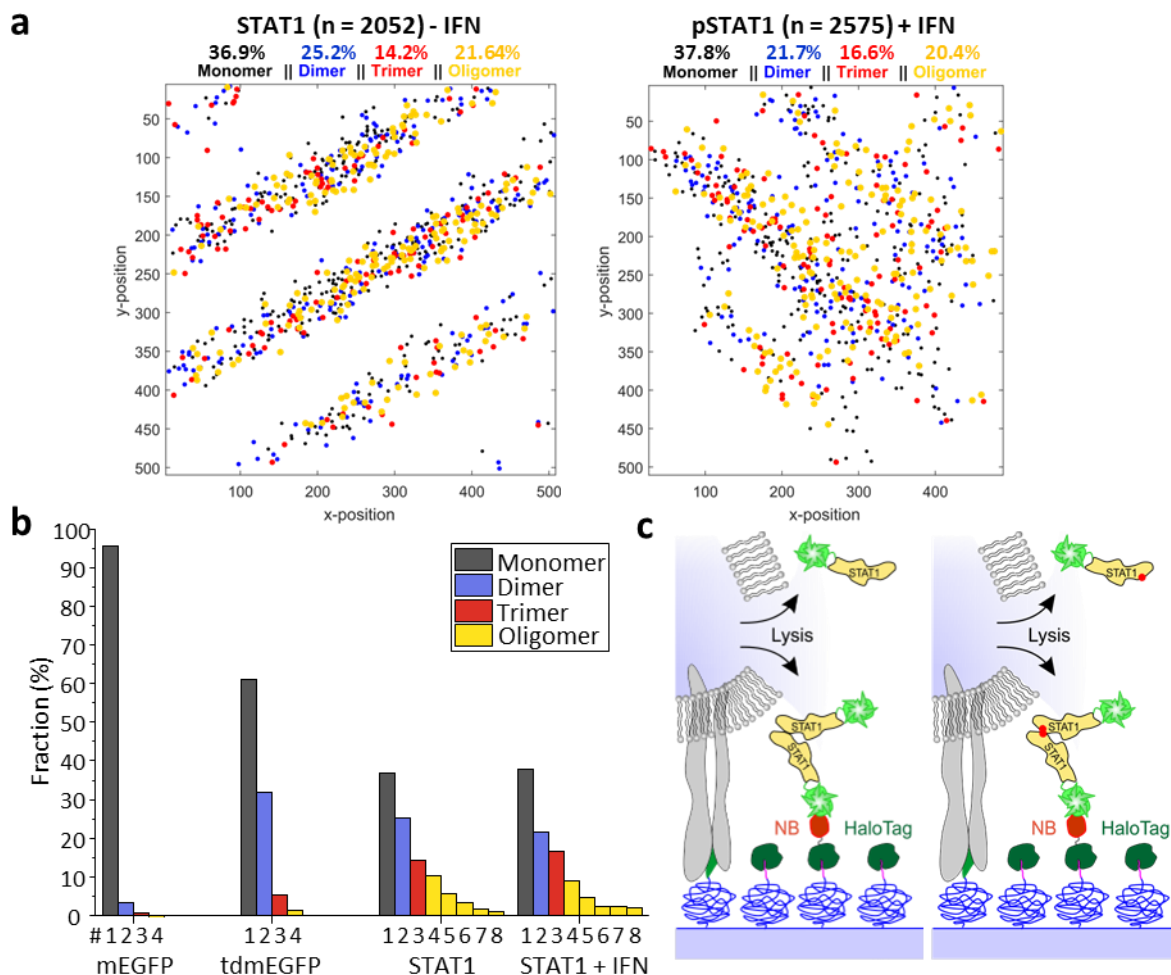


Figure 40: Single molecule analysis reveals oligomerization of STAT1. (a) Stoichiometry analysis after SM-SiCPull of HeLa double knockout cells (STAT1 $-/-$, STAT2 $-/-$) transiently expressing STAT1-L407A-mEGFP, either unstimulated (left), or IFN stimulated (right). (b) Fractions (%) of all molecule numbers in comparison to mEGFP and tdmEGFP controls. Oligomers include tetramers and above, but extremely small percentages above octamers are not shown as a separate bar. (c) Schematic illustrating SM-SiCPull of unstimulated STAT1-L407A-mEGFP (left) and IFN stimulated pSTAT1-L407A-mEGFP (right).

These results confirmed the previously reported homo-dimerization and tetramerization for both unstimulated as well as IFN stimulated and phosphorylated STAT1. Even after 20 minutes of IFN stimulation, which is known to induce a substantial phosphorylation (**Figure 39**), no difference in the equilibrium of STAT1 stoichiometry could be detected. This leads to the conclusion that surprisingly, phosphorylation does not substantially alter the stoichiometry and in turn the intermolecular interactions of STAT1.

4.3.7 Selective analysis of complemented receptor-kinase protein complexes

Finally, the influence of the oncogenic JAK2 V617F (VF) mutation was investigated via SiCPull, which is known to cause hyperactivity via unstimulated homo-dimerization of the receptor-associated kinase [20, 73, 74], making it an ideal model system for studying kinase dimerization. However, instead of solely investigating JAK2, SiCPull was employed in conjunction with BiFC, enabling to specifically investigate receptor-associated kinases. Accordingly, complementation of split GFP was again utilized to exclusively capture JAK2 interacting with the intracellular domain (ICD) of the thrombopoietin receptor (TpoR), selectively investigating the stoichiometry of only receptor associated kinases, while disregarding any individual, non-interacting proteins. Here, HeLa cells transiently expressing TpoR-ICD-NmEGFP and either JAK2 Δ TK-CmEGFP or JAK2 Δ TK-VF-CmEGFP were utilized and SM-SiCPull was carried out as in the previous experiment (**Figure 41**).

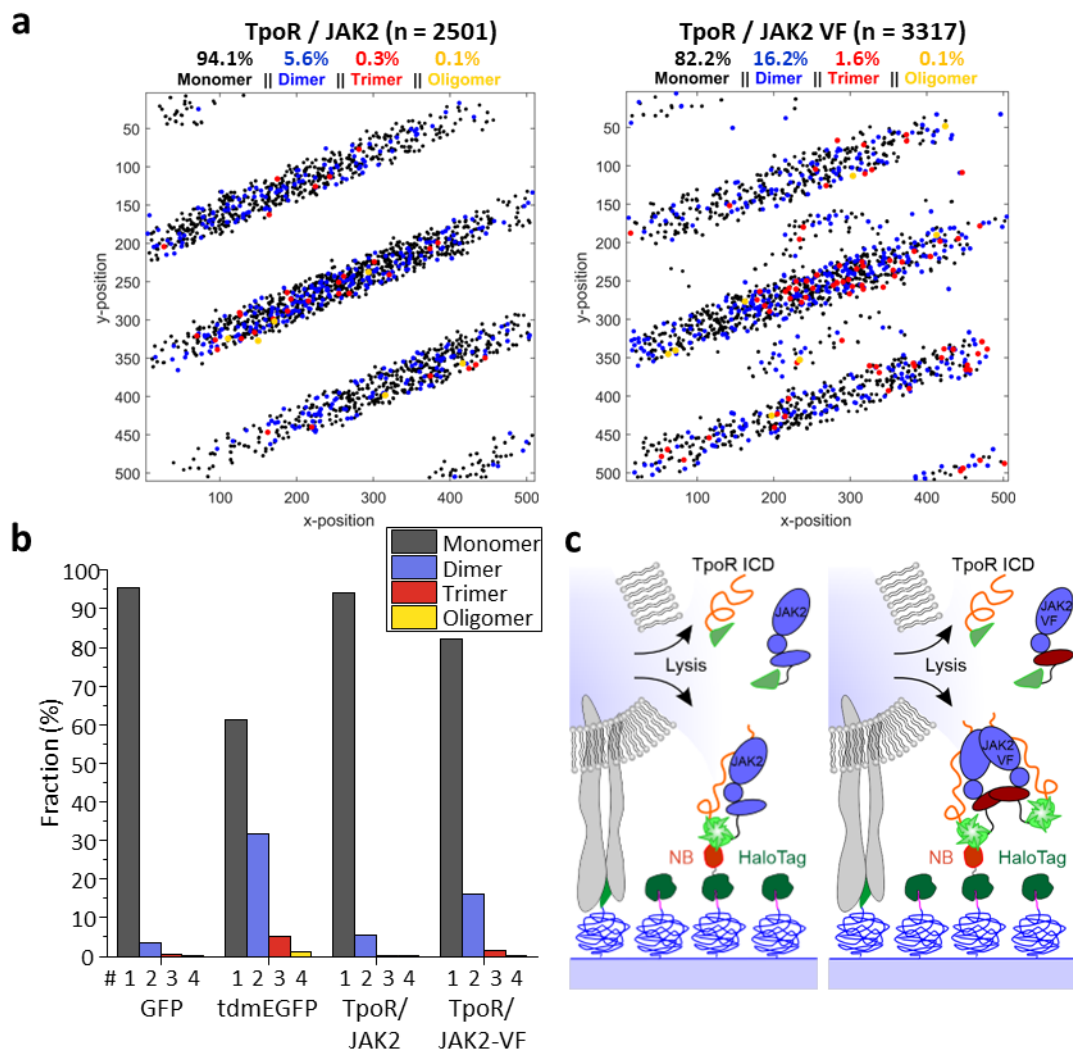


Figure 41: Specific analysis of interacting JAKs by selective capturing of complemented GFP. (a) Stoichiometry analysis after SM-SiCPull of HeLa cells transiently expressing TpoR-ICD-NmEGFP and JAK2 Δ TK-CmEGFP, either wild type (left), or the V617F (VF) mutant (right). (b) Fractions (%) of all molecule numbers in comparison to mEGFP and tdmEGFP controls. (c) Scheme illustrating SM-SiCPull of TpoR/JAK2 wild type (left) and TpoR/JAK2-VF (right).

Single molecule analysis of TpoR associated wildtype JAK2 (TpoR/JAK2) (n = 2501) revealed a stoichiometry of 94.1% monomers, 5.6% dimers, 0.3% trimers and 0.1% oligomers (**Figure 41a, b**), yielding similar results to the monomeric GFP control (**Figure 38**). In contrast, analysis of TpoR associated mutant JAK2-VF (TpoR/JAK2-VF) (n = 3317) revealed a significantly higher fraction of dimerized receptor-kinase complexes, featuring 82.2% monomers, 16.2% dimers, 1.6% trimers and 0.1% oligomers, demonstrating an enhanced dimerization caused by the JAK2 V617F mutation [20].

In conclusion, this set of experiments confirmed the significant influence of the oncogenic JAK2 V617F mutation, which was previously investigated by single molecule tracking data. This result not only demonstrated this assay's ability to reliably investigate the stoichiometry of thousands of protein complexes, in turn unraveling the influence of an altered interaction on the stoichiometric equilibrium, but it also demonstrated the ease with which BiFC can be incorporated into SM-SiCPull, as it is based on the anti-GFP NB pulldown strategy.

5 Discussion and Conclusions

In this thesis, novel live-cell and pull-down methods were developed to optimize current assays and to establish a robust and yet simplified workflow, suitable to investigate cytosolic PPIs of the type I IFN signaling pathway. This was achieved by utilizing a micropatterned anti-GFP nanobody as a generalized pull-down mechanism of GFP-tagged target proteins, based on a simple PLL-PEG surface architecture. This in turn enabled a spatio-temporal micropatterning in living cells, as well as pull-down of cytosolic proteins, captured from cells directly lysed on a coverslip. In this discussion, the biological findings are addressed in the order of this thesis, followed by the methodical aspects of nanobody live cell micropatterning and in *situ* single cell pull-down (SiCPull).

5.1 Investigating type I IFN interactions via generic nanobody live cell micropatterning

Studying the unique role of USP18 and ISG15 in type I IFN signaling, it was the very first step of this thesis to characterize their PPI by the here developed generic nanobody live cell micropatterning. This assay not only succeeded in capturing readily available mEGFP-USP18 in the cellular anti-GFP nanobody micropattern, but also demonstrated by negative controls that capturing of both USP18 as bait and ISG15 as prey was highly specific (**chapter 4.2.1**). In addition, the nanobody pull-down has been demonstrated to be well-suited to conduct fluorescence recovery after photobleaching (FRAP) experiments. As shown, FRAP revealed a surprisingly stable interaction of $\tau = 57 \pm 8$ s ($n = 11$) between the ubiquitin specific protease USP18 and its canonical de-ISGylation substrate, the di-ubiquitin-like ISG15 [100]. This result already illustrated the unique relationship between USP18 and ISG15, as enzymatic interactions tend to favor high turnover numbers, which in turn would suggest more transient interactions between enzyme and substrate. Moreover, this complex lifetime was well comparable to the lifetime of $\tau = 53 \pm 28$ s ($n = 8$) of micropatterned STAT2 (bait) interacting with intracellular USP18 (prey) [103], which inspired the investigations of the competition between USP18's binding partners ISG15 and STAT2 in later chapters. Incorporating the anti-GFP nanobody pull-down into live cell micropatterning thus laid the foundation for this work and also simplified the workflow of the subsequent investigations. As a side note, this assay also served to study the effects of ISG15 deficiency in humans and in mice, illustrating its potential in analyzing cell types of different species [104] (not shown).

Requiring only to generate truncations of the GFP-fused bait proteins and prey proteins, a comprehensive investigation of the structural domains of USP18 and ISG15 was readily carried out (**chapter 4.2.2**). Lacking any residues involved in the interaction with USP18, it was demonstrated that the N-terminal ISG15 domain was indeed unable to interact, as opposed to both full-length ISG15 and the C-terminal ISG15 domain, which feature all the identified interaction residues involved in binding USP18 [109].

In addition, similar experiments have examined the unstructured N-terminus of USP18, which comprises amino acids 1-42 and is known to feature two additional translation initiation sites downstream of AUG1, namely the non-canonical start codon CUG16, and start codon AUG36, leading to the expression of an N-terminal truncated isoform [110]. Strikingly, this work has shown that the Δ 42N-truncation of USP18 hinders interaction with both ISG15 (**chapter 4.2.2**) and STAT2 (**chapter 4.2.8**), albeit being an unstructured region that could not be resolved in the crystal of USP18 interacting with ISG15. In contrast, the first 42 amino acids of USP18 fused to mEGFP showed no interaction with ISG15. While mEGFP fluorescence at least indicated the expression of USP18-1-42-mEGFP, it remained uncertain whether such a small USP18 fragment was also functional. The results presented in this work thus identified an important role of USP18's N-terminus, apart from its published role in the expression of isoforms located in different cellular compartments.

Finally, the ISG15 binding boxes IBB1 and IBB2 were examined using USP18-1-169-mEGFP (1-169), which contains the thumb-domain and residues A138 and L142 of IBB1, as well as USP18-169-372-mEGFP, which features the finger and palm domains, including residues S192 and H251 of IBB1 and Q259 and W262 of IBB2 [109] (**chapter 4.2.2**). Although both USP18-truncations featured ISG15 binding residues, neither bait protein could interact with ISG15, likely due to a lack of structural features. Seeing that USP18 is not an easily segmented multi-domain protein, it is likely that these larger truncations are non-functional and therefore unable to interact with its target protein ISG15.

In conclusion, future experiments should focus on mutations of specific residues to further investigate the contribution of residues and domains, rather than truncating large protein sections. In order to investigate the function of the unstructured N-terminus of USP18, point mutations and truncations at CUG16 and AUG36 should be further employed in future pull-down experiments, and possibly phospho flow cytometry experiments, to extensively investigate their influence on the USP18 interactions and function.

5.1.1 Competition between STAT2 and negative feedback regulators USP18 and ISG15

Following the initial experiments characterizing the interaction between USP18 and ISG15, another set of experiments including STAT2 quickly revealed one of the major results of this thesis: that ISG15 competes with STAT2 for binding of USP18. Depending on the orientation of the pull-down, or rather depending on the bait protein, it was demonstrated that either ISG15 or STAT2 as bait are capable of recruiting USP18 as prey into the micropattern. In contrast, neither STAT2 nor ISG15 was able to be co-recruited into the micropattern as prey, clearly demonstrating the competition between ISG15 and STAT2 (**chapter 4.2.4**).

Briefly recapitulating the results, this competition between ISG15 and STAT2 was also validated by several control experiments, which instead of micropatterned nanobody employed directly immobilized STAT2 micropatterned at the plasma membrane as bait. This was a suitable control for the nanobody pull-down approach, as transmembrane domain fusions with STAT2 were frequently used for live cell micropatterning experiments in the past [103]. In presence of ISG15, directly micropatterned STAT2 was also not able to sufficiently recruit USP18 into the micropattern, instead demonstrating a large cytosolic background of both USP18 and ISG15, as well as low non-specific contrast values (**chapter 4.2.5**). The same competition was also observed when the IFNAR2 receptor was used as a binding site for STAT2, USP18 and ISG15 (**chapter 4.2.7**), not only validating the nanobody pull-down approach, but also confirming these results in the biological context of the involved proteins.

In addition, this thesis succeeded in demonstrating that the competition between ISG15 and STAT2 is not based on an overlapping binding site on USP18, but most likely on steric hindrance. This result was achieved by truncating the N-terminal domain of ISG15, which was known not to be involved in the interaction with USP18 [109]. Following the truncation, the C-terminal ISG15 domain gained the ability to bind USP18 together with STAT2, whereby an overlapping binding site could be excluded (see **chapters 4.2.5 - 4.2.7**). FRAP experiments further demonstrated no significant difference in the interaction dynamics between USP18 and both full-length and C-terminal ISG15, indicating an unaltered interaction that is truly relying on residues found within the C-terminal ISG15 domain (**chapter 4.2.3**).

Having these results in mind, the question arises as to what biological effects this competition has. Clearly, USP18 is not able to interact with STAT2 and ISG15 simultaneously. On the one hand, STAT2 is required as a docking site to recruit the negative feedback regulator USP18 to IFNAR2 [103]. Only then can USP18 destabilize the ternary complex, desensitize towards the lower affinity subtype IFN α 2 and cause differential IFN α/β signaling [19]. On the other hand, free ISG15 stabilizes USP18 by protecting it from proteolytic degradation, in turn preventing amplification of IFN- α/β responses and autoinflammation, making it an equally important negative feedback regulator for long-term regulation [57, 109].

ISG15 is thus a double-edged sword that protects cytosolic USP18 from degradation in the long-term, but may partially hinder USP18's function in the short term by preventing recruitment to the site of action, the ternary complex. Following this conclusion, ISG15 would indirectly regulate the negative feedback mechanism on a temporal level, as ISG15 and USP18 are both expressed in response to IFN stimulation and are crucial in priming, or desensitizing cells towards type I IFN. However, the actual impact of this ISG15/STAT2 competition may strongly depend on cellular expression levels, protein turnover, and thus the resulting protein concentrations within a specific cell type. A weakened but prolonged negative feedback regulation should therefore be seen as another adjusting screw for regulating the type I IFN signaling pathway. Hypothetically, presence of ISG15 may have a measurable effect on USP18's activity and function, which should be further investigated in future studies. For example, phospho flow cytometry [193] may be a suitable tool to analyze STAT-phosphorylation after IFN stimulation, in presence or absence of USP18 and ISG15, in order to discern possible alterations in USP18 activity.

However, the cellular effects of ISG15 should be studied as close as possible to physiological conditions where there are endogenously fewer proteins in the membrane and cytosol than in micropatterning experiments, as significantly higher protein expression and local concentration of binding partners in micropatterns could influence the equilibrium of protein interactions. Knock-out cells of USP18 $-/-$ and ISG15 $-/-$ could therefore be employed, combined with vectors for transient expression featuring less potent promoters, or even combined with CRISPR/Cas, to assure low, endogenous expression of target proteins. In any case, there are many methods to follow-up on this PPI characterization, with which the effects of USP18 and ISG15 should be further investigated.

5.1.2 Nanobody live cell micropatterning as a robust pull-down method

The objective of this thesis was to develop novel pull-down and micropatterning methods for investigating interaction dynamics and stoichiometry of cytosolic PPIs of the type I IFN signaling pathway. Furthermore, these methods were aimed to simplify the workflow of qualitative and quantitative PPI analysis, by employing PLL-PEG to readily introduce biocompatible functionalization and surface passivation. Finally, the use of an anti-GFP nanobody that specifically captures any of the commonly used GFP-tagged proteins makes this a generically applicable approach, that is not just suitable for studying the type I IFN signaling pathway, but also for many other biological questions.

It should therefore be assessed whether nanobody live cell micropatterning can truly provide a simplified, yet robust method for investigating cytosolic PPIs. The results of this work demonstrate that PLL-PEG was successfully used to generate live cell micropatterns which exhibited minimal fluorescent background in a TIRFM experimental setup, serving as an internal control for specific immobilization of nanobodies and capture of bait and prey proteins. Perhaps the biggest improvement of this assay is the use of nanobodies, which feature all the advantages of antibodies, yet none of their shortcomings. Nanobodies offer specific high affinity antigen binding and consist of only a single gene encoding their single domain structure. This fact enabled us to generate the HaloTag-mTagBFP-TMD-NB construct for easy intracellular micropatterning of cytosolic proteins. In contrast, previous methods were forced to employ surface architectures functionalized with unique antibodies directed against each specific target [166], or required affinity handles like the HaloTag or Strep-tag which required additional cloning work [103, 158]. The nanobody construct employed in this work can therefore be described as the basis that enabled a plethora of investigations, which only required commonly used GFP-tagged proteins, thus truly simplifying the workflow. However, nanobody live cell micropatterning faces the same challenges as any other live cell method, namely the risk of creating overexpression artefacts by inducing the required fluorescent fusion proteins. This leads to a potential saturation of binding sites within the micropattern, which may prevent accumulation of nanobodies, bait proteins, or even prey proteins within the micropattern, in turn causing a background of proteins that bias the observable fluorescence contrast. This risk was substantially alleviated by exploiting the core feature of micropatterning itself: that target proteins are specifically captured in micropatterns

and that the non-functionalized pattern (or the negative, opposite pattern) can be used as an internal control for non-specific binding and background fluorescence.

To this end, bait specific fluorescence contrast analysis was employed (**chapter 3.4.2**), correcting the contrast of micropatterned proteins for the ratio of directly immobilized proteins within the micropattern, enabling statistical analysis of transiently transfected cells that exhibited fluctuating protein expression. However, does this normalization of contrast values mean that all experimental results can be directly compared with one another? This consideration may be tempting, but is not permissible. As soon as major changes are made to the experimental setup, such as the use of a different bait protein, the experiments are no longer directly comparable, as the consequences to the equilibrium cannot be reliably predicted.

As seen, significant differences were observed regarding the fluorescence contrast of the recruited USP18 for several sets of experiments (**chapter 4.2.4**), which may indicate an experimental artefact caused by protein overexpression. Another possible explanation, which has not yet been discussed, could be that ISG15 is able to recruit USP18 into the micropattern more efficiently than when using STAT2 as bait, which would imply a higher affinity of USP18 for ISG15 than for STAT2. However, this is refuted when considering the interaction dynamics between USP18 and ISG15 characterized in this thesis and when comparing it with the interaction dynamics of USP18 and STAT2 characterized in a previous publication [103]. As shown, fluorescence recovery after photobleaching (FRAP) was employed to observe the exchange kinetics of micropatterned USP18 (bait) binding intracellular ISG15 (prey), yielding an interaction lifetime of $\tau = 54.2 \pm 10.1$ s ($n = 14$) (**chapter 4.2.3**). Similarly, micropatterned STAT2 (bait) interacting with intracellular USP18 (prey) featured an interaction lifetime of $\tau = 53 \pm 28$ s ($n = 8$) [103]. Statistical analysis via a two-sample t-test (Welsh's t-test) on these relatively similar interaction lifetimes gave a p-value of just $p = 0.91$, concluding no significant difference between USP18 interacting with ISG15 or with STAT2. As such, differences between fluorescence contrasts of USP18 recruited to different bait proteins (**chapter 4.2.4, Figure 25**) must be attributed to higher-level factors such as protein overexpression, different protein turnover of cytosolic and membrane-anchored proteins, or simply a different equilibrium in these experiments.

Moreover, the results when performing a pull-down with directly immobilized STAT2 or IFNAR2 as bait (**chapter 4.2.5, 4.2.7**) also differ from the two nanobody pull-down experiment, illustrating that different experimental systems or setups should not be directly compared. It is therefore advisable for PPI investigations to introduce only incremental changes into an experimental system, e.g. a mutation or a truncation, and not to treat fluorescence contrast values as an absolute specific value for an interaction. Instead, relative changes in fluorescence contrast should be observed within the same experimental system in a semi-quantitative manner, in order to reach meaningful insights. Taking this conclusion into account, the generic nanobody live cell micropatterning is an extremely robust method that allows even the most diverse cells to be statistically evaluated through a normalized evaluation of the fluorescence contrast.

5.1.3 Two-hybrid nanobody pull-down assays to investigate distinct complexes

Aiming to specifically capture interacting proteins as a complex, bimolecular fluorescence complementation (BiFC) was integrated into the nanobody live cell micropatterning assay. As demonstrated by a series of proof-of-concept experiments, split-GFP fragments can be readily fused with proteins of interest and captured by the anti-GFP nanobody upon interaction and complementation (**chapter 4.2.9**). Even in presence of the anti-GFP NB, split-GFP fragments do not undergo complementation without any specific interaction of their fusion proteins, which is necessary to bring the fragments into close proximity. Since individual split-GFP fragments are neither visible nor being captured into the NB micropattern, any non-interacting proteins are completely disregarded and only complexes of interacting proteins are captured for analysis. Moreover, even very transient PPIs will accumulate over time in protein complexes, as split-GFP complementation irreversibly locks the fusion proteins in their interactions.

The distinct advantage of the split two-hybrid nanobody live cell micropatterning is therefore not only selectivity, but also sensitivity for transient interactions. This two-hybrid nanobody pull-down approach was successfully validated by experiments employing split-fusions of USP18-NmEGFP and CmEGFP-ISG15, which yielded similar results to the previous experiments. Competition between STAT2 and ISG15 for binding USP18 clearly hindered fluorescence complementation of the split-GFP fusions, and when the C-terminal ISG15 domain was used, this competition was completely abolished and all three proteins were present in the micropattern (**chapter 4.2.10**).

This result lay the foundation for new possibilities of a combined two-hybrid nanobody pull-down assay. In conclusion, it is possible to foresee a multicolor fluorescence complementation analysis where several complementation proteins (e.g. BFP, CFP, GFP and YFP) are simultaneously employed, enabling pull-down and interaction analysis of distinct protein combinations within complemented complexes [168].

5.2 SiCPull for background-free investigation of interaction dynamics

Recapitulating on the first half of this thesis, the nanobody live cell micropatterning is a robust method to analyze not only a single PPI between two proteins, but also more complex interactions between multiple interaction partners in a semi-quantitative manner. In contrast to FRAP, which yields absolute lifetime values of interaction kinetics, fluorescence contrast analysis of micropatterned proteins is aiming to observe relative changes within an experimental system and thus functions more as a semi-quantitative analysis. As demonstrated, this makes micropatterning a powerful tool to analyze interactions, by introducing additional interaction partners and competitors into the experimental setup. It is even possible to perform comparative studies between wildtype interactions and mutants, as well as functional truncations, in order to investigate the molecular mechanisms of a specific PPI. Thus, fluorescence contrast analysis of micropatterned proteins reliably identifies altered interactions through an analysis of significant changes within the experimental system.

As mentioned earlier, fluorescence contrast analysis has its limitations, as it does not reveal properties characteristic of a particular PPI, such as a dissociation rate constant for example. Therefore, PPIs cannot be compared directly between unrelated sets of experiments, especially when using entirely different bait and prey protein combinations. Each protein, or more specifically, each construct of fusion proteins involved, may behave completely differently in living cells, e.g. by having a distinct expression level, turnover and equilibrium, in turn requiring a different cell type or knock-out cells for an unbiased experiment. For these reasons, only semi-quantitative conclusions can be drawn about whether a PPI is stronger than another PPI by simply observing the visual contrast, as the contrast is ultimately subject to higher-level factors. In case of investigating the specific interaction dynamics of a PPI, other analysis tools should be employed alongside the fluorescence contrast analysis, like FRAP in living cells. Alternatively, SiCPull can be used for a background free detection, which was developed in this work to enable a more quantitative and unbiased characterization of PPIs.

True to its name, the *in situ* single cell pull-down (SiCPull) enables investigation of proteins captured into nanobody surface micropatterns within close proximity of individual cells. Cells are exploited for their overexpression of proteins upon transient transfection, grown on micropatterned surface architectures, and lysed by addition of a lysis buffer containing a mild detergent. Cytosolic proteins are immediately released from the cell during lysis, and GFP-tagged bait proteins and interacting prey proteins are almost instantly captured into the anti-GFP nanobody micropattern. As demonstrated in this thesis, interaction kinetics can then be analyzed by simply observing the dissociation of co-captured prey proteins from the micropatterned GFP-fused bait proteins. As the fluorescent prey proteins dissociate and dilute into the medium, the fluorescence within the micropattern follows an exponential decay corresponding to the characteristic lifetime of the specific PPI (**chapter 4.3.3**). This process is thus similar to a FRAP analysis, where the fluorescence signal recovers after photobleaching, as bleached proteins are substituted by fluorescent proteins from the cytosol, again corresponding to their interaction lifetime. However, the disadvantage of FRAP is that a balanced protein expression is required. On the one hand, a potent background population of fluorescent proteins is required that can readily replace the bleached proteins, so as not to be limited by the diffusion of fluorescent proteins to the micropattern. On the other hand, too much background signal can distort the analysis of the recovering signal, which is easily caused by protein overexpression and requires thorough correction for this bias (**chapter 3.4.3, Equation 4**). In contrast, this balancing act is not required when using SiCPull, as it does not face the challenges of protein overexpression and an excessively high fluorescent signal in the cytosolic background of the micropattern. SiCPull can simply measure the fluorescence signal of captured GFP-tagged bait proteins and interacting prey proteins inside and outside the surface micropattern, since any cellular or cytosolic background is diluted during cell-lysis and is not detectable via TIRFM (**chapter 3.4.4**). In addition, any excess of target proteins that exceeds the binding capacity of the micropattern is also diluted into the medium and does not bias the analysis. Therefore, SiCPull experiments can be performed at any expression level, making it a robust, unbiased method for background-free characterization of cytosolic PPIs.

As shown in this work and as previously published by us [160], SiCPull successfully demonstrated its capabilities by resolving STAT dimerization that ranged from stable down to extremely transient interactions. By simply using STAT1-mEGFP as bait and

STAT1, STAT2, STAT3 fused with TagRFpt as prey, cell lysis, co-capturing and subsequent dissociation could be observed via TIRFM (**chapter 4.3.3**). This revealed two distinct interactions for STAT1-STAT1 homodimers, as dissociation followed a bi-exponential behavior yielding two characteristic lifetimes of ~22 seconds and a drastically more stable one of ~41 minutes. While STAT1-STAT2 heterodimers gave a similar lifetime of ~24 seconds, STAT1-STAT3 heterodimers showed a lifespan of only ~2 seconds. Remarkably, even such a transient interaction which dissociated within the first seconds after lysis could still be resolved via SiCPull, and which may have been lost in case of time-consuming *in vitro* protein purification assays. Importantly, these STAT1-STAT1 homodimers and STAT1-STAT2 and STAT1-STAT3 heterodimers were investigated without IFN stimulation, confirming their postulated dimerization in absence of phosphorylation [80, 82, 98]. The interaction dynamics gathered here should be followed up by a future investigation, looking into the influence of IFN-induced STAT phosphorylation on STAT interaction dynamics. As seen by the single molecule stoichiometry investigations, which will be discussed in the following, STAT1 stoichiometry was seemingly not affected by phosphorylation (**chapter 4.3.6**), and therefore it would be quite interesting to investigate this on the interaction dynamics, too. In conclusion, the *in situ* single cell pull-down (SiCPull) was demonstrated to be a simple, robust and unbiased method to investigate even transient cytosolic PPIs without the need for elaborate cell lysis and protein purification protocols, which are usually required for *in vitro* investigations. This left only the investigation of STAT stoichiometry in presence and absence of IFN stimulation, which required a single molecule pull-down in order to detect individual protein complexes.

5.2.1 Single molecule SiCPull to investigate cytosolic STAT and JAK stoichiometry

Concluding the single molecule investigations of this thesis, it is time to evaluate the biological findings on the stoichiometry of cytosolic PPIs involved in type I IFN signaling, as well as the workflow of the single molecule single cell pull-down (SM-SiCPull). It was demonstrated in this thesis that SM-SiCPull can be successfully used to investigate the stoichiometry of a cytosolic PPI, in this case STAT1 oligomerization in absence and presence of IFN stimulation. As initially stated, STAT1 is an ideal model system for stoichiometric investigations, as it features a well characterized dimerization [46, 82] and a reported tetramerization [80]. Furthermore, dimerization in absence of phosphorylation was proposed to play a unique role in gene transcription and

regulation of expression [99] and even the tetramerization was reported in absence of phosphorylation [80]. Therefore, STAT1 stoichiometry was to be investigated before and after 20 minutes of IFN stimulation, but first a challenge had to be overcome.

Phosphorylated STAT1 canonically dimerizes and translocates into the nucleus, where, surprisingly, it was retained during cell lysis and not released (**chapter 4.3.6**). This was finally overcome by employing STAT1-L407A, which is a mutant that is unable to bind importin- α 5 and therefore remains in the cytosol [40], from where it can be captured following IFN stimulation and cell lysis. As nuclear translocation could potentially be rescued by interaction with endogenous STAT2, HeLa double knockout cells (STAT1 $-/-$, STAT2 $-/-$) needed to be employed. Regarding nuclear translocation and retention in general, this challenge could also be overcome by simply deleting or mutating the nuclear localization signal (NLS), or by employing an inhibitor of nuclear transport [194]. Thus, other solutions readily exist if this is relevant for the investigation of other PPIs in the future. To make a virtue out of necessity, it is also possible to exploit SiCPull to specifically capture cytosolic proteins while ignoring those localized within the nucleus, thus having a simple way to discriminate between cellular compartments.

Finally, this enabled the SM-SiCPull of STAT1, in absence and presence of IFN stimulation, demonstrating that STAT1 phosphorylation surprisingly does not change the equilibrium of STAT1 stoichiometry, even though STATs are canonically described to undergo phosphorylation-induced homo- and heterodimerization [59, 88, 93]. Revisiting the results, both unstimulated and IFN stimulated cells yielded STAT1 stoichiometries of 36.9% and 37.8% monomers, 25.2% and 21.7% dimers, 14.2% and 16.6% trimers, as well as 21.64% and 20.4% oligomers, respectively (**Figure 40**). Moreover, oligomers included tetramers up to octamers, but even higher oligomers were excluded from the results section due to their even lower percentages.

Now, what must be considered when interpreting these results? Considering the control experiments, monomeric GFP (mEGFP) yielded a stoichiometry of 95.4% monomers, but also 3.5% dimers, 0.7% trimers and 0.1% oligomers (**chapter 4.3.5**), which correspond to multiple overlapping binding sites, respectively. Simulating a dimeric interaction, tandem GFP (tdmEGFP) showed 61.1% monomers, 31.7% dimers, 5.3% trimers and 1.3% oligomers, which illustrates the degree of labeling, or in this case the fluorophore maturation [192], which is a typical challenge in fluorescence microscopy and spectroscopy.

This teaches us two things: First, a very small proportion of signals are still biased by diffraction limitations, as molecules are captured too closely to resolve them, which is caused by the random distribution of nanobodies within the micropattern. Second, the varying maturation of GFP fluorophores leads to a range of detectable stoichiometries reflecting not only all possible combinations of interacting proteins, but also of those proteins captured too closely together. This is the reason why we observe not only dimers in the tdmEGFP control, but also monomers and even small percentages of tetramers. Likewise, STAT1 was reported to homo-dimerize and tetramerize, whereas observed stoichiometries reached from monomers to octamers.

However, these few cases are irrelevant for the stoichiometric investigation, as they are caused by a systematic error which depends solely on the employed fluorophore, in this case mEGFP, and the surface density of nanobodies used for capturing. This systematic error remaining constant is perhaps one of the biggest advantages of SM-SiCPull, which was developed to analyze the stoichiometric distribution of an entire population of cytosolic proteins. In contrast to crystallography, which can unravel an ideal stoichiometry of a PPI, SM-SiCPull is meant to compare the stoichiometric distribution of a specific PPI and to detect changes within the equilibrium of proteins. This makes SM-SiCPull a robust tool with a simple workflow to investigate the influence of different stimulations, truncations, mutations, or additional proteins such as competitors on a specific PPI.

After SM-SiCPull has shown that the supposed phosphorylation-induced homo- and heterodimerization [39] does not change the stoichiometry of STAT1, further research should be conducted to follow up on these results. As initially stated, the N-terminal domain (ND) of STATs was identified to direct homodimerization of inactive unphosphorylated STATs, as well as tetra- or oligomerization of STATs interacting with DNA [59, 80-82]. Furthermore, the ND was also proposed to be required for reorientation of STAT1 dimers to enable dephosphorylation of STAT1 [83]. It would therefore be very promising to investigate STAT1 stoichiometry in comparison with a truncation of the ND, which should have a severely noticeable effect. Hypothetically, deletion of the ND should prohibit STAT dimerization and inhibit nuclear translocation, which is also regulated by the ND [84], making such a truncation an ideal case for SM-SiCPull and stoichiometry analysis before and after IFN stimulation. Furthermore, such a STAT1- Δ ND construct could serve as a negative control for STAT dimerization in general.

Moreover, the here described SM-SiCPull only utilized homo-interactions and therefore one target protein and one fluorescent label at a time, namely mEGFP. It would be quite exciting to advance SM-SiCPull further, in order to investigate the stoichiometry of multiple target proteins by incorporating additional fluorescent labels. Following SM-SiCPull, multiple captured and co-localized proteins could then be analyzed, giving insights on their complex composition. Even protein analysis via immunostaining, e.g. with regard to posttranslational modifications, can be envisioned, making further developments of SM-SiCPull an exciting prospect.

5.2.2 Incorporating the two-hybrid approach into SM-SiCPull

Like for the nanobody live cell micropatterning assay, a two-hybrid pull-down was also implemented in the SM-SiCPull to specifically target complexes of interacting proteins. Serving as a proof of concept, the intracellular domain of the thrombopoietin receptor (TpoR) and JAK2 and have been employed, which have each been fused with a split GFP domain (**chapter 4.3.7**) and are a suitable model system as receptor-associated JAKs have been previously shown to contribute to receptor dimerization [20]. Furthermore, the oncogenic JAK2-V617F mutation induces ligand-independent receptor dimerization, which was demonstrated by observing co-locomotion of receptors within living cells [20]. As expected, stoichiometry was clearly shifted towards oligomerization when comparing wildtype JAK2 with JAK2-VF, reflecting the increased dimerization rate of the V617F mutation (**chapter 4.3.7**). SM-SiCPull thus offers an alternative for investigating cytosolic, receptor-associated proteins while interacting with an intracellular receptor domain. Furthermore, SM-SiCPull can be successfully combined with a two-hybrid approach, using BiFC to specifically capture and analyze only complexes of interacting proteins, while neither observing nor capturing the individual proteins of interest.

Similar to the NB live cell micropatterning approach, SiCPull and SM-SiCPull can also be envisioned to employ several labeled target proteins, or even several split fluorescent proteins for a multicolor analysis. This would enable to investigate interaction dynamics between individual complexes of defined protein compositions via SiCPull, as well as their stoichiometry via SM-SiCPull. As initially stated, complementation is even possible between truncations of different fluorescent proteins (e.g. BFP, CFP, GFP, YFP) [189], each resulting in unique spectral properties. When fused with several target proteins, SM-SiCPull may even be used to analyze the spectral properties of these individual complexes.

In conclusion, BiFC could be readily implemented in any of the methods presented in this work, as both the nanobody live cell micropatterning and the single cell pull-down approaches revolve around the simple strategy of capturing GFP-fused target proteins. Having the ability to implement BiFC for a two-hybrid approach gives much more control over the captured target proteins, in turn strengthening the investigations of protein-protein interaction dynamics and stoichiometry.

5.2.3 Good analysis practice and workflow of SM-SiCPull

In order to carry out the *in situ* single cell pull-down on the single molecule level, nanobody surface densities had to be reduced significantly, as the micropatterns were designed for a maximized pull-down of an ensemble of proteins. To this end, a new protocol for surface architectures was developed, in which an optimal density of anti-GFP nanobody was titrated (**chapter 4.3.4**). This step was crucial, as a sufficiently low surface density of nanobodies is required to avoid overlapping fluorescence signals of captured proteins, which cannot be resolved due to diffraction limitations and would thus bias the analysis. It is therefore advisable to thoroughly titrate the surface density for each adaptation of the methods presented in this work, as well as to repeat this control for each new batch or synthesis of the materials used for surface preparation. In this thesis, SM-SiCPull has been shown to reliably detect single molecules even when employing surfaces with a density of ≤ 0.5 particles/ μm^2 , which was chosen as a compromise for the highest possible surface density that is still yielding a reliable monomeric result in the control.

Interestingly, another single molecule pull-down assay called SiMPull, which was previously described by others, recommends an optimal density of only 0.1 to 0.2 particles/ μm^2 for an unbiased analysis[195], which is most likely related to the different surface architecture and analysis tools. Since SiMPull employs randomly arranged binding sites on a chip and lacks an internal control for specific protein capturing, this optimal surface density may be related to minimizing a possible bias. Again, one of the biggest advantages of SiCPull and SM-SiCPull is the arrangement of nanobodies within micropatterns, as the non-functionalized area serves as an internal control for surface passivation, background signals and non-specific binding. Since monomeric GFP control experiments showed no significant increase of overlapping signals at this surface density, both data analysis and pull-down experiments could be performed with high confidence under harsh parameters and the analysis yielded reliable results even for different datasets.

Moreover, the workflow of SM-SiCPull and the subsequent data analysis is quite simple. Similar to SiCPull, transiently transfected cells are grown and lysed on micropatterned surfaces, and the released cytosolic proteins are captured into NB micropatterns within close proximity to the individual cells. Following this strategy, the challenges of protein expression levels are trivialized, as surface density of captured proteins is dictated by the nanobody, not the amounts of protein in the host cell. Following lysis, the entire coverslide is fixed by the addition of PFA, which fixes all captured bait and prey proteins, preventing any dissociation over time and allowing unlimited acquisition of fluorescence bleaching movies without time limitations (**chapter 3.4.5**). Without this step, co-captured proteins would dissociate according to their characteristic lifetime, turning any delayed stoichiometric analysis of captured complexes ad absurdum. A prior surface scan for the positions of protein-expressing cells aided the workflow, as it serves to reliably find the position of cells after the lysis and fixation procedure. This in turn enables an easy acquisition of dozens of fluorescence bleaching movies on a single microscopy coverslide, which can acquire thousands of single molecules for a pooled statistical analysis over the entire dataset (**chapter 4.3.5**). As initially explained, SLIMfast is then used to specifically localize molecules within the micropattern for each frame of the bleaching movies, followed by an immobile cluster detection to combine these signals across multiple frames, yielding intensity traces over time (**chapter 3.4.6**).

It is important to emphasize that this analysis is carried out under specific assumptions, which must be corrected if they are not applicable, e.g. if fluorescence quenching or blinking occurs. In this example, a blinking particle may result in an on/off signal over several frames, which is more difficult to detect as one and the same molecule over several frames, thus requiring more relaxed parameters to stitch together the signals over time. The localization itself should also be handled with special care, in order to generate comparable data and robust parameters. Limits should be set increasingly harsher, only to slightly relax the parameters once the algorithm stops, which of course needs to be individually evaluated for a different fluorophore. Localization precision obviously varies greatly between fluorophores, as the extinction coefficient and quantum yield are very different for all kinds of fluorophores, too. In case of this work, mEGFP could be localized with a precision of 20 nm, resulting in a chosen search radius of 80 nm. In general, human visual feedback ensures sensibly chosen parameters, according to one's own

quality standard, as the human eye easily recognizes wrongly connected clusters or broken localizations (**chapter 4.3.5, Figure 37b**).

Continuing with the SM-SiCPull workflow, localized molecules from several bleaching movies of the same microscopy coverslide are then pooled and exported into the BleachCounter, a custom-made Matlab application (**chapter 3.4.6**). In this tool, intensity magnitudes of detected bleaching steps are correlated with their 2D coordinates, generating a spatial fluorophore intensity distribution map, which is required to account and correct for heterogeneous sample illumination. Usually, particles were fitted with a relative error below 10%, highlighting the good agreement between this 2D illumination profile and the actual recorded data. Moreover, this fit becomes increasingly more reliable in proportion to the number of acquired data, as more bleaching steps can be used. To account for the illumination bias of the experimental microscope setup, this specific illumination profile is then applied to calculate the stoichiometry of thousands of detected molecules, based on their 2D coordinate and detected fluorescence intensity. Again, it must be stressed that this analysis should be handled with special care, choosing harsher or relaxed parameters depending on each dataset. Experiments must be handled individually, as microscope and coverslide alignments may vary from experiment to experiment, yielding a unique illumination profile, and because specific PPIs and fluorescent markers behave highly differently too.

When following these guidelines, SM-SiCPull and the associated analysis tools provide an extremely robust and reliable method to investigate the stoichiometry of an entire population of cellular cytosolic proteins. The simple workflow allows thousands of molecules to be easily acquired and pooled into one dataset, further strengthening the statistical analysis and progressively reducing any errors of the used software algorithms. Employing the *in situ* single cell pull-down for more complex biological questions will further advance the method as well as the software analysis.

To conclude this work, the quantitative interaction analyses of cytosolic proteins have indeed demonstrated the capabilities of the here developed assays. Both the nanobody live cell micropatterning and the single cell pull-down assays provided a robust and versatile toolbox for investigating cytosolic protein-protein interactions of the type I IFN signaling pathway and have provided meaningful insights in a cellular context. It will be particularly exciting to see how future studies will follow up on the findings about the negative feedback regulators USP18 and ISG15, and the STAT effector proteins.

6 Appendix

6.1 References

1. Schuster, S.C., *Next-generation sequencing transforms today's biology*. Nature Methods, 2008. **5**(1): p. 16-18.
2. van Dijk, E.L., et al., *Ten years of next-generation sequencing technology*. Trends in Genetics, 2014. **30**(9): p. 418-426.
3. Hu, T., et al., *Next-generation sequencing technologies: An overview*. Human Immunology, 2021.
4. Aebersold, R. and M. Mann, *Mass spectrometry-based proteomics*. Nature, 2003. **422**(6928): p. 198-207.
5. Bensimon, A., A.J.R. Heck, and R. Aebersold, *Mass Spectrometry-Based Proteomics and Network Biology*. Annual Review of Biochemistry, 2012. **81**(1): p. 379-405.
6. Kim, M.-S., et al., *A draft map of the human proteome*. Nature, 2014. **509**(7502): p. 575-581.
7. Jumper, J., et al., *Highly accurate protein structure prediction with AlphaFold*. Nature, 2021. **596**(7873): p. 583-589.
8. Goulet, A. and C. Cambillau, *Present Impact of AlphaFold2 Revolution on Structural Biology, and an Illustration With the Structure Prediction of the Bacteriophage J-1 Host Adhesion Device*. Front Mol Biosci, 2022. **9**: p. 907452.
9. Dunham, I., et al., *An integrated encyclopedia of DNA elements in the human genome*. Nature, 2012. **489**(7414): p. 57-74.
10. Nurk, S., et al., *The complete sequence of a human genome*. Science, 2022. **376**(6588): p. 44-53.
11. Wang, E.T., et al., *Alternative isoform regulation in human tissue transcriptomes*. Nature, 2008. **456**(7221): p. 470-476.
12. Pan, Q., et al., *Deep surveying of alternative splicing complexity in the human transcriptome by high-throughput sequencing*. Nature genetics, 2008. **40**(12): p. 1413-1415.
13. Hong, D.S., et al., *KRASG12C Inhibition with Sotorasib in Advanced Solid Tumors*. New England Journal of Medicine, 2020. **383**(13): p. 1207-1217.
14. Skoulidis, F., et al., *Sotorasib for Lung Cancers with KRAS p.G12C Mutation*. New England Journal of Medicine, 2021. **384**(25): p. 2371-2381.
15. Kargbo, R.B., *Small-Molecule Inhibitor of the Oncogenic KRASG12C Mutant for the Treatment of Currently Incurable Cancer*. ACS Medicinal Chemistry Letters, 2022. **13**(5): p. 767-769.
16. Zhang, Z., et al., *Development and Preclinical Evaluation of Radiolabeled Covalent G12C-Specific Inhibitors for Direct Imaging of the Oncogenic KRAS Mutant*. Mol Pharm, 2021. **18**(9): p. 3509-3518.
17. Hofmann, M.H., et al., *Expanding the Reach of Precision Oncology by Drugging All KRAS Mutants*. Cancer Discovery, 2022: p. OF1-OF14.
18. Morris, R., N.J. Kershaw, and J.J. Babon, *The molecular details of cytokine signaling via the JAK/STAT pathway*. Protein Science, 2018. **27**(12): p. 1984-2009.
19. Wilmes, S., et al., *Receptor dimerization dynamics as a regulatory valve for plasticity of type I interferon signaling*. Journal of Cell Biology, 2015. **209**(4): p. 579-593.
20. Wilmes, S., et al., *Mechanism of homodimeric cytokine receptor activation and dysregulation by oncogenic mutations*. Science, 2020. **367**(6478): p. 643-652.

21. Rawlings, J.S., K.M. Rosler, and D.A. Harrison, *The JAK/STAT signaling pathway*. Journal of cell science, 2004. **117**(8): p. 1281-1283.
22. Carbone, C.J. and S.Y. Fuchs, *Eliminative signaling by Janus kinases: role in the downregulation of associated receptors*. Journal of cellular biochemistry, 2014. **115**(1): p. 8-16.
23. Chatterjee-Kishore, M., F.v.d. Akker, and G.R. Stark, *Association of STATs with relatives and friends*. Trends in Cell Biology, 2000. **10**(3): p. 106-111.
24. Garbers, C., et al., *Plasticity and cross-talk of interleukin 6-type cytokines*. Cytokine & growth factor reviews, 2012. **23**(3): p. 85-97.
25. Kang, S., et al., *Historical overview of the interleukin-6 family cytokine*. Journal of Experimental Medicine, 2020. **217**(5).
26. Nicola, N.A., *Cytokine pleiotropy and redundancy: a view from the receptor*. Stem cells (Dayton, Ohio), 1994. **12**: p. 3-12; discussion 12.
27. Borden, E.C., et al., *Interferons at age 50: past, current and future impact on biomedicine*. Nature reviews Drug discovery, 2007. **6**(12): p. 975-990.
28. Wilmes, S., et al., *Competitive binding of STATs to receptor phospho-Tyr motifs accounts for altered cytokine responses*. eLife, 2021. **10**: p. e66014.
29. Greenhalgh, C.J. and D.J. Hilton, *Negative regulation of cytokine signaling*. Journal of Leukocyte Biology, 2001. **70**(3): p. 348-356.
30. Stetson, D.B. and R. Medzhitov, *Type I interferons in host defense*. Immunity, 2006. **25**(3): p. 373-381.
31. Moraga, I., et al., *Receptor density is key to the alpha2/beta interferon differential activities*. Molecular and cellular biology, 2009. **29**(17): p. 4778-4787.
32. Levin, D., D. Harari, and G. Schreiber, *Stochastic receptor expression determines cell fate upon interferon treatment*. Molecular and cellular biology, 2011. **31**(16): p. 3252-3266.
33. Isaacs, A., J. Lindenmann, and C.H. Andrewes, *Virus interference. I. The interferon*. Proceedings of the Royal Society of London. Series B - Biological Sciences, 1957. **147**(927): p. 258-267.
34. Wang, X., et al., *Structural biology of shared cytokine receptors*. Annual review of immunology, 2009. **27**: p. 29-60.
35. Pestka, S., C.D. Krause, and M.R. Walter, *Interferons, interferon-like cytokines, and their receptors*. Immunological reviews, 2004. **202**(1): p. 8-32.
36. Jaitin, D.A., et al., *Inquiring into the differential action of interferons (IFNs): an IFN- α 2 mutant with enhanced affinity to IFNAR1 is functionally similar to IFN- β* . Molecular and cellular biology, 2006. **26**(5): p. 1888-1897.
37. Lamken, P., et al., *Ligand-induced assembling of the type I interferon receptor on supported lipid bilayers*. Journal of molecular biology, 2004. **341**(1): p. 303-318.
38. Jaks, E., et al., *Differential receptor subunit affinities of type I interferons govern differential signal activation*. Journal of molecular biology, 2007. **366**(2): p. 525-539.
39. Piehler, J., et al., *Structural and dynamic determinants of type I interferon receptor assembly and their functional interpretation*. Immunological reviews, 2012. **250**(1): p. 317-334.
40. McBride, K.M., et al., *Regulated nuclear import of the STAT1 transcription factor by direct binding of importin- α* . The EMBO Journal, 2002. **21**(7): p. 1754-1763.
41. Cohen, B., et al., *Ligand-induced association of the type I interferon receptor components*. Molecular and cellular biology, 1995. **15**(8): p. 4208-4214.

42. Bluyssen, H.R. and D.E. Levy, *Stat2 Is a Transcriptional Activator That Requires Sequence-specific Contacts Provided by Stat1 and p48 for Stable Interaction with DNA* *. Journal of Biological Chemistry, 1997. **272**(7): p. 4600-4605.
43. Au-Yeung, N., R. Mandhana, and C.M. Horvath, *Transcriptional regulation by STAT1 and STAT2 in the interferon JAK-STAT pathway*. Jakstat, 2013. **2**(3): p. e23931.
44. Blaszczyk, K., et al., *The unique role of STAT2 in constitutive and IFN-induced transcription and antiviral responses*. Cytokine & Growth Factor Reviews, 2016. **29**: p. 71-81.
45. Platanitis, E., et al., *A molecular switch from STAT2-IRF9 to ISGF3 underlies interferon-induced gene transcription*. Nature Communications, 2019. **10**(1): p. 2921.
46. Sehgal, P.B., *Paradigm shifts in the cell biology of STAT signaling*. Seminars in Cell & Developmental Biology, 2008. **19**(4): p. 329-340.
47. Kalie, E., et al., *The stability of the ternary interferon-receptor complex rather than the affinity to the individual subunits dictates differential biological activities*. Journal of Biological Chemistry, 2008. **283**(47): p. 32925-32936.
48. Lavoie, T.B., et al., *Binding and activity of all human alpha interferon subtypes*. Cytokine, 2011. **56**(2): p. 282-289.
49. Kalie, E., et al., *An interferon $\alpha 2$ mutant optimized by phage display for IFNAR1 binding confers specifically enhanced antitumor activities*. Journal of Biological Chemistry, 2007. **282**(15): p. 11602-11611.
50. Thomas, C., et al., *Structural linkage between ligand discrimination and receptor activation by type I interferons*. Cell, 2011. **146**(4): p. 621-632.
51. Platanias, L.C., *Mechanisms of type-I-and type-II-interferon-mediated signalling*. Nature Reviews Immunology, 2005. **5**(5): p. 375-386.
52. Arimoto, K.-I., et al., *Negative regulation of type I IFN signaling*. Journal of Leukocyte Biology, 2018. **103**(6): p. 1099-1116.
53. François-Newton, V., et al., *USP18-based negative feedback control is induced by type I and type III interferons and specifically inactivates interferon α response*. PloS one, 2011. **6**(7): p. e22200.
54. Zhang, D. and D.-E. Zhang, *Interferon-stimulated gene 15 and the protein ISGylation system*. Journal of interferon & cytokine research, 2011. **31**(1): p. 119-130.
55. Bogunovic, D., et al., *Mycobacterial disease and impaired IFN- γ immunity in humans with inherited ISG15 deficiency*. Science, 2012. **337**(6102): p. 1684-1688.
56. Durfee, L.A. and J.M. Huibregtse, *Identification and validation of ISG15 target proteins*. Conjugation and Deconjugation of Ubiquitin Family Modifiers, 2010: p. 228-237.
57. Zhang, X., et al., *Human intracellular ISG15 prevents interferon- α/β over-amplification and auto-inflammation*. Nature, 2015. **517**(7532): p. 89-93.
58. Stark, G.R., et al., *How cells respond to interferons*. Annual review of biochemistry, 1998. **67**(1): p. 227-264.
59. Schindler, C., D.E. Levy, and T. Decker, *JAK-STAT signaling: from interferons to cytokines*. J Biol Chem, 2007. **282**(28): p. 20059-63.
60. Haan, C., et al., *Jaks and cytokine receptors—an intimate relationship*. Biochemical pharmacology, 2006. **72**(11): p. 1538-1546.
61. Haan, C., et al., *Mapping of a region within the N terminus of Jak1 involved in cytokine receptor interaction*. Journal of Biological Chemistry, 2001. **276**(40): p. 37451-37458.

62. Girault, J.-A., et al., *Janus kinases and focal adhesion kinases play in the 4.1 band: a superfamily of band 4.1 domains important for cell structure and signal transduction*. *Molecular Medicine*, 1998. **4**(12): p. 751-769.
63. Radtke, S., et al., *The Jak1 SH2 Domain Does Not Fulfill a Classical SH2 Function in Jak/STAT Signaling but Plays a Structural Role for Receptor Interaction and Up-regulation of Receptor Surface Expression*. *Journal of Biological Chemistry*, 2005. **280**(27): p. 25760-25768.
64. Ragimbeau, J., et al., *The tyrosine kinase Tyk2 controls IFNAR1 cell surface expression*. *The EMBO journal*, 2003. **22**(3): p. 537-547.
65. Marijanovic, Z., et al., *TYK2 activity promotes ligand-induced IFNAR1 proteolysis*. *Biochemical Journal*, 2006. **397**(1): p. 31-38.
66. Kumar, K.S., et al., *Basal ubiquitin-independent internalization of interferon α receptor is prevented by Tyk2-mediated masking of a linear endocytic motif*. *Journal of biological chemistry*, 2008. **283**(27): p. 18566-18572.
67. Ferrao, R., et al., *The Structural Basis for Class II Cytokine Receptor Recognition by JAK1*. *Structure*, 2016. **24**(6): p. 897-905.
68. Lupardus, P.J., et al., *Structure of the pseudokinase-kinase domains from protein kinase TYK2 reveals a mechanism for Janus kinase (JAK) autoinhibition*. *Proceedings of the National Academy of Sciences*, 2014. **111**(22): p. 8025-8030.
69. Murakami, M., et al., *Critical cytoplasmic region of the interleukin 6 signal transducer gp130 is conserved in the cytokine receptor family*. *Proceedings of the National Academy of Sciences*, 1991. **88**(24): p. 11349-11353.
70. Yan, H., et al., *Molecular characterization of an alpha interferon receptor 1 subunit (IFNAR1) domain required for TYK2 binding and signal transduction*. *Molecular and Cellular Biology*, 1996. **16**(5): p. 2074-2082.
71. Usacheva, A., et al., *Contribution of the Box 1 and Box 2 motifs of cytokine receptors to Jak1 association and activation*. *Journal of Biological Chemistry*, 2002. **277**(50): p. 48220-48226.
72. Wallweber, H.J., et al., *Structural basis of recognition of interferon- α receptor by tyrosine kinase 2*. *Nature structural & molecular biology*, 2014. **21**(5): p. 443-448.
73. Vainchenker, W. and S.N. Constantinescu, *JAK/STAT signaling in hematological malignancies*. *Oncogene*, 2013. **32**(21): p. 2601-2613.
74. Levine, R.L., et al., *Activating mutation in the tyrosine kinase JAK2 in polycythemia vera, essential thrombocythemia, and myeloid metaplasia with myelofibrosis*. *Cancer Cell*, 2005. **7**(4): p. 387-397.
75. Waters, Michael J. and Andrew J. Brooks, *JAK2 activation by growth hormone and other cytokines*. *Biochemical Journal*, 2015. **466**(1): p. 1-11.
76. Glassman, C.R., et al., *Structure of a Janus kinase cytokine receptor complex reveals the basis for dimeric activation*. *Science*, 2022. **376**(6589): p. 163-169.
77. Stark, G.R., et al., *HOW CELLS RESPOND TO INTERFERONS*. *Annual Review of Biochemistry*, 1998. **67**(1): p. 227-264.
78. Plataniias, L.C. and E.N. Fish, *Signaling pathways activated by interferons*. *Experimental Hematology*, 1999. **27**(11): p. 1583-1592.
79. Vinkemeier, U., et al., *DNA binding of in vitro activated Stat1 alpha, Stat1 beta and truncated Stat1: interaction between NH2-terminal domains stabilizes binding of two dimers to tandem DNA sites*. *The EMBO journal*, 1996. **15**(20): p. 5616-5626.
80. Mao, X., et al., *Structural Bases of Unphosphorylated STAT1 Association and Receptor Binding*. *Molecular Cell*, 2005. **17**(6): p. 761-771.
81. Chen, X., et al., *A reinterpretation of the dimerization interface of the N-terminal domains of STATs*. *Protein Science*, 2003. **12**(2): p. 361-365.

82. Wenta, N., et al., *Tyrosine phosphorylation regulates the partitioning of STAT1 between different dimer conformations*. Proceedings of the National Academy of Sciences, 2008. **105**(27): p. 9238.
83. Mertens, C., et al., *Dephosphorylation of phosphotyrosine on STAT1 dimers requires extensive spatial reorientation of the monomers facilitated by the N-terminal domain*. Genes & development, 2006. **20**(24): p. 3372-3381.
84. Strehlow, I. and C. Schindler, *Amino-terminal signal transducer and activator of transcription (STAT) domains regulate nuclear translocation and STAT deactivation*. Journal of Biological Chemistry, 1998. **273**(43): p. 28049-28056.
85. Chen, X., et al., *Crystal structure of a tyrosine phosphorylated STAT-1 dimer bound to DNA*. Cell, 1998. **93**(5): p. 827-839.
86. Martinez-Moczygemba, M., et al., *Distinct STAT structure promotes interaction of STAT2 with the p48 subunit of the interferon- α -stimulated transcription factor ISGF3*. Journal of biological chemistry, 1997. **272**(32): p. 20070-20076.
87. Li, X., et al., *Functional subdomains of STAT2 required for preassociation with the alpha interferon receptor and for signaling*. Molecular and cellular biology, 1997. **17**(4): p. 2048-2056.
88. Lim, C.P. and X. Cao, *Structure, function, and regulation of STAT proteins*. Molecular biosystems, 2006. **2**(11): p. 536-550.
89. Melén, K., L. Kinnunen, and I. Julkunen, *Arginine/lysine-rich structural element is involved in interferon-induced nuclear import of STATs*. Journal of Biological Chemistry, 2001. **276**(19): p. 16447-16455.
90. Fagerlund, R., et al., *Arginine/lysine-rich nuclear localization signals mediate interactions between dimeric STATs and importin α 5*. Journal of Biological Chemistry, 2002. **277**(33): p. 30072-30078.
91. Melén, K., et al., *Importin α nuclear localization signal binding sites for STAT1, STAT2, and influenza A virus nucleoprotein*. Journal of Biological Chemistry, 2003. **278**(30): p. 28193-28200.
92. Levy, D.E. and J. Darnell, *Stats: transcriptional control and biological impact*. Nature reviews Molecular cell biology, 2002. **3**(9): p. 651-662.
93. Gupta, S., et al., *The SH2 domains of Stat1 and Stat2 mediate multiple interactions in the transduction of IFN-alpha signals*. The EMBO journal, 1996. **15**(5): p. 1075-1084.
94. Zhang, J.J., et al., *Two contact regions between Stat1 and CBP/p300 in interferon γ signaling*. Proceedings of the National Academy of Sciences, 1996. **93**(26): p. 15092-15096.
95. Steen, H.C. and A.M. Gamero, *STAT2 phosphorylation and signaling*. Jak-Stat, 2013. **2**(4): p. e25790.
96. Kallal, L.E. and C.A. Biron, *Changing partners at the dance: variations in STAT concentrations for shaping cytokine function and immune responses to viral infections*. Jak-Stat, 2013. **2**(1): p. e23504.
97. McBride, K.M., C. McDonald, and N.C. Reich, *Nuclear export signal located within the DNA-binding domain of the STAT1 transcription factor*. The EMBO journal, 2000. **19**(22): p. 6196-6206.
98. Stancato, L.F., et al., *Preassociation of STAT1 with STAT2 and STAT3 in separate signalling complexes prior to cytokine stimulation*. J Biol Chem, 1996. **271**(8): p. 4134-7.
99. Yang, J. and G.R. Stark, *Roles of unphosphorylated STATs in signaling*. Cell Research, 2008. **18**(4): p. 443-451.

100. Basters, A., et al., *Molecular characterization of ubiquitin-specific protease 18 reveals substrate specificity for interferon-stimulated gene 15*. The FEBS Journal, 2014. **281**(7): p. 1918-1928.
101. Kim, K.I., et al., *Ube1L and protein ISGylation are not essential for alpha/beta interferon signaling*. Molecular and cellular biology, 2006. **26**(2): p. 472-479.
102. Malakhova, O.A., et al., *UBP43 is a novel regulator of interferon signaling independent of its ISG15 isopeptidase activity*. The EMBO journal, 2006. **25**(11): p. 2358-2367.
103. Arimoto, K.-i., et al., *STAT2 is an essential adaptor in USP18-mediated suppression of type I interferon signaling*. Nature Structural & Molecular Biology, 2017. **24**(3): p. 279-289.
104. Speer, S., et al., *ISG15 deficiency and increased viral resistance in humans but not mice*. Nature Communications, 2016. **7**: p. 11496.
105. Altman, J.B., et al., *Type I IFN is siloed in endosomes*. Proceedings of the National Academy of Sciences, 2020. **117**(30): p. 17510-17512.
106. Francois-Newton, V., et al., *USP18 establishes the transcriptional and anti-proliferative interferon α/β differential*. Biochemical Journal, 2012. **446**(3): p. 509-516.
107. Taft, J. and D. Bogunovic, *The Goldilocks Zone of Type I IFNs: Lessons from Human Genetics*. The Journal of Immunology, 2018. **201**(12): p. 3479-3485.
108. Chmiest, D., et al., *Spatiotemporal control of interferon-induced JAK/STAT signalling and gene transcription by the retromer complex*. Nature communications, 2016. **7**(1): p. 1-15.
109. Basters, A., et al., *Structural basis of the specificity of USP18 toward ISG15*. Nature Structural & Molecular Biology, 2017. **24**(3): p. 270-278.
110. Burkart, C., J.-B. Fan, and D.-E. Zhang, *Two Independent Mechanisms Promote Expression of an N-terminal Truncated USP18 Isoform with Higher DeISGylation Activity in the Nucleus*. Journal of Biological Chemistry, 2012. **287**(7): p. 4883-4893.
111. Kozak, M., *An analysis of 5'-noncoding sequences from 699 vertebrate messenger RNAs*. Nucleic Acids Research, 1987. **15**(20): p. 8125-8148.
112. Kurien, B.T. and R.H. Scofield, *Western blotting*. Methods, 2006. **38**(4): p. 283-293.
113. Lin, J.-S. and E.-M. Lai, *Protein-protein interactions: co-immunoprecipitation*, in *Bacterial Protein Secretion Systems*. 2017, Springer. p. 211-219.
114. Kessler, S.W., *Rapid isolation of antigens from cells with a staphylococcal protein A-antibody adsorbent: parameters of the interaction of antibody-antigen complexes with protein A*. The Journal of Immunology, 1975. **115**(6): p. 1617-1624.
115. Kessler, S.W., *Cell membrane antigen isolation with the staphylococcal protein A-antibody adsorbent*. The Journal of Immunology, 1976. **117**(5 Part 1): p. 1482-1490.
116. Louche, A., S.P. Salcedo, and S. Bigot, *Protein-protein interactions: pull-down assays*, in *Bacterial Protein Secretion Systems*. 2017, Springer. p. 247-255.
117. Li, Y., *The tandem affinity purification technology: an overview*. Biotechnology Letters, 2011. **33**(8): p. 1487-1499.
118. Rigaut, G., et al., *A generic protein purification method for protein complex characterization and proteome exploration*. Nature biotechnology, 1999. **17**(10): p. 1030-1032.
119. Brückner, A., et al., *Yeast two-hybrid, a powerful tool for systems biology*. International journal of molecular sciences, 2009. **10**(6): p. 2763-2788.

120. Fields, S. and O.-k. Song, *A novel genetic system to detect protein–protein interactions*. *Nature*, 1989. **340**(6230): p. 245-246.
121. Johnsson, N. and A. Varshavsky, *Split ubiquitin as a sensor of protein interactions in vivo*. *Proceedings of the National Academy of Sciences*, 1994. **91**(22): p. 10340-10344.
122. Kerppola, T.K., *Visualization of molecular interactions by fluorescence complementation*. *Nature Reviews Molecular Cell Biology*, 2006. **7**(6): p. 449-456.
123. Hu, C.-D., Y. Chinenov, and T.K. Kerppola, *Visualization of interactions among bZIP and Rel family proteins in living cells using bimolecular fluorescence complementation*. *Molecular cell*, 2002. **9**(4): p. 789-798.
124. Bagchi, S., R. Fredriksson, and Å. Wallén-Mackenzie, *In situ proximity ligation assay (PLA)*, in *ELISA*. 2015, Springer. p. 149-159.
125. Fredriksson, S., et al., *Protein detection using proximity-dependent DNA ligation assays*. *Nature biotechnology*, 2002. **20**(5): p. 473-477.
126. Förster, T., *Zwischenmolekulare energiewanderung und fluoreszenz*. *Annalen der physik*, 1948. **437**(1-2): p. 55-75.
127. Periasamy, A., et al., *Chapter 22 Quantitation of Protein–Protein Interactions: Confocal FRET Microscopy*, in *Methods in Cell Biology*. 2008, Academic Press. p. 569-598.
128. Krause, C.D., et al., *Ligand-independent interaction of the type I interferon receptor complex is necessary to observe its biological activity*. *Cytokine*, 2013. **64**(1): p. 286-297.
129. Bacia, K., S.A. Kim, and P. Schwille, *Fluorescence cross-correlation spectroscopy in living cells*. *Nature Methods*, 2006. **3**(2): p. 83-89.
130. Piehler, J., et al., *Assessment of affinity constants by rapid solid phase detection of equilibrium binding in a flow system*. *Journal of Immunological Methods*, 1997. **201**(2): p. 189-206.
131. Cunningham, B.C., et al., *Dimerization of the extracellular domain of the human growth hormone receptor by a single hormone molecule*. *Science*, 1991. **254**(5033): p. 821.
132. Atanasova, M. and A. Whitty, *Understanding cytokine and growth factor receptor activation mechanisms*. *Critical Reviews in Biochemistry and Molecular Biology*, 2012. **47**(6): p. 502-530.
133. Stroud, R.M. and J.A. Wells, *Mechanistic Diversity of Cytokine Receptor Signaling Across Cell Membranes*. *Science*’s STKE, 2004. **2004**(231): p. re7.
134. Gent, J., et al., *Ligand-independent growth hormone receptor dimerization occurs in the endoplasmic reticulum and is required for ubiquitin system-dependent endocytosis*. *Proceedings of the National Academy of Sciences*, 2002. **99**(15): p. 9858.
135. Brown, R.J., et al., *Model for growth hormone receptor activation based on subunit rotation within a receptor dimer*. *Nature Structural & Molecular Biology*, 2005. **12**(9): p. 814-821.
136. Brooks, A.J., et al., *Mechanism of Activation of Protein Kinase JAK2 by the Growth Hormone Receptor*. *Science*, 2014. **344**(6185): p. 1249783.
137. Tenhumberg, S., et al., *gp130 dimerization in the absence of ligand: Preformed cytokine receptor complexes*. *Biochemical and Biophysical Research Communications*, 2006. **346**(3): p. 649-657.
138. Zaks-Zilberman, M., et al., *Interleukin-5 receptor subunit oligomerization and rearrangement revealed by fluorescence resonance energy transfer imaging*. *Journal of Biological Chemistry*, 2008. **283**(19): p. 13398-13406.

139. Krause, C.D., et al., *Preassembly and ligand-induced restructuring of the chains of the IFN- γ receptor complex: the roles of Jak kinases, Stat1 and the receptor chains*. Cell Research, 2006. **16**(1): p. 55-69.
140. Krause, C.D., et al., *Seeing the Light*. Molecular & Cellular Proteomics, 2002. **1**(10): p. 805.
141. Krause, C.D., et al., *Interactions among the components of the interleukin-10 receptor complex*. Biochemical and Biophysical Research Communications, 2006. **340**(2): p. 377-385.
142. Thorn, K., *Genetically encoded fluorescent tags*. Molecular biology of the cell, 2017. **28**(7): p. 848-857.
143. Nelson, A.L., *Antibody fragments*. mAbs, 2010. **2**(1): p. 77-83.
144. Rouet, R., D. Lowe, and D. Christ, *Stability engineering of the human antibody repertoire*. FEBS letters, 2014. **588**(2): p. 269-277.
145. WoÈrn, A. and A. PluÈckthun, *Stability engineering of antibody single-chain Fv fragments*. Journal of molecular biology, 2001. **305**(5): p. 989-1010.
146. Hamers-Casterman, C., et al., *Naturally occurring antibodies devoid of light chains*. Nature, 1993. **363**(6428): p. 446-448.
147. Muyldermans, S., *Single domain camel antibodies: current status*. Reviews in Molecular Biotechnology, 2001. **74**(4): p. 277-302.
148. Kirchhofer, A., et al., *Modulation of protein properties in living cells using nanobodies*. Nat Struct Mol Biol, 2010. **17**(1): p. 133-8.
149. Qin, D., Y. Xia, and G.M. Whitesides, *Soft lithography for micro- and nanoscale patterning*. Nature Protocols, 2010. **5**(3): p. 491-502.
150. Torres, A.J., et al., *Nanobiotechnology and cell biology: micro-and nanofabricated surfaces to investigate receptor-mediated signaling*. Annu. Rev. Biophys., 2008. **37**: p. 265-288.
151. Perl, A., D.N. Reinhoudt, and J. Huskens, *Microcontact Printing: Limitations and Achievements*. Advanced Materials, 2009. **21**(22): p. 2257-2268.
152. Steadman, B.L., et al., *The effects of surface adsorption on the thermal stability of proteins*. Biotechnology and bioengineering, 1992. **40**(1): p. 8-15.
153. Keppler, A., et al., *A general method for the covalent labeling of fusion proteins with small molecules in vivo*. Nature biotechnology, 2003. **21**(1): p. 86-89.
154. Keppler, A., et al., *Labeling of fusion proteins of O6-alkylguanine-DNA alkyltransferase with small molecules in vivo and in vitro*. Methods, 2004. **32**(4): p. 437-444.
155. Engin, S., et al., *Benzylguanine thiol self-assembled monolayers for the immobilization of SNAP-tag proteins on microcontact-printed surface structures*. Langmuir, 2010. **26**(9): p. 6097-6101.
156. Los, G.V., et al., *HaloTag: A Novel Protein Labeling Technology for Cell Imaging and Protein Analysis*. ACS Chemical Biology, 2008. **3**(6): p. 373-382.
157. Lee, S. and N.D. Spencer, *Adsorption Properties of Poly(l-lysine)-graft-poly(ethylene glycol) (PLL-g-PEG) at a Hydrophobic Interface: Influence of Tribological Stress, pH, Salt Concentration, and Polymer Molecular Weight*. Langmuir, 2008. **24**(17): p. 9479-9488.
158. Löchte, S., et al., *Live cell micropatterning reveals the dynamics of signaling complexes at the plasma membrane*. Journal of Cell Biology, 2014. **207**(3): p. 407-418.
159. Wedeking, T., et al., *Spatiotemporally Controlled Reorganization of Signaling Complexes in the Plasma Membrane of Living Cells*. Small, 2015. **11**(44): p. 5912-5918.

160. Wedeking, T., et al., *Single Cell GFP-Trap Reveals Stoichiometry and Dynamics of Cytosolic Protein Complexes*. Nano letters, 2015. **15**.
161. Parsons, J.T., A.R. Horwitz, and M.A. Schwartz, *Cell adhesion: integrating cytoskeletal dynamics and cellular tension*. Nature reviews Molecular cell biology, 2010. **11**(9): p. 633-643.
162. Humphries, J.D., A. Byron, and M.J. Humphries, *Integrin ligands at a glance*. Journal of cell science, 2006. **119**(19): p. 3901-3903.
163. Ruoslahti, E. and M.D. Pierschbacher, *New perspectives in cell adhesion: RGD and integrins*. Science, 1987. **238**(4826): p. 491.
164. VandeVondele, S., J. Vörös, and J.A. Hubbell, *RGD-grafted poly-L-lysine-graft-(polyethylene glycol) copolymers block non-specific protein adsorption while promoting cell adhesion*. Biotechnol Bioeng, 2003. **82**(7): p. 784-90.
165. Mattheyses, A.L., S.M. Simon, and J.Z. Rappoport, *Imaging with total internal reflection fluorescence microscopy for the cell biologist*. Journal of cell science, 2010. **123**(21): p. 3621-3628.
166. Dirscherl, C., et al., *Specific Capture of Peptide-Receptive Major Histocompatibility Complex Class I Molecules by Antibody Micropatterns Allows for a Novel Peptide-Binding Assay in Live Cells*. Small, 2017. **13**(15): p. 1602974.
167. Jain, A., et al., *Probing cellular protein complexes using single-molecule pull-down*. Nature, 2011. **473**(7348): p. 484-488.
168. Hu, C.-D. and T.K. Kerppola, *Simultaneous visualization of multiple protein interactions in living cells using multicolor fluorescence complementation analysis*. Nature Biotechnology, 2003. **21**(5): p. 539-545.
169. Shyu, Y.J., et al., *Identification of new fluorescent protein fragments for bimolecular fluorescence complementation analysis under physiological conditions*. BioTechniques, 2006. **40**(1): p. 61-66.
170. Graham, F.L. and A.J. van der Eb, *A new technique for the assay of infectivity of human adenovirus 5 DNA*. virology, 1973. **52**(2): p. 456-467.
171. Muster, B., et al., *Respiratory Chain Complexes in Dynamic Mitochondria Display a Patchy Distribution in Live Cells*. PLOS ONE, 2010. **5**(7): p. e11910.
172. Gautier, A., et al., *An engineered protein tag for multiprotein labeling in living cells*. Chemistry & biology, 2008. **15**(2): p. 128-136.
173. Roder, F., et al., *Spatial organization of lipid phases in micropatterned polymer-supported membranes*. Journal of the American Chemical Society, 2013. **135**(4): p. 1189-1192.
174. Subach, O.M., et al., *An enhanced monomeric blue fluorescent protein with the high chemical stability of the chromophore*. PLoS One, 2011. **6**(12): p. e28674.
175. Zacharias, D.A., et al., *Partitioning of lipid-modified monomeric GFPs into membrane microdomains of live cells*. Science, 2002. **296**(5569): p. 913-6.
176. Shaner, N.C., et al., *Improved monomeric red, orange and yellow fluorescent proteins derived from *Discosoma* sp. red fluorescent protein*. Nat Biotechnol, 2004. **22**(12): p. 1567-72.
177. Shaner, N.C., et al., *Improving the photostability of bright monomeric orange and red fluorescent proteins*. Nat Methods, 2008. **5**(6): p. 545-51.
178. Liße, D., et al., *Selective Targeting of Fluorescent Nanoparticles to Proteins Inside Live Cells*. Angewandte Chemie International Edition, 2011. **50**(40): p. 9352-9355.
179. Yin, J., et al., *Genetically encoded short peptide tag for versatile protein labeling by *Sfp* phosphotransferase*. Proc Natl Acad Sci U S A, 2005. **102**(44): p. 15815-20.

180. Garcin, G., et al., *High efficiency cell-specific targeting of cytokine activity*. Nature Communications, 2014. **5**(1): p. 3016.
181. Welch, B.L., *THE GENERALIZATION OF 'STUDENT'S' PROBLEM WHEN SEVERAL DIFFERENT POPULATION VARIANCES ARE INVOLVED*. Biometrika, 1947. **34**(1-2): p. 28-35.
182. Sprague, B.L., et al., *Analysis of binding reactions by fluorescence recovery after photobleaching*. Biophys J, 2004. **86**(6): p. 3473-95.
183. Sprague, B.L. and J.G. McNally, *FRAP analysis of binding: proper and fitting*. Trends Cell Biol, 2005. **15**(2): p. 84-91.
184. Dickson, R.M., et al., *On/off blinking and switching behaviour of single molecules of green fluorescent protein*. Nature, 1997. **388**(6640): p. 355-358.
185. Sergé, A., et al., *Dynamic multiple-target tracing to probe spatiotemporal cartography of cell membranes*. Nature Methods, 2008. **5**(8): p. 687-694.
186. Appelhans, T., et al., *Nanoscale Organization of Mitochondrial Microcompartments Revealed by Combining Tracking and Localization Microscopy*. Nano Letters, 2012. **12**(2): p. 610-616.
187. Hess, S.T., T.P.K. Girirajan, and M.D. Mason, *Ultra-high resolution imaging by fluorescence photoactivation localization microscopy*. Biophysical journal, 2006. **91**(11): p. 4258-4272.
188. Niewidok, B., et al., *Single-molecule imaging reveals dynamic biphasic partition of RNA-binding proteins in stress granules*. Journal of Cell Biology, 2018. **217**(4): p. 1303-1318.
189. Shuang, B., et al., *Fast Step Transition and State Identification (STaSI) for Discrete Single-Molecule Data Analysis*. The Journal of Physical Chemistry Letters, 2014. **5**(18): p. 3157-3161.
190. Garcia, D., *Robust smoothing of gridded data in one and higher dimensions with missing values*. Computational Statistics & Data Analysis, 2010. **54**(4): p. 1167-1178.
191. Reynolds, D.A., *Gaussian Mixture Models*. Encyclopedia of biometrics, 2009. **741**.
192. Balleza, E., J.M. Kim, and P. Cluzel, *Systematic characterization of maturation time of fluorescent proteins in living cells*. Nature methods, 2018. **15**(1): p. 47-51.
193. Skånland, S.S., *Phospho Flow Cytometry with Fluorescent Cell Barcoding for Single Cell Signaling Analysis and Biomarker Discovery*. J Vis Exp, 2018(140).
194. Jans, D.A., A.J. Martin, and K.M. Wagstaff, *Inhibitors of nuclear transport*. Curr Opin Cell Biol, 2019. **58**: p. 50-60.
195. Jain, A., et al., *Single-molecule pull-down for studying protein interactions*. Nature protocols, 2012. **7**(3): p. 445-452.

6.2 List of Figures

Figure 1: Genomic and proteomic complexity.....	2
Figure 2: Cytokine-induced JAK-STAT signaling pathways.....	4
Figure 3: Type I IFN signaling pathway.	6
Figure 4: FERM and SH2 domains interact with receptor box motifs.....	10
Figure 5: Homodimeric cytokine receptor activation.	12
Figure 6: Two-step model of JAK activation.....	13
Figure 7: STAT1 domains and crystal structure in complex with DNA.	15
Figure 8: Model for STAT1 Oligomerization.	17

Figure 9: IFN-induced IFNAR dimerization and negative feedback regulation by USP18.	19
Figure 10: Structure of USP18 bound ISG15.	21
Figure 11 Antibody-related protein binders.	27
Figure 12: Micropatterned surface architecture.	29
Figure 13: Nanobody live cell micropatterning.	30
Figure 14: Single cell pull-down (SiCPull).	32
Figure 15: Two-hybrid NB pull-down assays.	34
Figure 16: Molecular structure of PLL-g-PEG-HTL.	38
Figure 17: Molecular structure of PLL-g-PEG-RGD.	39
Figure 18: <i>In vitro</i> capturing of HaloTag-mEGFP into HTL micropatterns.	47
Figure 19: Live cell micropatterning of mEGFP.	48
Figure 20: Fluorescence contrast interaction analysis of USP18 and ISG15.	50
Figure 21: Quantifying the stability of USP18-ISG15 via FRAP.	51
Figure 22: Interaction of USP18 with ISG15.	53
Figure 23: Interaction Dynamics of ISG15 and USP18.	56
Figure 24: Competition between ISG15 and STAT2 for USP18.	57
Figure 25: Recruitment to STAT2 prevents USP18 interaction with ISG15.	58
Figure 26: C-terminal ISG15 interacts with STAT2-bound USP18.	60
Figure 27: ISG15 does not interact with STAT2.	62
Figure 28: Competition at the cytokine signaling complex.	63
Figure 29: N-terminus of USP18 required for STAT2 binding.	64
Figure 30 BiFC is not induced by the anti-GFP NB enhancer.	65
Figure 31: Specific capturing of complemented USP18-mEGFP-ISG15.	66
Figure 32: Competition between STAT2 and ISG15 prevents two-hybrid complementation.	68
Figure 33: Efficient <i>in vitro</i> capturing of mEGFP.	69
Figure 34: SiCPull strategy to capture GFP-fused STAT1.	70
Figure 35: Probing dissociation rate constants of STAT complexes.	72
Figure 36: <i>In vitro</i> single molecule density titration.	74
Figure 37: Localization and Cluster analysis using SLIMfast.	75
Figure 38: Single molecule analysis using the BleachCounter.	76
Figure 39: Inhibited capturing of nuclear proteins.	78
Figure 40: Single molecule analysis reveals oligomerization of STAT1.	79
Figure 41: Specific analysis of interacting JAKs by selective capturing of complemented GFP.	80

6.3 Abbreviations

μ CP	Microcontact printing	Fab	Fragment antigen binding
BFP	Blue fluorescent protein	FCS, FCCS	fluorescence (cross-)correlation spectroscopy
BG	Benzyl guanine	FERM	Four-point-one, ezrin, radixin and moesin domain
BiFC	Bimolecular fluorescence complementation	FRAP	Fluorescence recovery after photobleaching
BSA	Bovine serum albumin	FRET	Förster resonance energy transfer
BT	Biotin	fSNAP	Fast SNAP-Tag (New England Biolabs)
cAMP	Cyclic adenosine monophosphate	GFP	green fluorescent protein
CBP	CREB-binding protein	GHR	Growth hormone receptor
CC	Coiled-coil domain	GOPTS	glycidylpropylsilane
CFP	Cyan fluorescent protein	HaloTag	self-labeling protein tag
C _H	Heavy chain constant domain	His-tag	Polyhistidine-tag
C-ISG15	C-terminal ISG15 domain	HTL	HaloTag ligand
C _L	Light chain constant domain	IBB1/2	ISG15 binding box 1/2
CLSM	Confocal laser scanning microscopy	ICD	intracellular domain
CmEGFP	C-terminal domain of split GFP	IFN	Interferon
CMOS	complementary metal-oxide-semiconductor	IFNAR	Interferon α receptor
Co-IP	Co-immunoprecipitation	IgG	Immunoglobulin G
CRM1	Chromosome region maintenance 1, or exportin 1	IRF9	IFN regulatory factor 9, formerly p48
cryo-EM	cryogenic electron microscopy	ISG	Interferon-stimulated gene
C-term.	C-terminus	ISG15	Interferon-stimulated gene 15
CTLs	cytotoxic T cells	ISGF3	interferon-stimulated gene factor 3
DBD	DNA-binding domain	ISRE	IFN-I-stimulated response element
DBSCAN	Density-based spatial clustering of applications with noise	JAK	Janus kinase
DIC	Differential interference contrast	KRAS	Kirsten rat sarcoma viral oncogene homologue
DMSO	Dimethyl sulfoxide	LD	Linker domain
ECM	Extracellular matrix	LLSM	Lattice light sheet microscopy
ELISA	Enzyme-linked immunosorbent assays	mCherry	Monomeric orange fluorescent protein
EpoR	Erythropoietin receptor		

Abbreviations

mEGFP	Monomeric enhanced green fluorescent protein	SAM	Self-assembled monolayer
MEM	Minimal essential medium	SAV	Streptavidin
Meo	Methoxy	scFv	Single chain variable fragment
mTagBFP	Monomeric blue fluorescent protein	SEM	Scanning electron microscope
MTT	multiple-target tracing	SH2	src-homology 2
NB	Nanobody	SiCPull	Single cell pull-down
ND	N-terminal domain	SiMPull	single-molecule pull-down
NES	Nuclear export signal	SiR	Silicon rhodamine, far-red fluorophore
N-ISG15	N-terminal ISG15 domain	SLIMfast	Software for localization-based imaging in Matlab
NK	natural killer cells	SM-SiCPull	Single molecule single cell pull-down
NLS	Nuclear localization signal	SNAPTag	self-labeling protein tag
NmEGFP	N-terminal domain of split GFP	SOCS	suppressors of cytokine signaling
NTA	Nitrilotriacetic acid	STaSI	Step transition and state identification algorithm
N-term.	N-terminus	STAT	Signal transducer and activator of transcription
p300	E1A binding protein p300	TAD	Transactivation domain
PBS	Phosphate buffered saline	tdmEGFP	tandem-fused monomeric enhanced green fluorescent protein
PDMS	Poly-dimethylsiloxane	TIRFM	Total internal reflection fluorescence microscopy
PEG	Poly(ethylene-glycol)	TK	Tyrosine kinase domain
PFA	Para-formaldehyde	TMD	Transmembrane domain
PH	Pleckstrin homology domain	TMR	Tetramethylrhodamine
PIAS	protein inhibitors of activated STAT	Tpo	Thrombopoietin
PK	Pseudokinase domain	TpoR	Thrombopoietin receptor
PKA	Protein kinase A	Tyk2	Tyrosine kinase 2
PLA	Proximity ligation assay	USP18	Ubiquitin specific protease 18
PLL	Poly-L-lysine	VF	JAK2 V617F mutation
PPI	Protein-protein interaction	VH	Heavy chain variable domain
PSF	Point spread function	VHH	Variable domain of a heavy-chain antibody
PTP	protein-tyrosine-phosphatase	VL	Light chain variable domain
PTP1B	protein-tyrosine phosphatase 1B	WT	Wildtype
RFP	Red fluorescent protein	Y	Tyrosine activation domain
RGD	Arginine-glycine-aspartic acid	YFP	Yellow fluorescent protein
ROI	Region of interest		

7 Publications

Altman, J.B., Taft, J., **Wedeking, T.**, Gruber, C.N., Holtmannspötter, M., Piehler, J., and Bogunovic, D., Type I IFN is siloed in endosomes. *Proceedings of the National Academy of Sciences*, 2020. 117(30): p. 17510.

Speer, S., Li, Z., Buta, S., Payelle-Brogard, B., Qian, L., Vigant, F., Rubino, E., Gardner, T., **Wedeking, T.**, Hermann, M., Duehr, J., Sanal, O., Tezcan, I., Mansouri, N., Tabarsi, P., Mansouri, D., Francois-Newton, V., Daussy, C., Rodriguez, M., and Bogunovic, D., ISG15 deficiency and increased viral resistance in humans but not mice. *Nature Communications*, 2016. 7: p. 11496.

Volf, A., Kovalev, A., **Wedeking, T.**, Gorb, E., Xue, L., You, C., Piehler, J., Gorb, S., and Steinhart, M., Bioinspired monolithic polymer microsphere arrays as generically anti-adhesive surfaces. *Bioinspiration & Biomimetics*, 2016. 11: p. 025002.

Wedeking, T., Löchte, S., Birkholz, O., Wallenstein, A., Trahe, J., Klingauf, J., Piehler, J., and You, C., Spatiotemporally Controlled Reorganization of Signaling Complexes in the Plasma Membrane of Living Cells. *Small*, 2015. 11(44): p. 5912-5918.

Wedeking, T., Löchte, S., Richter, C., Bhagawati, M., Piehler, J., and You, C., Single Cell GFP-Trap Reveals Stoichiometry and Dynamics of Cytosolic Protein Complexes. *Nano letters*, 2015. 15.

8 Curriculum vitae

Personal data

Name	Tim Wedeking
Date & place of birth	19.09.1989 in Detmold
Nationality	German

Education and work

02/2022 - present	Product manager Systec GmbH & Co. KG
04/2015 - present	Doctoral candidate University of Osnabrück, Division of Biophysics Advisor: Prof. Dr. Jacob Piehler Thesis: "Generic Micropatterned Pull-Down Assays for Quantifying Interaction Dynamics and Stoichiometry of Protein-Protein Interactions"
11/2012 – 04/2015	Research assistant University of Osnabrück, Division of Biophysics
10/2012 – 10/2014	Master of Science University of Osnabrück, Division of Biophysics Advisor: Prof. Dr. Jacob Piehler Thesis: "Metal-induced energy transfer (MIET) for resolving the conformational organization of transmembrane receptors in living cells"
10/2009 – 09/2012	Bachelor of Science University of Osnabrück, Division of Biophysics Advisor: Prof. Dr. Jacob Piehler Thesis: "Functional surface micro-patterning for spatial organization of membrane proteins in living cells"
06/2009	Abitur (A-Levels), Gymnasium Horn-Bad Meinberg

9 Declaration

I hereby declare that the presented thesis ‘Generic Micropatterned Pull-Down Assays for Quantifying Interaction Dynamics and Stoichiometry of Protein-Protein Interactions’ was prepared entirely on my own and I have not used outside sources without declaration in the text. Any concepts or quotations applicable to these sources are clearly attributed to them. The following people attributed to this work as collaboration partners:

1. Hella Kenneweg and Gabriele Hikade extensively supported in terms of protein expression and molecular biology, as well as their well-appreciated experience.
2. Sara Löchte supplied PLL-PEGs and fusion proteins (IFNAR, STATs), as she also investigated the type I IFN signaling pathway.
3. Christoph Drees and Changjiang You aided in PLL-PEG synthesis and supplied the laboratory with affinity tags and labeling dyes.
4. Rainer Kurre managed the fluorescence microscopy setups and heavily supported the image acquisition.
5. Christian P. Richter advised and implemented sophisticated Matlab software for live cell micropatterning contrast analysis and single molecule localization and stoichiometry analysis.

I have not attempted a promotion before.

(Osnabrück, 06.09.2023) (Tim Wedeking)